Computers and Structures 296 (2024) 107293

Contents lists available at ScienceDirect

Computers and Structures

journal homepage: www.elsevier.com/locate/compstruc

Enhanced damage detection for noisy input signals using improved reptile search algorithm and data analytics techniques

Sahar Hassani [a], Ulrike Dackermann [a,*], Mohsen Mousavi [a], Jianchun Li [b,*]

[a] Centre for Infrastructure Engineering and Safety, School of Civil and Environmental Engineering, University of New South Wales, Sydney, NSW, Australia
[b] School of Civil and Environmental Engineering, University of Technology Sydney, Ultimo, NSW, 2007, Australia

ARTICLE INFO

Keywords:
Structural health monitoring
Frequency response function
Johansen cointegration
Mutual information
Outlier detection
Data fusion

ABSTRACT

The sensitivity of structural health monitoring systems to environmental and operational conditions poses a significant challenge due to their inherent susceptibility to outliers. This paper proposes an effective model-updating-based optimization algorithm that can alleviate the impact of outliers associated with field and operational fluctuations. The proposed method addresses the influence of uncertainties from sources such as white noise, colored noise, and measurement errors, which can introduce outliers in datasets. The approach comprises a hybrid procedure in which a Gaussian smoothing technique is first employed to smooth out measured data to reduce the impact of irregularities. Next, Johansen cointegration is employed for raw data fusion to further enhance the signature of shared patterns. A novel optimization algorithm based on the Reptile Search Algorithm (RSA), named Improved RSA (IRSA), is proposed to solve the objective function based on the concept of mutual information. This algorithm provides a superior solution with much improved computational speed and accuracy compared to RSA. The new hybrid method was validated by several numerical and experimental damage detection studies. Furthermore, it was compared to other state-of-the-art methods described in the literature. The results clearly demonstrate the superior performance of the newly developed method.

1. Introduction

Structural health monitoring (SHM) involves continuously monitoring structural responses using sensors, data acquisition systems, and advanced signal processing techniques in order to evaluate conditions, serviceability, and safety of the structures, in which detecting damage/deterioration is a crucial part. Related damage detection techniques may suffer from sensor malfunctioning or measurement noise leading to erroneous data. Over the past decades, researchers dedicated substantial efforts to the development of effective methods for damage identification using data contaminated with measurement noise and errors. Although advanced signal processing facilitates extracting meaningful information from sensor measurements [1], leveraging other techniques helps to alleviate the effect of inaccurate data leading to the presence of outliers. Such practice, however, requires multidisciplinary knowledge that spans applied mathematics, data analytics, and advanced signal processing. The techniques may contribute to robust noise filtering [2], feature extraction [3], pattern recognition [4], and outlier removal [5].

The input signal type plays an important role in SHM. Traditionally, modal data has been used for vibration-based SHM techniques [6]. However, when considering the challenges associated with using modal data, alternative approaches, such as the Frequency Response Function (FRF), prove more advantageous as they offer several benefits addressing the limitations and improving the effectiveness of damage detection in SHM applications [7]. Firstly, modal data only captures limited information at resonant frequencies, thereby restricting the amount of information that can be extracted from a broadband range of the FRF. In contrast, the FRF provides a comprehensive frequency response profile across a wide frequency range, enabling a more detailed understanding of the structural behavior. This broader coverage allows for a more comprehensive structural health assessment, including detecting damage or anomalies occurring at frequencies other than resonant frequencies. Secondly, modal techniques tend to focus on lower modes, which can

* Corresponding authors.
E-mail addresses: u.dackermann@unsw.edu.au (U. Dackermann), jianchun.li@uts.edu.au (J. Li).

https://doi.org/10.1016/j.compstruc.2024.107293
Received 26 October 2023; Accepted 16 January 2024
Available online 6 February 2024

limit the sensitivity to prominent damage types that may manifest in higher modes, such as smaller local damage. The sensitivity of FRFs to higher modes enables the detection of subtle or localized damage that may not be readily discernible using modal data alone. Furthermore, errors in the modal extraction process can affect the accuracy and reliability of modal data, introducing uncertainties into subsequent analysis or damage detection algorithms. In comparison, FRFs, which are directly measured or estimated from input-output measurements, eliminate the dependency on modal extraction procedures and minimize potential errors. Moreover, FRFs capture the unique response characteristics at different frequencies, overcoming the limitations associated with information redundancy and enabling the detection of damage in structures with closely-spaced eigenvalues [8,9]. Given these challenges related to modal data and the advantages offered by the FRF, it is evident that utilizing the FRF in SHM methodologies provides a more practical approach to damage detection.

However, FRF measurements can be accompanied by several uncertainties, such as measurement errors and different types of noise contamination [10]. This can substantially impact the identification of modal parameters and jeopardize the accuracy of damage detection results.

Several techniques are proposed to tackle the problems arising from using FRF for damage detection. Beale et al. [11] presented an adaptive wavelet packet denoising algorithm for numerous SHM technologies, including acoustics, vibrations, and acoustic emission. In order to enhance the performance of real-time SHM measurements, an algorithm was built that incorporated non-traditional approaches to noise estimation, threshold selection, and threshold application. The results showed that the proposed algorithm enhanced damage detection performance by up to 60% in most cases while reducing false detection rates. de Castro et al. [12] proposed a novel index based on cross-correlation signal processing, specifically designed for noisy environments. This index was tested in both the frequency domain, using impedance measurements directly, and in the time domain, based on the wavelet transform of the transducer response signals. This approach to material feature extraction in noisy environments was demonstrated to be effective with an aluminum structure with different noise levels. In [13], a hybrid damage detection technique combining variational mode decomposition (VMD) and frequency domain decomposition (FDD) was proposed to overcome heavily noise-contaminated environments. Analysis of small-magnitude damage was performed using Gaussian pulse noise ranging from 0 to 100%. To reduce the amount of sensor data necessary, wavelet-based algorithms were used to obtain intrinsic mode functions (IMFs) from one sensor's output. The natural frequencies of the structure were then determined by using these IMFs in the FDD algorithm. Damage identification results with VMD+FDD were satisfactory with 100% noise contamination, whereas results with EMD+FDD were not as accurate when noise levels exceeded 20%. A novel method for denoising vibration signals in SHM was introduced by Fan et al. [14]. The method utilizes specialized residual convolutional neural networks. The proposed approach was evaluated using acceleration data obtained from the Guangzhou New TV Tower. The findings demonstrate the effectiveness of the proposed approach in enhancing acceleration data quality across different noise levels and types.

The governing assumption in SHM is that any noise contamination follows a stationary Gaussian model (white noise). This is based on the assumption that the system dynamics are time-invariant throughout the analysis, and hence, it is safe to assume that the properties of noise will remain the same. Consequently, the generated noise will likely follow a stationary distribution [15].

However, several researchers have investigated the contamination of FRFs with nonstationary colored noise. According to Hanson et al. [16], if FRFs are generated using colored noise excitation, no reference will be available to correct the regenerated FRFs from in-band poles and zeros. This results in FRFs exhibiting an arbitrary slope due to the effect of out-of-band poles and zeros. In other words, the non-flat power spectral density of the input colored noise can interact with the structure's frequency response characteristics, leading to distortions and uncertainties in the measured FRFs. This will result in the loss of relative scaling between the mode shapes as the slope will vary between measurement locations. Consequently, this will introduce colored noise contamination to the regenerated FRFs.

It is vital to develop a technique to overcome the uncertainties associated with the process of FRF regeneration. Adhikari and Kay [17] proposed converting colored noise into white Gaussian noise. A method has also been developed by Luo et al. [18] to identify the natural frequencies of a structure under unknown colored noise excitation using the second singular value of the transmissibility matrices. Alamdari et al. [19] presented a technique for cleaning FRFs from correlated colored noise using a Gaussian kernel.

This paper proposes a robust method for detecting damage from regenerated uncertain FRFs contaminated with low-frequency colored noise. The study leverages the concept of cointegration–a technique from econometrics that seeks to find common trends among a set of non-stationary signals–to mitigate the nonstationary effect of highly correlated colored noise. In this context, we elucidate the efficacy of cointegration as a powerful technique for addressing uncertainties in FRF measurements. The Johansen cointegration test was initially proposed by Søren Johansen [20] and involves estimating a vector autoregressive model and conducting tests to determine the presence of cointegration. The test provides information about the number of cointegrating vectors (relationships) and the corresponding coefficients. The effectiveness of cointegration for SHM has been investigated by Cross and Worden [21]. Moreover, a non-stationary effect produced by temperature variations was successfully mitigated for long-term condition monitoring of civil infrastructure [22,23]. Using cointegration analysis of nonlinear acoustics also successfully removed the unwanted effects of applied loads in the damage detection of intelligent composite materials [24].

Signal smoothing techniques aim at enhancing the quality of signals by reducing noise and eliminating outliers. These techniques modify the data to minimize noise while preserving essential features of the signal. In certain instances, it can be highly advantageous to apply signal smoothing prior to applying the Johansen cointegration test. By reducing the noise, smoothing can enhance the ability of the Johansen test to detect the underlying cointegrating relationships. Therefore, the proposed procedure entails a sequential application of Johansen cointegration and a smoothing technique to effectively deal with outliers in the data. Smoothing techniques like moving average, Gaussian smoothing, or Savitzky-Golay filtering can be applied to achieve the desired quality in the studied signal. On the other hand, Johansen cointegration is a statistical technique used in econometrics to investigate the long-term relationship between multiple time series variables. It helps determine whether a set of variables share a common stochastic trend or are cointegrated Cross et al. [22], Dao and Staszewski [25], Tome et al. [26]. Cointegration is an essential concept in time series analysis, as it reveals a relationship among a set of signals allowing for meaningful interpretation and modeling.

In addition to mitigating non-stationary effects in FRFs, in this paper, Johansen cointegration is innovatively employed as a data fusion algorithm to obtain common trends among a set of FRFs. Typically, Johansen cointegration is used to analyze the long-term relationships among a set of variables. However, it is also robust to the presence of outliers in the dataset. As such, the obtained signal is clear from various types of uncertainties, including those stemming from colored noise excitation. Data fusion combines information from multiple sources to obtain a more comprehensive and accurate representation of the underlying phenomenon [27]. In this context, Johansen cointegration can be used by examining the cointegrating relationships among variables from different sources. Since the most informative part of FRF signals is extracted and used for further analysis, the proposed method can hence be considered a data fusion technique.

Advancements in mathematical and computational technologies have driven the development of sophisticated optimization algorithms. Optimization algorithms provide a powerful tool for refining and optimizing the performance of SHM systems. These algorithms aim to find the optimal values of variables that best satisfy a given objective function or criteria. Optimization techniques employed in SHM systems can be categorized into four categories:

- Biology-based algorithms such as differential evolution (DE), genetic algorithm (GA), and particle swarm optimization (PSO).
- Geography-based algorithms such as the imperialistic competition algorithm (ICA) and Tabu search (TS).
- Physics-based algorithms such as simulated annealing (SA), gravitational search algorithm (GSA), electromagnetism-like algorithm (EMA), particle collision algorithm (PCA), and gravitation field algorithm (GFA).
- Sequential placement algorithms include backward sequential sensor placement (BSSP) and forward sequential sensor placement (FSSP).

Combining data analytics methods and optimization algorithms effectively mitigates the limitations posed by noise and outliers in measured signals [28]. Data analytics techniques can be employed to preprocess and denoise the measured signals, reducing the impact of noise on subsequent analysis and removing outliers. Optimization algorithms can then be utilized to refine the data analytics parameters or optimize the selection and configuration of algorithms, leading to improved performance and more accurate results. The synergy between data analytics and optimization algorithms enables the development of advanced SHM systems that are robust, efficient, and capable of dealing with high noise levels. These systems have the ability to detect and characterize structural damage or anomalies with enhanced accuracy, even in challenging environments where the measured signals are corrupted by various sources of noise [29–32].

In this paper, a novel optimization algorithm, namely the Improved Reptile Search Algorithm (IRSA), is developed to optimize damage parameters and enhance the quality of the solution. Compared to its predecessor, the Reptile Search Algorithm (RSA) [33], the improved algorithm exhibits increased computational speed and accuracy. The superior performance of the proposed IRSA in finding global optima is demonstrated by solving several renowned benchmark problems. Furthermore, we employ the proposed IRSA to update damage parameters in numerical and experimental damage detection studies using the constructed objective function. The superiority of the proposed method over other state-of-the-art methods from the literature is further demonstrated.

In our proposed methodology, the contribution of each major component to the overall damage detection process can be described as follows:

1. Johansen cointegration is integral in mitigating non-stationary effects in FRFs by constructing a robust objective function that seeks a stationary common trend among a set of nonstationary FRFs.
2. Gaussian smoothing is implemented for effective noise reduction and overall data smoothing by augmenting the signal-to-noise ratio within the measured FRFs.
3. IRSA is employed to methodically optimize the parameters or weights associated with the objective function, derived from the cointegration and smoothing processes. Thereby this algorithm facilitates the accurate adjustments to our methodology, enabling it to adapt more effectively to the unique characteristics of the structural data under examination. This fine-tuning process holds the potential to significantly enhance the accuracy and efficiency of our damage detection approach.

To determine the distinct contributions of the individual components to the overall methodology, they are systematically analyzed in a one-by-one exclusion analysis

The contributions of the proposed method in the SHM field can be summarized as follows:

1. We introduce a novel application of Johansen cointegration as a data fusion technique, and showcase its ability to effectively handle outliers in FRF signals.
2. A Gaussian smoothing is shown effective for handling high-frequency noise while preserving more information and maintaining functionality.
3. Subsequently, a new metric based on the concepts of Mutual Information (MI), Johansen cointegration, and Gaussian smoothing is proposed to formulate a new objective function that is insensitive to highly correlated colored noise.
4. We further propose a robust objective function based on the proposed damage-sensitive feature (DSF) capable of handling outliers originating from non-stationary noise or measurement errors in FRF signals. Multiple ways of constructing the proposed objective function are investigated, with the most effective one identified.
5. The robustness of the proposed objective function for damage detection in structures with closely spaced eigenvalues is demonstrated. As mentioned earlier, we had established that this particular approach can be applied to systems with closely spaced eigenvalues. Therefore, we opted to conduct a numerical evaluation using a composite plate as a complex system that exemplifies the presence of closely spaced eigenvectors. This deliberate selection allows us to effectively showcase the capabilities and effectiveness of our proposed method.
6. We proposed a new and robust optimization algorithm based on the concept of the RSA, named IRSA, to optimize the proposed objective function for damage indices. The superior performance of the proposed optimization algorithm is demonstrated by comparing it to various optimization algorithms across well-established function benchmarks. The accuracy and robustness of the proposed optimization algorithm are also demonstrated through various cases, both numerical and experimental, by examining the central processing unit (CPU) performance of the optimization algorithm.
7. To evaluate the performance of the proposed method, we apply it to a damage detection study for laminated composite plates. We assess the impacts of varying boundary conditions and different E_1/E_2 ratios on the damage detection results for composite laminates. A comparative analysis with other state-of-the-art damage identification methods demonstrates the superiority of our proposed method.
8. Furthermore, the proposed method is validated through an experimental damage detection scenario conducted on steel beams, confirming its applicability to real-world problems.

In the subsequent sections, we delve into the specifics of the proposed technique, providing comprehensive details, and present the outcomes derived from both the experimental and numerical models.

2. Proposed methodology

Fig. 1 presents an overview of the damage detection methodology employed in this paper. The proposed approach encompasses three main steps: (1) simulating or measuring FRF data contaminated with an uncertain type of noise by either generating data using a numerical model or recording measurements from a real structure; (2) analyzing the input signals with Gaussian smoothing and Johansen integration to reduce high-frequency/low-frequency noise and remove outliers through the fusion of data through Johansen cointegration, and (3) constructing a novel objective function based on the concept of mutual information and optimizing it using the proposed optimization algorithm. The following sections provide details on the individual procedures.

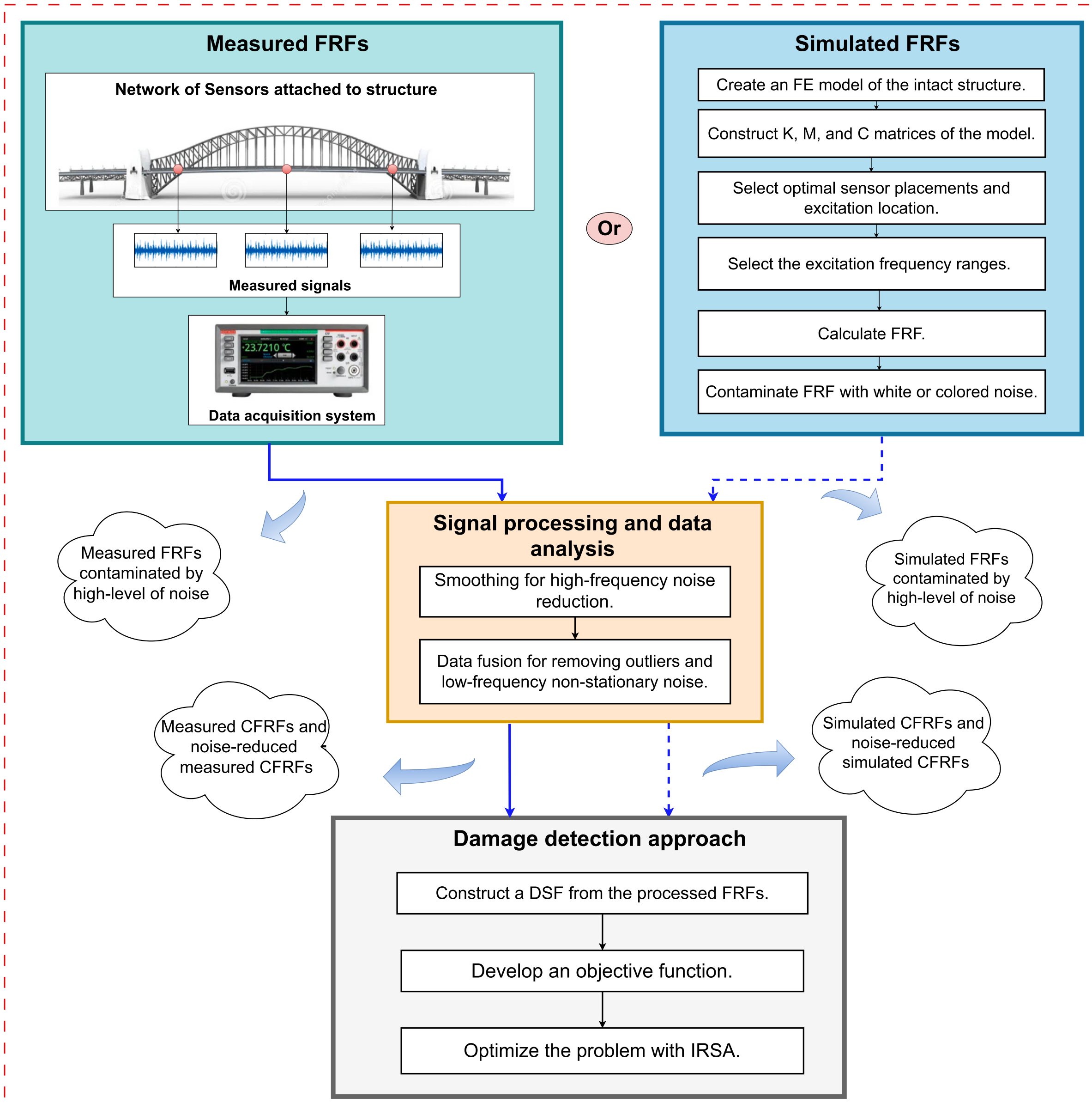

Fig. 1. Overview of the methodology steps of the proposed damage detection approach.

2.1. FRF simulation of damaged structures

Consider an n-DOF FE model of a system excited at its condensed master DOFs by a dynamic force vector $\bar{\mathbf{f}}$. The following differential equation can express a damaged model with the assumption that the damage only affects the stiffness matrix of the structure:

$$\bar{\mathbf{M}}\ddot{\mathbf{x}} + \bar{\mathbf{C}}\dot{\mathbf{x}} + \bar{\mathbf{K}}^{\mathrm{d}}\bar{\mathbf{x}} = \bar{\mathbf{f}} \tag{1}$$

where $\bar{\mathbf{K}}$, $\bar{\mathbf{M}}$, and $\bar{\mathbf{C}}$ denote, respectively, the condensed form of the stiffness, mass, and damping matrices and,

$$\bar{\mathbf{K}}^{\mathrm{d}} = \sum_{i=1}^{ne} \alpha_i \bar{\mathbf{k}}_i \tag{2}$$

is the matrix of stiffness of the damaged structure defined as the parameter of damage, assigned to the i^{th} element, multiplied by the stiffness matrix of the element in the global coordinate, shown as $\bar{\mathbf{k}}_i$, summed over all the ne elements; $\bar{\mathbf{M}}$ is the condensed mass matrix of the structure; $\bar{\mathbf{C}}$ is the Rayleigh damping obtained as $[\bar{\mathbf{C}}] = a[\bar{\mathbf{M}}] + b[\bar{\mathbf{K}}^{\mathrm{d}}]$, where a and b are constants determined by assuming 5% damping ratio for the two lowest modes of the structure.

Taking the Fourier transform of Eq. (1) results in:

$$-\omega^2\bar{\mathbf{M}}\bar{\mathbf{X}} + j\omega\,\bar{\mathbf{C}}\bar{\mathbf{X}} + \bar{\mathbf{K}}^{\mathrm{d}}\bar{\mathbf{X}} = \bar{\mathbf{F}} \tag{3}$$

As a special case, where the structure is excited by a range of frequencies $\boldsymbol{\omega}_k$, $\bar{\mathbf{F}}$ depends on the excitation frequency ω_k, while $\bar{\mathbf{X}}$ is the function of the vector of damage parameters $\boldsymbol{\alpha}_i$ as well as the excitation frequency ω_k. Accordingly, rearrangement of Eq. (3) gives the following equation:

$$\bar{\mathbf{X}}_k = \left(-\omega_k^2\bar{\mathbf{M}} + j\omega_k\,\bar{\mathbf{C}} + \bar{\mathbf{K}}^{\mathrm{d}}\right)^{-1}\bar{\mathbf{F}}_k \tag{4}$$

A more compact version of the expression (4) can be written as follows:

$$\bar{\mathbf{X}}_k = \mathbf{H}_k \times \mathbf{F}_k \tag{5}$$

where

$$\mathbf{H}_k = \left(-\omega_k^2\bar{\mathbf{M}} + j\omega_k\bar{\mathbf{C}} + \bar{\mathbf{K}}^{\mathrm{d}}\right)^{-1} \tag{6}$$

Different values of ω_k, corresponding to different excitation frequencies, are used in Eq. (6) to simulate the measured k^{th} FRF of a damaged structure, shown as $\mathbf{H}_k$, with rows corresponding to measurement locations and columns corresponding to excitation locations. The corresponding rows and columns of the obtained FRFs are chosen to find the final FRFs. Then, the obtained FRFs from different values of ω_k are concatenated to obtain one uniform FRF.

2.2. Selection of optimal excitation locations and frequency ranges

The following section outlines the optimization of both the range and location of excitation frequencies. In general, it is preferred to use frequencies sensitive to structural parameter variations. Based on the findings of Pedram et al. [34], selecting excitation frequencies near resonances proves advantageous as the structural response to small changes in structural parameters is more sensitive to variations in near-resonance frequency ranges. Moreover, the noise effect diminishes in the vicinity of resonances-a phenomenon also described by [19]. It is further desirable to diminish damping effects, even though it does not directly contribute to Eq. (6). The influence of damping on FRF decreases with increasing distance from resonances, thus, suggesting that the preferred excitation frequency ranges, from a damping perspective, should be further away from resonances. The selection of optimal excitation ranges entails a trade-off between maintaining a distance from resonant frequencies and remaining in close proximity to them. Therefore, this distance must be adjusted for each structure individually.

Obtaining a uniform FRF requires concatenating FRFs obtained from different excitations. With each iteration, the damage indices are adjusted, resulting in a shift in the computed FRF, $\mathbf{H}^{\text{c}}$. Accordingly, $\mathbf{H}^{\text{c}}$ requires adjustment with each iteration through an automated frequency-range selection program.

The selection of the excitation locations is an essential factor for improving the accuracy of model-updating algorithms [35]. The proposed model-updating approach based on FRFs adheres to this principle. According to [36], the following method can be used to obtain such optimized excitation locations:

$$\boldsymbol{\Lambda} = \sum_{j=1}^{N} \sqrt{\sum_{i=1}^{n} \left(\mathbf{H}_{ij}\right)^2} \tag{7}$$

Firstly, the number of excitation locations must be determined. Subsequently, the entries of Λ are sorted in descending order so that the DOFs corresponding to the prespecified number of most significant entries of Λ can be determined to be optimal excitation locations. FE models of intact structures are used to determine the optimal excitation locations. This ensures that they are not updated during the iterations.

2.3. Contaminating input signals with a colored noise

Thus far, we have discussed how FRFs can be numerically simulated for damage detection. Next, the columns of the obtained FRFs $\mathbf{H}$ are contaminated with colored noise having the theoretical spectral characteristic $|f|^{-\beta}$ where f and β correspond to the cyclic frequency and a real number between -2 and 2, respectively [37]. The following are well-known types of colored noise that can be generated in MATLAB:

1. Brown noise (Brownian process) with $\beta = 2$;
2. Pink noise or $\frac{1}{f}$ noise with $\beta = 1$;
3. White noise with $\beta = 0$;
4. Blue noise, also known as azure noise, with $\beta = -1$ and;
5. Purple noise, also known as violet noise, with $\beta = -2$.

Fig. 2 displays the Power Spectral Densities (PSDs) of various theoretical and MATLAB-generated noise signals. The logarithmic plots depicted in the figure demonstrate that the noise energy varies according to the frequency range. Accordingly, brown noise introduces the most severe case of low-frequency noise, causing the contaminated signal to be more nonstationary. Therefore, this work focuses on studying brown noise for damage detection using simulated FRF signals.

To obtain different levels of signal-to-noise ratio (SNR), the rows of the generated FRF matrix ($\mathbf{H}$) are contaminated with colored noise. The SNRs are set at 20 and 10 dB in this study, where a value of 10 dB corresponds to more severe signal contamination compared to a value of 20 dB. To contaminate an FRF signal with colored brown noise, the following procedures are implemented:

Firstly, noise power and signal power are calculated as follows:

$$P_{\mathbf{H}(:,i)} = \frac{1}{N} \sum_{n=1}^{n=N} \mathbf{H}(n,i)^2 \tag{8}$$

$$P_{\text{noise}} = \frac{1}{N} \sum_{n=1}^{n=N} \epsilon(n)^2 \tag{9}$$

where $\mathbf{H}(:,i)$ and ϵ denote the i^{th} column of the $\mathbf{H}$ and the simulated noise in MATLAB, respectively. To achieve the specified target values for the SNR in dB, the simulated noise is normalized by the factor λ as follows:

$$\text{SNR}_{\text{db}} = 10 \log_{10} \left(\frac{P_{\mathbf{H}(:,i)}}{\lambda^2 \, P_{\text{noise}}} \right) \tag{10}$$

Accordingly, the i^{th} FRF noisy column can be obtained in the following way:

$$\mathbf{H}_{\text{noisy}}(:,i) = \mathbf{H}(:,i) + \lambda \, \epsilon^{\text{t}} \tag{11}$$

where $\mathbf{H}_{\text{noisy}}(:,i)$ is the i^{th} column of the noise polluted $\mathbf{H}$, and superscript t denotes the transpose operator.

2.4. Using Gaussian smoothing to smooth noisy FRFs

To reduce the intensity of high-frequency noise, it is essential to implement an effective smoothing technique prior to signal processing. One approach is to employ smoothing techniques to enhance the quality of the signals. Various methods for smoothing signals include moving average, Gaussian smoothing, Savitzky-Golay filtering, median filtering, and Wavelet denoising [39]. By applying a suitable smoothing method, the contaminating noise can be significantly attenuated. This will result in cleaner and more reliable data and enhance the accuracy and robustness of the subsequent analysis. However, the selected smoothing technique must also be able to preserve as much information as possible in the data. In this paper, we use Gaussian smoothing as a robust smoothing technique over other options for two main reasons: (1) it has only one hyperparameter, and (2) it produces satisfactory smoothing results.

Gaussian smoothing, also known as Gaussian blur, is a widely used technique in signal and image processing for reducing the effect of noise. It is based on the mathematical concept of convolving a signal with a Gaussian kernel that has a bell-shaped distribution. The main idea behind Gaussian smoothing is to replace each data point in a signal with a weighted average of its neighboring points. The Gaussian kernel assigns higher weights to the data points closer to the center and lower weights to the farther-distanced points, resulting in a smooth combination of neighboring values. The Gaussian smoothing formula can be written as follows:

$$\bar{S}(i) = \frac{\sum_{j=-\infty}^{\infty} S(j).G(i-j)}{\sum_{j=-\infty}^{\infty} G(i-j)} \tag{12}$$

where:

- $\bar{S}(i)$ represents the value of the smoothed signal at index i.
- $S(j)$ represents the value of the original signal at index j
- The sums extend from $-\infty$ to ∞, but in practice, they are calculated only within a finite range determined by the kernel size.

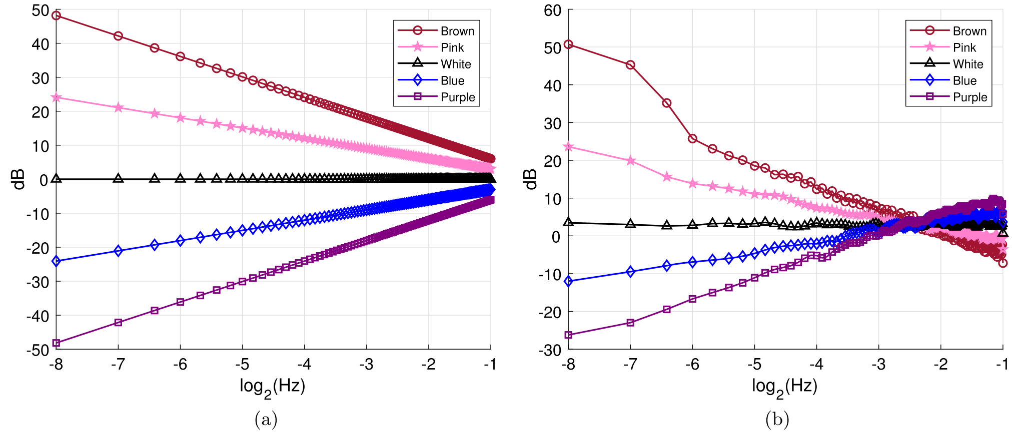

Fig. 2. Log-log plots of the PSD of (a) theoretical and (b) MATLAB-generated noise signals of various colors [38].

Note that Eq, (12) can also be described as the convolution between the signal and the Gaussian kernel normalized by the assigned Gaussian weights. The Gaussian kernel can be defined as follows:

$$G(k) = \frac{1}{\sqrt{2\pi\sigma^2}}.e^{\frac{-k^2}{2\sigma^2}} \tag{13}$$

where $G(k)$ represents the value of the Gaussian kernel at index k and σ is the standard deviation of the Gaussian distribution. The Gaussian kernel is centered around $k = 0$ and has a bell-shaped distribution, the value of which decreases exponentially as the distance from the center increases. As such, σ is the only hyperparameter of the Gaussian smoothing technique, the larger value of which will impose a stronger smoothing effect on the signal. Hence, the algorithm needs to be set to optimize the value of σ along with damage parameters in a way to minimize the to-be-proposed objective function.

2.5. Handling of colored noise contamination and outliers with Johansen cointegration

Following the preceding description, the columns of the generated FRF (Section 2.1) are contaminated with colored noise (Section 2.3). To subsequently derive a unique signal free of nonstationary colored noise, the columns of the contaminated FRF are cointegrated utilizing the equation below:

$$\boldsymbol{\Psi} = \sum_{j=1}^{j=p} a_j\, \bar{\mathbf{H}}_{\text{noisy}}(:, j) \tag{14}$$

where $\boldsymbol{\Psi}$ represents the residuals of the Johansen cointegration for the noisy FRF matrix $\bar{\mathbf{H}}_{\text{noisy}}$, termed CIFRF; p represents column numbers (excitation locations) in $\bar{\mathbf{H}}_{\text{noisy}}$; and a_j is the cointegration coefficient obtained for the j^{th} row as indicated in Eq. (14).

It is important to note that, from a technical point, the Johansen cointegration process can yield more than one vector of a_j. These vectors are eigenvectors that correspond to the eigenvalue problem of Johansen cointegration. Therefore, the first eigenvector, which corresponds to the largest eigenvalue, represents a stationary FRF column combination, represented by CIFRF$_1$ in Eq. (14). Accordingly, the second eigenvector produces a combination of FRF columns that is less stationary, expressed as CIFRF$_2$.[1] Hence, in this study, CIFRF$_1$ is selected as a DSF. The superiority of CIFRF$_1$ over CIFRF$_2$ is demonstrated in the subsequent section by comparing the results obtained when using either CIFRF$_1$ or CIFRF$_2$ as the DSF. Throughout the remainder of this paper, unless stated otherwise, CIFRF$_1$ is referred to as the selected DSF for the sake of simplicity.

Furthermore, from a technical perspective, the columns of $\bar{\mathbf{H}}_{\text{noisy}}$ need to be nonstationary and integrated in the same order for the Johansen cointegration to operate. For this reason, the Kwiatkowski—Phillips—Schmidt—Shin (KPSS) test is applied to each column of $\bar{\mathbf{H}}_{\text{noisy}}$ and $\Delta\bar{\mathbf{H}}_{\text{noisy}}$ to determine whether this property complies. Theoretically, it is required that all signals introduced in the Johansen cointegration procedure must be of the same order of non-stationarity. However, Cross and Worden [21] suggested that this requirement could be relaxed when employing cointegration in the context of SHM applications.

As stated previously, in this study, Johansen cointegration is employed as a data fusion technique for handling outliers and colored noise in FRFs. While the former relates primarily to experimental data, the latter applied mainly to numerical simulations. It is noted that the term outlier handling is a general term that also incorporates other types of noise contamination. In this paper, we use the term outlier for experimental measurement errors as no pre-knowledge about the type of noise contamination exists. Although one may investigate the type of noise by further comparing the measured FRF with the reference FRF obtained from a numerical simulation, we simply propose Johansen cointegration as an effective tool to deal with any type of error in the regenerated FRF. Here, the objective is to leverage the capabilities of Johansen cointegration to identify outliers within the input signals and fuse data from multiple sources, thereby enhancing the overall quality and reliability of the dataset.

Outlier detection plays a critical role in data analysis by identifying observations that deviate from expected patterns. By applying the Johansen cointegration method, the objective is to identify the relationship among a set of FRFs and thereby reduce the effect of outliers in one particular variable at a given point in the analysis. Using Johansen cointegration as a means of data fusion involves integrating information from multiple FRFs to obtain a more comprehensive and accurate representation of the phenomenon under study. By examining the cointegration relationships among FRFs at different locations, this study seeks to identify common trends among variables as a data fusion approach.

2.6. Proposed damage detection method

This section discusses the construction of the objective function to be minimized for damage parameters and the smoothing factor. In the following, we define the objective function based on the mutual information shared between computed and measured metrics at specific excited and measured DOFs of the structure. The primary reason for adopting the concept of mutual information instead of minimizing the

[1] Consider that the total number of columns in the FRF matrix is less than the number of possible cointegration residuals.

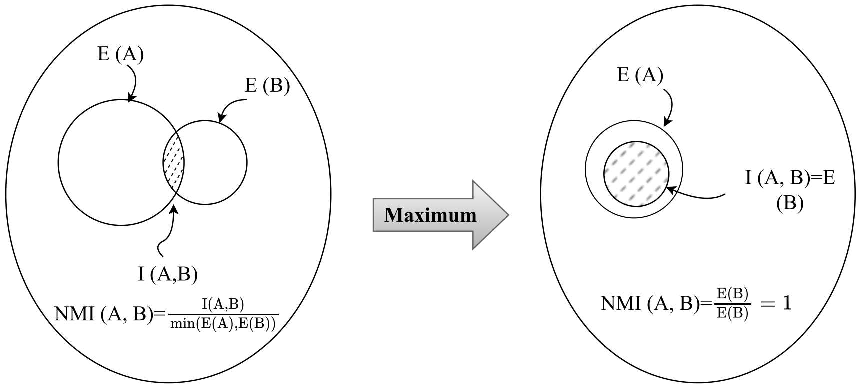

Fig. 3. The maximum value of NMI is equal to 1.

mathematical distance between the obtained metrics is rationalized as follows. The utilization of information distance considers the semantic meaning or similarity between vectors, rather than focusing only on their mathematical differences. Consequently, it enables a deeper exploration of the underlying information or patterns in the data, leading to more meaningful insights regarding similarities or differences in FRFs.

Assume $\mathbf{H}$ be the FRFs of the intact structure. Subsequently, $\bar{\mathbf{H}}_{\text{noisy}}$ denotes the smoothed version of the noisy FRFs regenerated from the damaged structure. The corresponding cointegration vector of each matrix is obtained using Eq. (14) as $\boldsymbol{\Psi}_{\text{num}}$ and $\boldsymbol{\Psi}_{\text{exp}}$ for the intact and damaged structures, respectively. The objective is to minimize the distance between these two matrices as much as possible. The distance between two finite FRFs, however, may bring about some errors, such as neglecting the effect of higher-order components. Moreover, the direct distance between two FRFs is more sensitive to noise. Therefore, in this paper, we propose to maximize the mutual information distance between $\boldsymbol{\Psi}_{\text{num}}$ and $\boldsymbol{\Psi}_{\text{exp}}$. As such, the proposed objective function aims to maximize the normalized mutual information between $\boldsymbol{\Psi}_{\text{num}}$ and $\boldsymbol{\Psi}_{\text{exp}}$ as follows:

$$\text{NMI}(\boldsymbol{\Psi}_{\text{num}}, \boldsymbol{\Psi}_{\text{exp}}) = \frac{\text{I}(\boldsymbol{\Psi}_{\text{num}}, \boldsymbol{\Psi}_{\text{exp}})}{\min\left(\text{E}(\boldsymbol{\Psi}_{\text{num}}), \text{E}(\boldsymbol{\Psi}_{\text{exp}})\right)} \tag{15}$$

where E(.) and I(.) represent the Shannon entropy and mutual information, respectively, and can be obtained through the following equations:

$$\text{E}(\mathbf{X}) = -\sum_{x\in\mathbf{X}} \text{P}(x)\log \text{P}(x) \tag{16}$$

and

$$\text{I}(\mathbf{X};\mathbf{Y}) = \sum_{y\in\mathbf{Y}}\sum_{x\in\mathbf{X}} \text{P}_{(\mathbf{X},\mathbf{Y})}(x,y)\log\left(\frac{\text{P}_{(\mathbf{X},\mathbf{Y})}(x,y)}{\text{P}_{\mathbf{X}}(x)\text{P}_{\mathbf{Y}}(y)}\right) \tag{17}$$

In the above, $\text{P}_{\mathbf{X}}(x)$, $\text{P}_{\mathbf{Y}}(y)$, and $\text{P}_{(\mathbf{X},\mathbf{Y})}(x,y)$ are the marginal probability of $\mathbf{X}$ and $\mathbf{Y}$ and the joint probability of $\mathbf{X}$ and $\mathbf{Y}$, respectively. The procedure presented by [40,41] is followed to obtain the value for the above probabilities. The readers are referred to these papers for further details. Note that by dividing the numerator of (15) (I) by the minimum entropy value in the denominator, the obtained value of NMI is scaled to the range of [0, 1]. Here, the denominator is a scaling factor ensuring that the NMI value is always less than or equal to 1 (Fig. 3).

Finally, the proposed objective function is obtained by inverting (15) as follows:

$$\min_{\alpha;\sigma} \frac{1}{\text{NMI}(\boldsymbol{\Psi}_{\text{num}}, \boldsymbol{\Psi}_{\text{exp}})} \tag{18}$$

where the objective is to obtain the optimal value for $\boldsymbol{\alpha}$ (vector of damage indices) and σ (standard deviation of Gaussian smoothing) that minimizes the inverse of the mutual information between $\boldsymbol{\Psi}_{\text{num}}$ and $\boldsymbol{\Psi}_{\text{exp}}$. Note that the possible maximum value for the aforementioned objective function is 1.

2.7. New optimization algorithm: Improved Reptile Search Algorithm (IRSA)

A recent metaheuristic optimization algorithm, the Reptile Search Algorithm (RSA) [33], is based on the hunting behavior of crocodiles. RSA belongs to the category of swarm intelligence algorithms that leverage competition and cooperation within a group of reptiles. By mimicking natural crocodile behaviors that search for food in their natural habitat, the algorithm attempts to find the global optimum of an optimization problem. The main advantages of RSA over other metaheuristic algorithms are its simplicity, flexibility, and efficiency. RSA has been successfully applied in various domains, such as engineering design, power systems, and image processing.

In this paper, we propose an advanced RSA algorithm, named the Improved RSA (IRSA) algorithm, that enhances several features of RSA and thereby improves its performance across a wide range of benchmark functions. Unlike the previous version, which only works well on a few specific benchmarks (see Table 1) [33], our proposed optimization method (IRSA) demonstrates superior performance across broader benchmark functions where the RSA does not perform well. By implementing these improvements, we achieve enhanced optimization capabilities and expand the applicability of RSA in several domains. To demonstrate this, the performance of the proposed IRSA algorithm is compared to that of several other algorithms in the following sections.

The following changes have been implemented to improve different aspects of the original RSA:

- Initialization phase: Initialization is a critical feature of optimization algorithms as it profoundly influences the final solution. The initialization process is the first step in setting up an optimization algorithm. This step can significantly impact the convergence speed of the algorithm and the ultimate optimal outcome. As such, the choice of initialization method is critical in ensuring the success and efficiency of an optimization algorithm.
  RSA makes a uniform distribution assumption for initializing variables. While this assumption may work in some cases due to assigning unbiased probabilities to the initialization, it somehow contradicts the nature of SHM problems. It is known in SHM that most of the damage parameters take the value of zero, and there is usually a sparse number of variables whose value is non-zero. Moreover, it is known that the variables are bounded between 0 and 1. By incorporating this prior knowledge into the initialization process, we are able to obtain a more robust initialization for the problem. Therefore, a one-sided standard normal distribution is assumed for

the variables in the SHM problem discussed in this paper with the following probability density function (PDF):

$$f(x) = (\frac{1}{\sqrt{2\pi}}) * exp\left\{\frac{-x^2}{2}\right\}; \qquad x \in \mathbb{R}. \tag{19}$$

Where the random variable x is an independent and identically distributed (iid) random variable with a mean of 0 and standard deviation of 1.

However, in a general case, where foreknowledge about the distribution of the variables does not exist assuming a random normal distribution may benefit the algorithm due to the following reasons:

- Normal distribution: The preference for using normal distribution over uniform distribution for initialization is application-dependent. While uniform initialization may yield satisfactory results in certain scenarios, there have been several applications where initialization based on the normal distribution has been favored [42].
- Symmetric and bell-shaped distribution: The symmetric and bell-shaped configuration of the PDF for the normal distribution allows for generating random numbers that are more likely to be closer, rather than farther, to the mean. This property of the normal distribution makes it suitable for modeling many natural phenomena that exhibit a degree of symmetry.
- Central limit theorem: According to the central limit theorem, the distribution of the limit sum of a set of iid variables approaches a normal distribution. This property is, in fact, independent of the underlying distribution of the individual random variables.
- More flexibility: The function generating normal distribution is more versatile compared to that of a uniform distribution. This is because it allows for generating random numbers with different means and standard deviations by applying appropriate scaling and shifting operations.

To achieve initialization following standard normal distribution, we use the function “randn” in MATLAB. We also use MATLAB’s “rng(‘shuffle’)” function to generate different populations in each iteration. “rng(‘shuffle’)” function is called to set the seed for the random number generator to the current time, which ensures that the random numbers generated by the function “randn” are different in each iteration of the program. The use of this function ensures the generation of diverse populations. By increasing the diversity of the search space, the quality of the generated solutions is improved.

- Dynamic Evolutionary Sense (DES): Evolutionary Sense (ES)–a function of the preassigned total number of iterations–is a variable that controls generating a random population at the beginning of the program. It is defined in RSA as follows:

$$\text{ES} = 2 \times rand \times \left(1 - (\frac{t}{T})^2\right) \tag{20}$$

where T is the total number of iterations, and $rand$ is a random variable that follows a uniform distribution.

The Dynamic Evolutionary Sense (DES) is defined to be changed at each iteration as follows:

$$\text{DES}(t) = 2 \times rand(t) \times \left(1 - (\frac{t}{T})^2\right) \tag{21}$$

where T and t are the total number of iterations and the running iteration, respectively, and $rand(t)$ is a random variable, selected at the t^{th} iteration, that follows a standard normal distribution. The proposed IRSA updates this parameter in each iteration.

- Subdivision of the search space: The RSA algorithm is programmed to identify the best solution by searching the entire possible search space. Here, in the proposed IRSA, the search space is proposed to be subdivided based on the concept of finite elements (FE) in mechanical engineering. As such, by leveraging finite element analysis, the search space is divided into different finite regions, and each region is searched for the best solution individually. The overall system performance can be enhanced by considering the interactions between neighboring regions of the search space. This approach allows for more localized and focused optimization, where the design variables within each region are adjusted independently.
- Boundary checking: In constraint optimization, RSA checks the identified best solutions against acceptable boundaries once at the end of iterations. Here, we propose to check the obtained solution against the allowed limits in each region (each FE) of the search space at each iteration. As a result, out-of-the-range responses will be discarded at each iteration automatically.
- Parameter updates: RSA considers a static value for α, and β parameters. However, we propose to update these parameters at each iteration to lead the program to the best solution region. In the proposed IRSA, α and β are essential factors that control the behavior of the optimization process and are proposed to be updated based on the following rules:

$$\alpha(t) = \alpha_1 \times randn \times \left(1 - (\frac{t}{T})^2\right), \tag{22}$$

and,

$$\beta(t) = \beta_1 \times randn \times \left(1 - (\frac{t}{T})^2\right). \tag{23}$$

In summary, the proposed IRSA optimization process begins with generating a random set of candidate solutions (population). IRSA’s search mechanisms explore various positions of the near-optimal solution during the trajectory of repetition. The proposed IRSA process replaces each solution’s position with the best-obtained solution. The search processes have been divided into two main methods (exploration and exploitation) with four strategies to highlight exploration and exploitation. An exploration method involves high walking and a belly walking strategy, and an exploration method involves hunting coordination and cooperation [33]. A candidate solution attempts to broaden the scope of the search when $t \leq \frac{T}{2}$ and aims to reach a near-optimal solution when $t > \frac{T}{2}$. A high-walking movement strategy is used during the exploration phase when $t \leq \frac{T}{4}$ and a movement strategy of belly walking is used when $t > \frac{T}{4}$ and $t \leq 2\frac{T}{4}$. As part of the exploitation phase, a hunting coordination strategy is implemented when $t > 2\frac{T}{4}$ and $t \leq 3\frac{T}{4}$. Otherwise, a strategy of hunting cooperation is used when $t \leq T$ and $t > 3\frac{T}{4}$. The proposed IRSA process is terminated once the end criterion has been satisfied. This is when the maximum iteration is reached or the difference between two successive values of the objective function is less than a threshold. Algorithm 1 provides the pseudo-code for the proposed IRSA. Fig. 4 shows the flowchart of the proposed IRSA.

2.7.1. Comparing the proposed IRSA with existing algorithms

Table 2 presents a comparison of the performance between the proposed IRSA and some other meta-heuristic algorithms, including the previous version (RSA), grasshopper optimization algorithm (GOA), salp swarm algorithm (SSA), whale optimization algorithm (WOA), sine cosine algorithm (SCA), dragonfly algorithm (DA), grey wolf optimizer (GWO), particle swarm optimization (PSO), ant lion optimizer (ALO), marine predators Algorithm (MPA), equilibrium optimizer (EO), and covariance matrix adaptation evolution strategy (CMAES). The specifications for this comparison are consistent with those outlined in [33] with dimensions of 500 and a total of 500 iterations. As depicted in Table 2, most of the previous algorithms encountered challenges in solving the benchmark problems [33]. However, from examining the table, it is evident that the proposed IRSA outperforms other algorithms by providing a better average fitness value, demonstrated by its rank, i.e., 1,

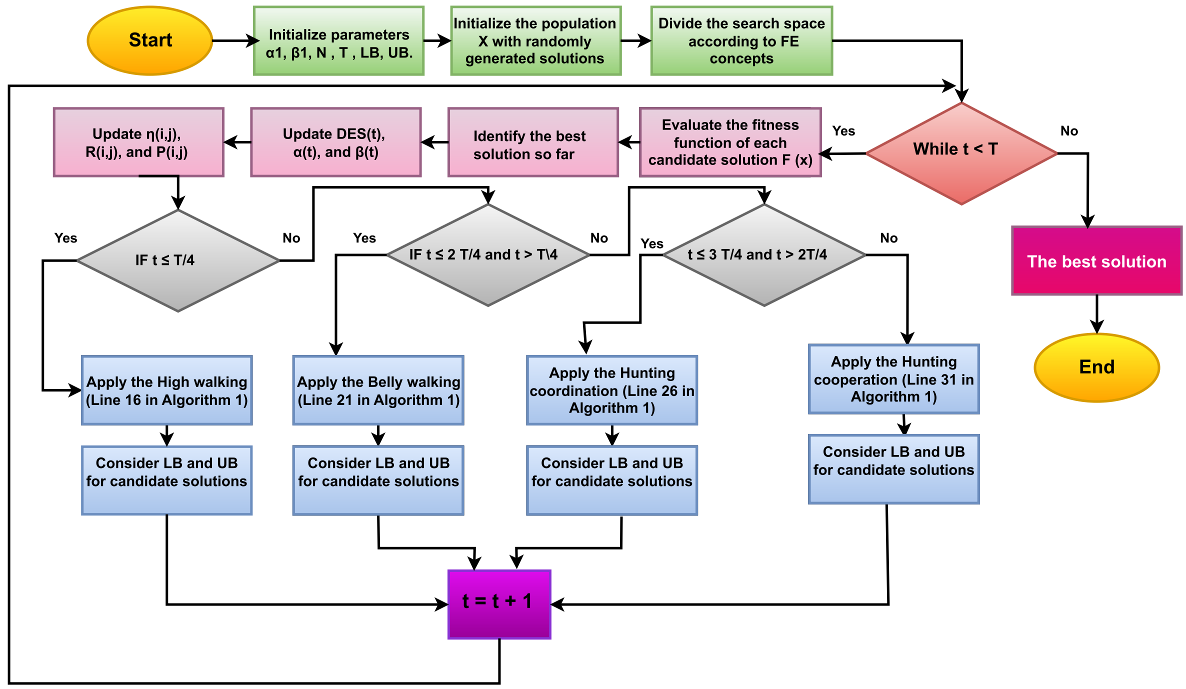

Fig. 4. Flowchart of the proposed IRSA.

Table 1
Benchmark functions.

Fun	Description	Type	Dimensions	Range	f_{min}
F1	$f(x) = \sum_{i=1}^{n} \left(\left[x_i + 0.5\right]\right)^2)$	Unimodal	30, 100, 500, 1000	$[-100, 100]$	0
F2	$f(x) = \sum_{i=1}^{n} \left(-x_i \sin\left(\sqrt{\lvert x_i \rvert}\right)\right)$	Multimodal	30, 100, 500, 1000	$[-500, 500]$	$-418.9829 \times n$
F3	$f(x) = 0.1 \left(\sin^2(3\pi x_i) + \sum_{i=1}^{n} \left(x_i - 1\right)^2\right)$ $\left[1 + \sin^2(3\pi x_i + 1)\right] + (x_n - 1)^2 + \sin^2(2\pi x_n)$ $+ \sum_{i=1}^{n} u(x_i, 5, 100, 4)$	Multimodal	30, 100, 500, 1000	$[-50, 50]$	0
F4	$f(x) = \sum_{i=1}^{11} \left[a_i - \frac{x_i(b_i^2 + b_i x_2)}{b_i^2 + b_i x_3 + x_4}\right]^2$	Fixed-dimension multimodal	4	$[-5, 5]$	0.00030
F5	$f(x) = -\sum_{i=1}^{5} \left[(X - a_i)(X - a_i)^T + c_i\right]^{-1}$	Fixed-dimension multimodal	4	$[0, 1]$	-10.1532
F6	$f(x) = -\sum_{i=1}^{7} \left[(X - a_i)(X - a_i)^T + c_i\right]^{-1}$	Fixed-dimension multimodal	4	$[0, 1]$	-10.4028
F7	$f(x) = -\sum_{i=1}^{10} \left[(X - a_i)(X - a_i)^T + c_i\right]^{-1}$	Fixed-dimension multimodal	4	$[0, 1]$	-10.5363

in most cases. Furthermore, it can be observed that the performance of the proposed IRSA is superior compared to other methods at high dimensions (500). The results clearly illustrate that our proposed optimization algorithm excels in optimizing various benchmark objective functions. Our algorithm demonstrates the ability to effectively address complex optimization problems and deliver highly accurate solutions across a diverse range of benchmark scenarios.

2.8. Damage identification accuracy indicators

To evaluate the accuracy of the obtained results, the following three accuracy indicators are used, as described in [43]:

1. Closeness index (CI): It is defined as the difference between actual and computed damage index vectors expressed as:

$$\mathrm{CI} = 1 - \frac{\| P^r - P^c \|_2}{\| P^r \|_2} \tag{24}$$

where P^r and P^c are the vectors of synthesized and predicted damage indices, respectively. An ideal match is achieved when CI $=$ 1.

2. Mean square error (MSE): This error is defined as the sum of the absolute differences between the predicted and synthesized damage parameters, normalized by the number of damaged elements in the synthesized model. MSE is calculated as follows:

$$\mathrm{MSE} = \frac{1}{de} \sum_{e=1}^{de} |p_e^r - p_e^c|, \quad 0 \leq \mathrm{MSE} \tag{25}$$

where p_e^r and p_e^c are the synthesized and predicted damage parameters for the e^{th} element.

3. Relative error (RE): It can be defined as follows:

$$\mathrm{RE} = \frac{\sum_{e=1}^{n} |p_e^r| - \sum_{e=1}^{n} |p_e^c|}{\sum_{e=1}^{n} |p_e^r|}, \quad -1 \leq \mathrm{RE} \leq 1 \tag{26}$$

where n denotes the number of all elements regardless of their health condition. A more accurate prediction of damage indices will result in smaller MSE and RE values.

Table 2
IRSA results applying unimodal and multimodal test functions, as well as fixed-dimension multimodal benchmark functions.

Fun	Measure	RSA	GOA	SSA	WOA	SCA	DA	GWO	PSO	ALO	MPA	EO	CMA-ES	IRSA
F1	Worst	1.25E+02	8.08E+05	1.05E+06	1.04E+02	2.69E+05	3.58E+05	1.63E+02	2.30E+05	1.09E+06	1.08E+02	1.19E+02	5.00E+02	1.03E+02
	Average	1.24E+02	7.61E+05	9.53E+05	1.01E+02	2.52E+05	3.15E+05	1.45E+02	2.27E+05	1.00E+06	1.07E+02	1.18E+02	4.89E+02	1.00E+02
	Best	1.24E+02	7.33E+05	8.59E+05	9.86E+01	2.37E+05	2.31E+05	1.20E+02	2.22E+05	8.73E+05	1.06E+02	1.17E+02	4.81E+02	9.80E+01
	STD	1.97E-01	4.13E+04	9.81E+04	2.62E+00	1.63E+04	7.24E+04	2.24E+01	4.29E+03	1.14E+05	1.44E+00	9.18E-01	9.39E+00	4.13E+04
	Rank	5	11	12	2	9	10	6	8	12	3	4	6	1
F2	Worst	-7.46E+04	-3.32E+04	-2.67E+04	-1.26E+05	-1.21E+04	-1.50E+04	-1.02E+04	-9.56E+03	-9.03E+04	-5.10E+04	-3.85E+04	-6.06E+04	-1.20E+05
	Average	-7.86E+04	-3.70E+04	-3.25E+04	-1.39E+05	-1.33E+04	-1.70E+04	-2.91E+04	-1.19E+04	-9.03E+04	-5.53E+04	-4.26E+04	-6.64E+04	-1.30E+05
	Best	-8.10E+04	-3.95E+04	-3.73E+04	-1.50E+05	-1.45E+04	-1.90E+04	-3.63E+04	-1.56E+04	-9.03E+04	-5.96E+04	-4.58E+04	-7.17E+04	-1.40E+05
	STD	2.78E+03	2.69E+03	4.71E+03	9.97E+03	1.04E+03	1.64E+03	1.26E+04	2.85E+03	0.00E+00	4.72E+03	3.26E+03	5.66E+03	9.99E+03
	Rank	4	8	9	2	12	11	10	12	3	6	7	5	1
F3	Worst	5.00E+01	7.80E+09	8.62E+09	4.78E+01	1.06E+10	2.76E+09	3.06E+02	2.83E+08	7.83E+09	4.98E+01	4.98E+01	2.15E+02	4.77E+01
	Average	5.00E+01	7.20E+09	7.83E+09	3.90E+01	8.82E+09	1.59E+09	2.04E+02	2.64E+08	7.23E+09	4.98E+01	4.96E+01	1.97E+02	3.80E+01
	Best	5.00E+01	6.57E+09	7.27E+09	3.01E+01	6.56E+09	1.12E+09	1.05E+02	2.45E+08	6.63E+09	4.98E+01	4.92E+01	1.82E+02	2.90E+01
	STD	1.19E+03	6.05E+08	6.34E+08	8.05E+00	1.72E+09	7.84E+08	8.38E+01	1.55E+07	5.79E+08	3.71E-02	2.93E-01	1.39E+01	8.04E+00
	Rank	5	10	12	2	13	9	7	8	11	4	3	6	1
F4	Worst	8.39E-04	2.18E-02	2.08E-02	1.52E-03	1.91E-03	2.04E-02	2.04E-02	9.93E-04	2.04E-02	3.07E-04	3.53E-04	0.00E+00	3.04E-04
	Average	5.76E-04	9.79E-03	4.80E-03	7.74E-04	1.28E-03	5.72E-03	8.45E-03	9.20E-04	4.95E-03	3.07E-04	3.21E-04	0.00E+00	3.04E-04
	Best	3.64E-04	7.85E-04	7.43E-04	3.13E-04	6.92E-04	1.50E-03	3.08E-04	8.66E-04	7.78E-04	3.07E-04	3.08E-04	0.00E+00	3.04E-04
	STD	2.24E-04	1.05E-02	8.95E-03	4.56E-04	4.90E-04	8.19E-03	1.09E-02	6.64E-05	8.65E-03	2.90E-15	1.98E-05	0.00E+00	2.91E-15
	Rank	5	13	9	6	8	11	12	7	10	3	4	1	2
F5	Worst	-5.06E+00	-2.68E+00	-5.06E+00	-5.05E+00	-4.96E-01	-2.63E+00	-1.01E+01	-2.63E+00	-2.68E+00	-1.02E+01	-2.94E-01	-1.02E+01	-1.01E+01
	Average	-9.13E+00	-6.15E+00	-6.08E+00	-8.07E+00	-8.94E-01	-6.63E+00	-1.01E+01	-7.15E+00	-4.61E+00	-1.02E+01	-4.66E-01	-1.02E+01	-1.01E+01
	Best	-1.02E+01	-1.02E+01	-1.02E+01	-1.01E+01	-2.10E+00	-1.02E+01	-1.02E+01	-1.02E+01	-5.10E+00	-1.02E+01	-7.11E-01	-1.02E+01	-1.01E+01
	STD	2.28E+00	3.78E+00	2.27E+00	2.75E+00	6.93E-01	3.37E+00	2.99E-03	4.11E+00	1.08E+00	1.78E-11	1.59E-01	0.00E+00	0.00E+00
	Rank	5	9	10	6	12	8	4	7	11	2	13	2	1
F6	Worst	-5.09E+00	-2.75E+00	-3.72E+00	-2.94E-01	-9.06E-01	-2.75E+00	-1.04E+01	-2.75E+00	-3.72E+00	-1.04E+01	-5.09E+00	-1.04E+01	-1.00E+01
	Average	-9.25E+00	-7.34E+00	-8.01E+00	-5.56E-01	-1.90E+00	-6.38E+00	-1.04E+01	-6.47E+00	-7.73E+00	-1.04E+01	-9.34E+00	-1.04E+01	-1.00E+01
	Best	-1.04E+01	-1.04E+01	-1.04E+01	-8.58E-01	-4.02E+00	-1.03E+01	-1.04E+01	-1.04E+01	-1.04E+01	-1.04E+01	-1.04E+01	-1.04E+01	-1.00E+01
	STD	2.33E+00	4.19E+00	3.31E+00	2.72E-01	1.43E+00	3.54E+00	1.34E-03	3.68E+00	3.66E+00	1.04E-11	2.38E+00	0.00E+00	0.00E+00
	Rank	6	9	7	13	12	11	2	10	8	2	5	2	1
F7	Worst	-2.87E+00	-1.68E+00	-1.05E+01	-5.10E+00	-2.46E+00	-1.68E+00	-1.05E+01	-1.05E+01	-3.84E+00	-7.89E-01	-3.84E+00	-1.05E+01	-1.03E+01
	Average	-6.59E+00	-4.26E+00	-1.05E+01	-9.42E+00	-4.14E+00	-6.52E+00	-1.05E+01	-1.05E+01	-9.20E+00	-2.09E+00	-9.20E+00	-1.05E+01	-1.03E+01
	Best	-1.05E+01	-1.05E+01	-1.05E+01	-1.05E+01	-7.27E+00	-1.05E+01	-1.05E+01	-1.05E+01	-1.05E+01	-5.13E+00	-1.05E+01	-1.05E+01	-1.03E+01
	STD	3.69E+00	3.60E+00	2.10E-11	2.42E+00	1.90E+00	3.74E+00	1.98E-03	1.54E-15	3.00E+00	1.90E+00	3.00E+00	0.00E+00	0.00E+00
	Rank	8	10	6	5	12	11	3	4	13	8	7	2	1
	Final Ranking	5	10	9	6	12	11	7	8	13	4	3	2	1

Algorithm 1 Pseudo-code for the proposed IRSA.

Determine Objective Function $F(x)$.
Initialize parameters α_1, β_1, N, T, LB, UB.
Initialize the population X with randomly generated solutions.
while $t < T$ **do**
  Evaluate the fitness function of each candidate solution $F(x)$.
  Identify the best solution so far.
  $DES(t) = 2 \times randn \times \left(1 - (\frac{t}{T})^2\right)$,
  $\alpha(t) = \alpha_1 \times randn \times \left(1 - (\frac{t}{T})^2\right)$,
  $\beta(t) = \beta_1 \times randn \times \left(1 - (\frac{t}{T})^2\right)$,
  for $i = 1 : N$ **do**
    for $j = 1 : n$ **do**
      $\eta(i,j) = Best_j(t) \times P_{(i,j)}$,
      $R_{(i,j)} = \frac{Best_j(t) - x_{(r_2,j)}}{Best_j(t) + \epsilon}$,
      $P_{(i,j)} = \alpha_1 \times randn \times \left(1 - (\frac{t}{T})^2\right) + \frac{x_{(i,j)} - M_{(x_i)}}{Best_j(t) \times (UB_(j) - LB_(j)) + \epsilon}$
      if $t \le \frac{T}{4}$ **then**
        $x_{(i,j)}(t+1) = Best_j(t) \times -\eta_{(i,j)}(t) \times \beta_1 \times randn \times \left(1 - (\frac{t}{T})^2\right) - R_{(i,j)}(t) \times randn$, ▷ {**High walking**}
        $x.UB_{(i,j)}(t+1) = x_{(i,j)}(t+1) > UB$
        $x.LB_{(i,j)}(t+1) = x_{(i,j)}(t+1) < LB$
        $x_{(i,j)}(t+1) = x_{(i,j)}(t+1) \times (x.UB + x.LB) + LB \times x.LB + UB \times x.UB$
      else if $t \le 2\frac{T}{4}$ *and* $t > \frac{T}{4}$ **then**
        $x_{(i,j)}(t+1) = Best_j(t) \times x_{(r_1,j)} \times DES(t) \times randn$, ▷ {**Belly walking**}
        $x.UB_{(i,j)}(t+1) = x_{(i,j)}(t+1) > UB$
        $x.LB_{(i,j)}(t+1) = x_{(i,j)}(t+1) < LB$
        $x_{(i,j)}(t+1) = x_{(i,j)}(t+1) \times (x.UB + x.LB) + LB \times x.LB + UB \times x.UB$
      else if $t \le 3\frac{T}{4}$ *and* $t > 2\frac{T}{4}$ **then**
        $x_{(i,j)}(t+1) = Best_j(t) \times P_{(i,j)}(t) \times randn$, ▷ {**Hunting coordination**}
        $x.UB_{(i,j)}(t+1) = x_{(i,j)}(t+1) > UB$
        $x.LB_{(i,j)}(t+1) = x_{(i,j)}(t+1) < LB$
        $x_{(i,j)}(t+1) = x_{(i,j)}(t+1) \times (x.UB + x.LB) + LB \times x.LB + UB \times x.UB$
      else
        $x_{(i,j)}(t+1) = Best_j(t) - \eta_{(i,j)}(t) \times \epsilon - R_{(i,j)}(t) \times randn$, ▷ {**Hunting cooperation**}
        $x.UB_{(i,j)}(t+1) = x_{(i,j)}(t+1) > UB$
        $x.LB_{(i,j)}(t+1) = x_{(i,j)}(t+1) < LB$
        $x_{(i,j)}(t+1) = x_{(i,j)}(t+1) \times (x.UB + x.LB) + LB \times x.LB + UB \times x.UB$
      end if
    end for
  end for
  $t = t + 1$,
end while
Return the best individual found during the evolution $Best(X)$.

3. Numerical and experimental evaluation

To validate the effectiveness of the proposed approach, we conducted verification on both numerical and experimental data in the subsequent sections. By performing these verification steps, we aimed to assess the accuracy and reliability of the proposed approach in practical scenarios. This verification process involved analyzing and evaluating the results obtained from applying the proposed approach to the numerical data as well as the data collected through real-world experiments. The results show the performance and suitability of the proposed approach for the different applications.

The damage detection algorithm was implemented using MATLAB 2023a, a programming environment specifically suited for numerical computations and data analysis. The developed computer program utilizes various libraries in MATLAB including Machine learning, econometrics and optimization toolboxes.

3.1. Numerical verification

This section validates our proposed method using numerical examples of composite laminate plates. In the following, we employ the Gaussian smoothing approach to smooth the FRF input signals, and subsequently, we apply Johanson cointegration for data fusion. Finally, we construct the proposed objective function and solve it by using the proposed IRSA. Fig. 5 illustrates the flowchart of the proposed methodology for the numerical problem.

Table 3
Different damage scenarios of the composite laminate plates.

Case 1		Case 2		Case 3		Case 4	
Element	Ratio	Element	Ratio	Element	Ratio	Element	Ratio
1	0.20	5	0.15	4	0.15	3	0.20
10	0.15	10	0.10	8	0.20	7	0.15
13	0.20	20	0.25	23	0.15	19	0.30
17	0.30	25	0.30	31	0.10	23	0.35
29	0.25	30	0.10	36	0.20	31	0.20

3.1.1. Laminated composite model

In this paper, we use Reddy's laminated composite plate model [44] for the numerical validation. This model is a square laminated composite plate with fully supported edges. Different numbers of layers (NoL) and layering angles (LA) are considered in two models of the plate as follows:

- NoL = 3 and LA = $0°/90°/0°$,
- NoL = 6 and LA = $(0°/45°/0°) \times 2$.

The model's geometrical and finite element (FE) configurations are given below:

- The plates have a dimension of $100 \times 100 \times 10$ cm with a thickness of 10 cm, regardless of the number of layers.
- The plates are composed of $n_x \times n_y$ square elements resulting in a total of $(n_x + 1) \times (n_y + 1)$ nodes (see Fig. 6a), where n_x and n_y indicate the number of divisions on the x and y axes (see Fig. 6b).
- The plates consist of 36 shell elements with a total of 245 DoFs ($n_x = n_y = 6$). Thus, there are 49 nodes in total, 25 of which are active. Three translational DOFs exist in each node (w_x, w_y, w_z), and two rotational DOFs (φ_x, φ_y). We assume that the plate has a rigid DoF for in-plane rotation (φ_z).
- Due to the fixed support on four sides of the plates, there are 125 active DoFs.

As mentioned before, MATLAB is utilized to simulate all FE models of the composite laminate plates, as well as to program the damage detection algorithm. In this study, we use the first-order shear deformation theory (FSDT)–an extension of Classical Laminated Plate Theory (CLPT) [44]. To reduce the number of measured locations, we employ the condensed form of FRFs (CFRFs), as discussed in [38]. In the following, the results of the newly proposed method are referred to as CICFRF.

The material properties for the composite consist of Young's Modulus (E), Poisson ratio (ν), and Modulus of Rigidity (G). Specifically, E_1 and E_2 represent Young's Modulus with values of 40 and 1 N/m^2 respectively. The Poisson ratios, ν_{12} and ν_{21}, are 0.25 and 0.00625. For the Modulus of Rigidity, G_{12}, G_{13}, and G_{23} are calculated as $0.6E_2$, $0.6E_2$, and $0.5E_2$ respectively [44]. The same plate models have also been investigated by other researchers including [45–50].

This study investigates four damage scenarios considering different damage locations, severity, and types as listed in Table 3. The first ten natural frequencies of the different damage scenarios are presented in Table 4. It can be observed that the natural frequencies of the plates decrease as the damage occurs. In addition, it is evident that the frequencies are closely spaced. The authors have extensively studied this property of laminated composite plates in their previous work [38,51].

To determine the optimal excitation locations for the plates, Eq. (7) is applied. According to Table 5, signals are obtained by varying composite plate models (NoL = 3 and 6) and optimal excitation locations. As indicated in Table 5, the first eight DOFs that correspond to the largest entries in the obtained vector Λ represent the optimal locations for excitation of each plate model. All DOFs associated with out-of-plane translational DOFs (i.e., those along the z-axis in Fig. 6a) are assumed to be measured at the measurement locations.

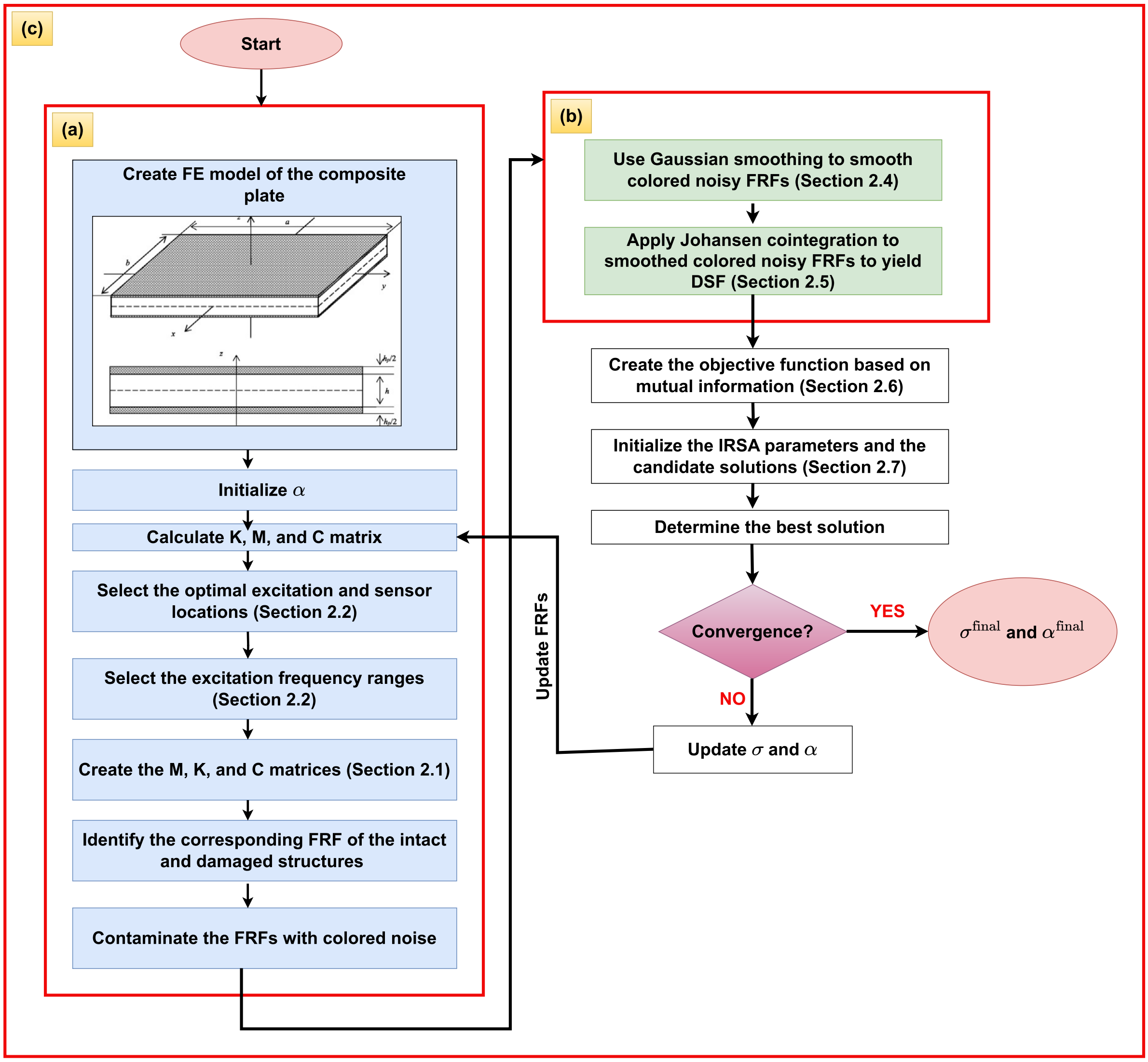

Fig. 5. Methodology steps of the proposed method on a numerical example ((a) Performing FE modeling simulations. (b) applying data analytics methods on CFRP, and (c) implementing the proposed model updating method.)

After identifying the DOFs that correspond to the optimal excitation and measurement locations (see Section 2.2), the FRFs of the plates are obtained following the procedure in Section 2.1. Subsequently, the synthesized FRFs are contaminated with brown noise, a type of nonstationary colored noise based on the steps in Section 2.3. In this section, our analysis focuses solely on FRFs contaminated with brown noise because it is known to be the most correlated type of colored noise. However, it is expected that similar results would be obtained with other types of noise.

The KPSS test is then applied to determine the presence of unit roots in FRFs polluted with brown noise. It is imperative to carefully decide the number of lags in the KPSS test to avoid losing the power of the test (large lags) or obtaining biased results (short lag). To this end, the following equation is employed to obtain the maximum lag for the test:

$$L_{\max} = \left[12 \times \left(\frac{N}{100} \right)^{\frac{1}{4}} \right] \tag{27}$$

where $L_{\max}$ is the maximum lag length, N is the number of excitation frequencies, and [.] indicate the integer part of a number.

For Johansen cointegration to operate, the concatenated chunks of FRFs obtained at different locations must be of the same order of nonstationarity–a requirement for fusing FRFs obtained at different locations. However, Cross and Worden [21] suggested that checking this requirement can be overlooked when employing Johansen cointegration in SHM. Having said that, we still conform to this requirement of the Johansen cointegration by checking the order of nonstationarity in FRFs contaminated with brown noise. Tables 6, 7, 8, and 9 present the results of the KPSS test conducted on FRF signals contaminated with brown noise of SNR = 10 and 20. As shown in the tables, h can either take a value of 1 or 0, indicating whether the signal trend is nonstationary or stationary. According to Eq. (27), the maximum lag of the signals is 18 because they are 601 in length. To verify the validity of the tests, three different lags are considered: 16, 17, and 18. A significance level of 0.1 is used for the test. Therefore, any P-value less than 0.1 defies the null hypothesis of signal stationarity. In Tables 6 to 9, it is shown that for all DOFs, the P-values are less than 0.05, except for DOF 56 (Table 8) and DOF 66 (Table 9), which have slightly larger P-values. Setting the significance level to 0.05 implies that the signals would be considered stationary. Nonetheless, as suggested by [21], Johansen cointegration can still be applied in the context of SHM despite signals not meeting the same nonstationary assumption. However, the results displayed in the table indicate that the FRF signals for all DOFs

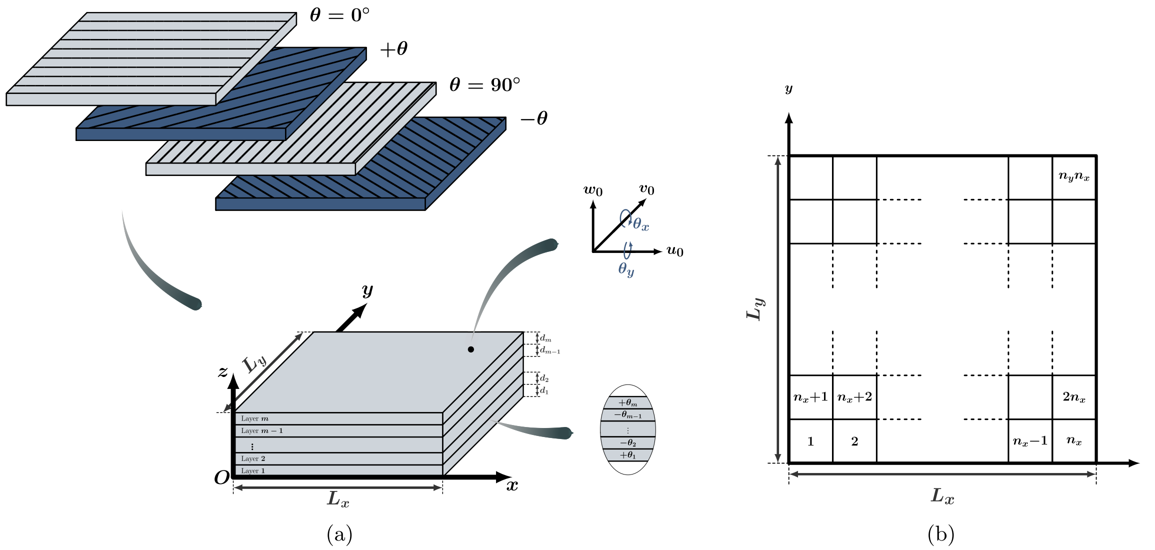

Fig. 6. (a) Sketch of the composite laminate plate, and (b) element numbering of the composite laminate plate ($n_x = n_y = 6$).

Table 4
First ten natural frequencies of the composite laminate plates with different NoL and LA.

Lamination scheme		Mode No. 1	2	3	4	5	6	7	8	9	10
Intact	NoL = 3, LA = (0°/90°/0°)	7.40	11.14	14.32	16.23	18.74	21.42	23.32	23.90	25.74	26.29
	NoL = 6, LA = (0°/45°/0°/0°/45°/0°)	7.64	11.53	14.74	16.82	19.07	21.99	23.78	24.90	25.78	26.60
Case 1	NoL = 3, LA = (0°/90°/0°)	7.25	10.98	14.06	16.01	18.51	21.06	22.78	23.50	25.29	25.83
	NoL = 6, LA = (0°/45°/0°/0°/45°/0°)	7.47	11.35	14.47	16.61	18.81	21.59	23.29	24.45	25.36	26.03
Case 2	NoL = 3, LA = (0°/90°/0°)	7.29	10.97	14.13	15.88	18.55	21.05	22.89	23.54	25.38	25.92
	NoL = 6, LA = (0°/45°/0°/0°/45°/0°)	7.54	11.36	14.57	16.44	18.94	21.53	23.40	24.56	25.44	26.34
Case 3	NoL = 3, LA = (0°/90°/0°)	7.34	11.03	14.27	16.10	18.53	21.16	23.16	23.66	25.47	25.94
	NoL = 6, LA = (0°/45°/0°/0°/45°/0°)	7.57	11.40	14.66	16.67	18.85	21.74	23.61	24.59	25.54	26.24
Case 4	NoL = 3, LA = (0°/90°/0°)	7.18	10.96	13.96	15.96	18.46	21.01	22.68	23.57	25.14	25.84
	NoL = 6, LA = (0°/45°/0°/0°/45°/0°)	7.43	11.31	14.41	16.54	18.71	21.68	23.20	24.43	25.24	26.02

Table 5
The optimal excitation locations obtained for the laminated composite plates.

Plate	Λ	DOFs
NoL = 3, LA = (0°/90°/0°)	25.2310, 23.6311, 22.5224, 20.1986, 17.2411, 17.2200, 17.0378, 16.2453	71, 66, 56, 31, 102, 47, 72, 32
NoL = 6, LA = (0°/45°/0°) × 2	34.07, 33.74, 33.2212, 32.0823, 27.2546, 25.6578, 22.5345, 18.2422	21, 66, 31, 41, 107, 117, 122, 51

Table 6
Results of the KPSS test run on each column of the FRF matrix contaminated with brown noise. The significance level of the test is 0.1 with SNR = 10; NoL = 3 and LA = 0°/90°/0°.

FRF	Lag	P-value	h	Stationary
1^{st} excitation				
DOF_{71}	16, 17, 18	0.0315, 0.0365, 0.0420	1, 1, 1	No
Δ DOF_{71}	16, 17, 18	0.1000, 0.1000, 0.1000	0, 0, 0	Yes
2^{nd} excitation				
DOF_{66}	16, 17, 18	0.0444, 0.0434, 0.0476	1, 1, 1	No
Δ DOF_{66}	16, 17, 18	0.1000, 0.1000, 0.1000	0, 0, 0	Yes
3^{rd} excitation				
DOF_{56}	16, 17, 18	0.0132, 0.0134, 0.0165	1, 1, 1	No
Δ DOF_{56}	16, 17, 18	0.1000, 0.1000, 0.1000	0, 0, 0	Yes
4^{th} excitation				
DOF_{31}	16, 17, 18	0.0100, 0.0100, 0.0100	1, 1, 1	No
Δ DOF_{31}	16, 17, 18	0.1000, 0.1000, 0.1000	0, 0, 0	Yes
5^{st} excitation				
DOF_{102}	16, 17, 18	0.0100, 0.0100, 0.0114	1, 1, 1	No
Δ DOF_{102}	16, 17, 18	0.1000, 0.1000, 0.1000	0, 0, 0	Yes
6^{nd} excitation				
DOF_{47}	16, 17, 18	0.0156, 0.0203, 0.0249	1, 1, 1	No
Δ DOF_{47}	16, 17, 18	0.1000, 0.1000, 0.1000	0, 0, 0	Yes
7^{rd} excitation				
DOF_{72}	16, 17, 18	0.0100, 0.0100, 0.0100	1, 1, 1	No
Δ DOF_{72}	16, 17, 18	0.1000, 0.1000, 0.1000	0, 0, 0	Yes
8^{th} excitation				
DOF_{32}	16, 17, 18	0.0326, 0.0375, 0.0400	1, 1, 1	No
Δ DOF_{32}	16, 17, 18	0.1000, 0.1000, 0.1000	0, 0, 0	Yes

are indeed non-stationary. When the difference operator Δ is applied, P-values of 0.1 indicate stationary results. Therefore, Johansen cointegration can be applied to all $I(1)$ signals.

3.1.2. Gaussian smoothing applied to input signals

Fig. 7 presents FRFs of the composite laminated plate contaminated with different types of noise. It can be observed that brown noise has the most pronounced impact introducing severe outliers to the signals. In our numerical analysis, we deliberately utilized signals that are contaminated with brown noise to demonstrate the capability of our method.

As demonstrated in Eq. (18), the value of σ for the Gaussian smoothing algorithm is optimized in the optimization process. To this end, a grid of possible values between 0.5 and 3, representing fine smoothing and coarse smoothing, respectively, with an increment equal to 0.01, was set to be tested in the optimization process. As a result, the best smoothing factor (see Table 10) was selected as the optimal value for the problem of damage detection in composite plates.

Fig. 8 shows the original noisy signals and the smoothed version of the contaminated signals.

3.1.3. Results of Johansen cointegration

An alternative method for combining the columns of the CFRF matrix is to concatenate them into a vector. In this case, we refer to the resulting shorter vector obtained from Johansen cointegration as CICFRF and the vector obtained by simply concatenating the columns of CFRF as CFRF. Both damage features, i.e., CICFRF and CFRF, are used in the proposed objective function (18) to compare the effectiveness of Johansen cointegration in fusing the CFRF signals.

Figs. 9 and 10 illustrate the damage detection outcomes using CFRF and the proposed CICFRF, respectively. Here, the results of the case contaminated with the more severe noise, i.e., SNR = 10, are presented for illustration. It is evident from the results that incorporating the CICFRF in the objective function results in superior results.

Table 7
Results of the KPSS test run on each column of the FRF matrix contaminated with brown noise. The significance level for the test is 0.1 and SNR = 10; NoL = 6 and LA = (0°/45°/0°) × 2.

FRF	Lag	P-value	h	Stationary
1^{st} excitation				
DOF_{21}	16, 17, 18	0.0200, 0.0203, 0.0216	1, 1, 1	No
Δ DOF_{21}	16, 17, 18	0.1000, 0.1000, 0.1000	0, 0, 0	Yes
2^{nd} excitation				
DOF_{66}	16, 17, 18	0.0156, 0.0182, 0.0202	1, 1, 1	No
Δ DOF_{66}	16, 17, 18	0.1000, 0.1000, 0.1000	0, 0, 0	Yes
3^{rd} excitation				
DOF_{31}	16, 17, 18	0.0100, 0.0100, 0.0100	1, 1, 1	No
Δ DOF_{31}	16,17, 18	0.1000, 0.1000, 0.1000	0, 0, 0	Yes
4^{th} excitation				
DOF_{41}	16, 17, 18	0.0100, 0.0100, 0.0102	1, 1, 1	No
Δ DOF_{41}	16, 17, 18	0.1000, 0.1000, 0.1000	0, 0, 0	Yes
5^{st} excitation				
DOF_{107}	16, 17, 18	0.0186, 0.0201, 0.0237	1, 1, 1	No
Δ DOF_{107}	16, 17, 18	0.1000, 0.1000, 0.1000	0, 0, 0	Yes
6^{nd} excitation				
DOF_{117}	16, 17, 18	0.0100, 0.0100, 0.0100	1, 1, 1	No
Δ DOF_{117}	16, 17, 18	0.1000, 0.1000, 0.1000	0, 0, 0	Yes
7^{rd} excitation				
DOF_{122}	16, 17, 18	0.0100, 0.0100, 0.0100	1, 1, 1	No
Δ DOF_{122}	16, 17, 18	0.1000, 0.1000, 0.1000	0, 0, 0	Yes
8^{th} excitation				
DOF_{51}	16, 17, 18	0.0232, 0.0222, 0.0245	1, 1, 1	No
Δ DOF_{51}	16, 17, 18	0.1000, 0.1000, 0.1000	0, 0, 0	Yes

Table 8
Results of the KPSS test run on each column of the FRF matrix contaminated with brown noise. The significance level for the test is 0.1 and SNR = 20; NoL = 3 and LA = 0°/90°/0°.

FRF	Lag	P-value	h	Stationary
1^{st} excitation				
DOF_{71}	16, 17, 18	0.0100, 0.0100, 0.0100	1, 1, 1	No
Δ DOF_{71}	16, 17, 18	0.1000, 0.1000, 0.1000	0, 0, 0	Yes
2^{nd} excitation				
DOF_{66}	16, 17, 18	0.0286, 0.0311, 0.0340	1, 1, 1	No
Δ DOF_{66}	16, 17, 18	0.1000, 0.1000, 0.1000	0, 0, 0	Yes
3^{rd} excitation				
DOF_{56}	16, 17, 18	0.0645, 0.0682, 0.0799	1, 1, 1	No
Δ DOF_{56}	16, 17, 18	0.1000, 0.1000, 0.1000	0, 0, 0	Yes
4^{th} excitation				
DOF_{31}	16, 17, 18	0.0100, 0.0100, 0.0100	1, 1, 1	No
Δ DOF_{31}	16, 17, 18	0.1000, 0.1000, 0.1000	0, 0, 0	Yes
5^{st} excitation				
DOF_{102}	16, 17, 18	0.0100, 0.0100, 0.0113	1, 1, 1	No
Δ DOF_{102}	16, 17, 18	0.1000, 0.1000, 0.1000	0, 0, 0	Yes
6^{nd} excitation				
DOF_{47}	16, 17, 18	0.0100, 0.0100, 0.0100	1, 1, 1	No
Δ DOF_{47}	16, 17, 18	0.1000, 0.1000, 0.1000	0, 0, 0	Yes
7^{rd} excitation				
DOF_{72}	16, 17, 18	0.0100, 0.0100, 0.0100	1, 1, 1	No
Δ DOF_{72}	16, 17, 18	0.1000, 0.1000, 0.1000	0, 0, 0	Yes
8^{th} excitation				
DOF_{32}	16, 17, 18	0.0346, 0.0450, 0.0302	1, 1, 1	No
Δ DOF_{32}	16, 17, 18	0.1000, 0.1000, 0.1000	0, 0, 0	Yes

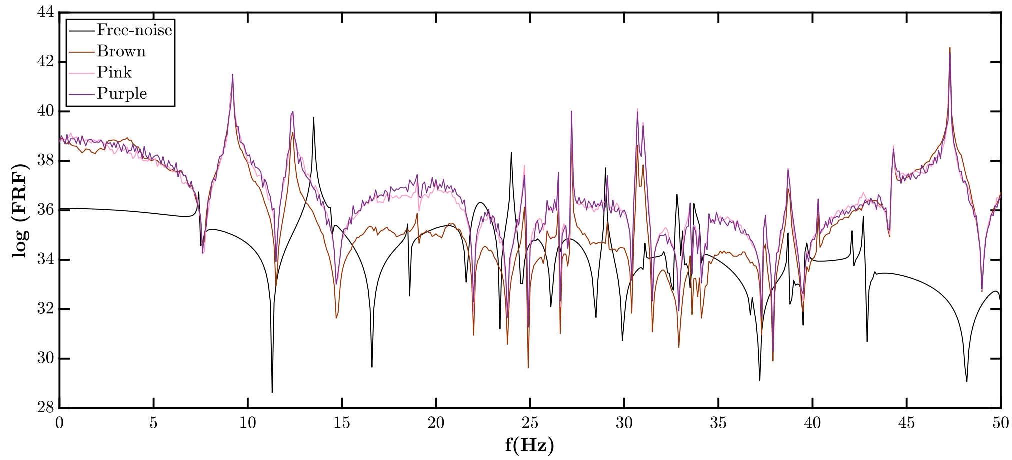

Fig. 7. Examples of noise-free and noise-polluted CFRFs contaminated with different types of colored noise (brown, pink, and purple) with SNR = 10. The data is obtained from a plate model with NoL = 3, LA = (0°/90°/0°) excited and measured at DOF numbers 66 and 32, respectively.

Table 9
Results of the KPSS test run on each column of the FRF matrix contaminated with brown noise. The significance level for the test is 0.1 and SNR = 20; NoL = 6 and LA = (0°/45°/0°) × 2.

FRF	Lag	P-value	h	Stationary
1^{st} excitation				
DOF_{21}	16, 17, 18	0.0100, 0.0100, 0.0100	1, 1, 1	No
Δ DOF_{21}	16, 17, 18	0.1000, 0.1000, 0.1000	0, 0, 0	Yes
2^{nd} excitation				
DOF_{66}	16, 17, 18	0.0501, 0.0610, 0.0660	1, 1, 1	No
Δ DOF_{66}	16, 17, 18	0.1000, 0.1000, 0.1000	0, 0, 0	Yes
3^{rd} excitation				
DOF_{31}	16, 17, 18	0.0100, 0.0100, 0.0100	1, 1, 1	No
Δ DOF_{31}	16,17, 18	0.1000, 0.1000, 0.1000	0, 0, 0	Yes
4^{th} excitation				
DOF_{41}	16, 17, 18	0.0110, 0.0100, 0.0133	1, 1, 1	No
Δ DOF_{41}	16, 17, 18	0.1000, 0.1000, 0.1000	0, 0, 0	Yes
5^{st} excitation				
DOF_{107}	16, 17, 18	0.0290, 0.0310, 0.0321	1, 1, 1	No
Δ DOF_{107}	16, 17, 18	0.1000, 0.1000, 0.1000	0, 0, 0	Yes
6^{nd} excitation				
DOF_{117}	16, 17, 18	0.0100, 0.0100, 0.0100	1, 1, 1	No
Δ DOF_{117}	16, 17, 18	0.1000, 0.1000, 0.1000	0, 0, 0	Yes
7^{rd} excitation				
DOF_{122}	16, 17, 18	0.0100, 0.0100, 0.0100	1, 1, 1	No
Δ DOF_{122}	16, 17, 18	0.1000, 0.1000, 0.1000	0, 0, 0	Yes
8^{th} excitation				
DOF_{51}	16, 17, 18	0.0310, 0.0328, 0.0322	1, 1, 1	No
Δ DOF_{51}	16, 17, 18	0.1000, 0.1000, 0.1000	0, 0, 0	Yes

Table 10
The value of σ for all cases as determined by optimization in composite plates.

	σ			
Lamination scheme	Case 1	Case 2	Case 3	Case 4
Three-layer (0°/90°/0°)	1.05	1.10	1.03	1.12
Six-layer (0°/45°/0°)	1.27	1.10	1.04	1.11

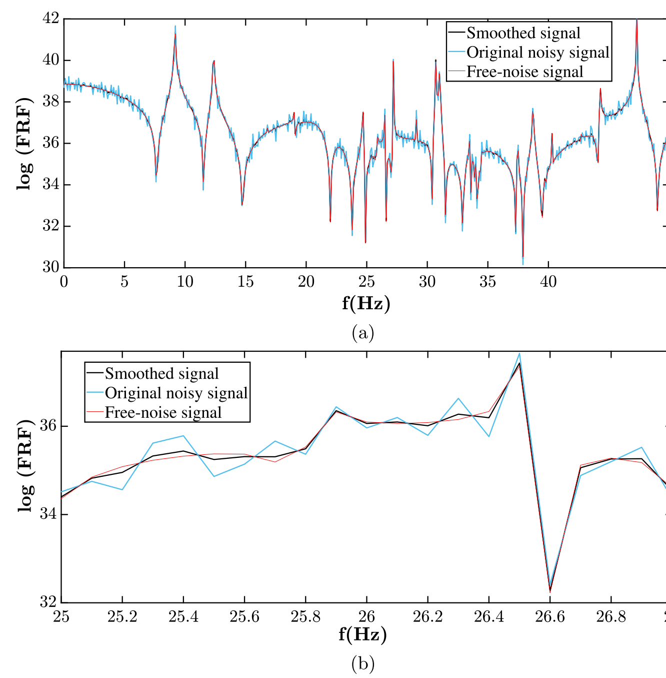

Fig. 8. Difference between the noise-free, original noise-polluted, and smoothed FRF signals of a composite laminated plate with white noise with SNR = 10; NoL = 3, LA = (0°/90°/0°); (a) whole spectrum and (b) zoomed spectrum.

To further examine the damage identification results, Table 11 presents the accuracy indices CI, MSE, and RE obtained for the various laminated composite models using CFRF and CICFRF signals. A predicted outcome is more accurate when |CI|, |MSE|, and |RE| are close to 1, 0, and 0, respectively. The accuracy indices further showcase the superiority of the proposed method using CICFRF. Furthermore, the results obtained by using CFRF indicate significant errors in the location and severity prediction of the damage.

Figs. 11 and 12 demonstrate the convergence of the proposed method using the proposed IRSA. It is evident from the figures that even with a relatively small number of iterations, the robust proposed IRSA algorithm is capable of achieving convergence in the proposed optimization process.

In optimization algorithms, central processing unit (CPU) time refers to the amount of time it takes for the algorithm to execute and find an

Table 11
Summary of the obtained error indices using the proposed damage detection method for all damage cases in the studied composite laminate plates with different SNR.

Case	Applied	SNR	NoL = 3, LA = (0°/90°/0°)			NoL = 6, LA = (0°/45°/0°) × 2		
No.	method		MSE	RE	CI	MSE	RE	CI
1	CFRF	10	0.0806	-0.9277	-0.2080	0.0907	-1.1536	-0.3164
1	CFRF	20	0.0777	-0.8855	-0.2727	0.0824	-1.0677	-0.3388
1	CICFRF	10	0.00390	-0.1204	0.9460	0.0045	-0.1302	0.9661
1	CICFRF	20	0.0040	-0.1005	0.9477	0.0040	-0.1256	0.9302
2	CFRF	10	0.0708	-0.9506	-0.4988	0.0669	-1.5038	-0.3324
2	CFRF	20	0.0727	-0.8788	-0.5988	0.0678	-0.5545	-0.2565
2	CICFRF	10	0.0040	-0.1188	0.9678	0.0040	-0.0964	0.9758
2	CICFRF	20	0.0039	-0.1027	0.9756	0.0030	-0.0999	0.9769
3	CFRF	10	0.0651	-0.6778	-0.3884	0.0666	-0.6099	-0.3245
3	CFRF	20	0.0656	-0.6978	-0.4199	0.0687	-0.8735	-0.3599
3	CICFRF	10	0.0040	-0.1308	0.9566	0.0056	-0.1644	0.9663
3	CICFRF	20	0.0040	-0.1156	0.9893	0.0044	-0.1561	0.9597
4	CFRF	10	0.0545	-0.5855	-0.3555	0.0933	-0.6065	-0.3798
4	CFRF	20	0.0625	-0.4954	-0.3035	0.0787	-0.6098	-0.3865
4	CICFRF	10	0.0046	-0.1154	0.9763	0.0049	-0.1381	0.9773
4	CICFRF	20	0.0044	-0.1100	0.9720	0.0054	-0.1266	0.9778

Table 12
Comparison of CPU time for different composite plates and damage scenarios.

	Time (Sec.)			
Lamination scheme	Case 1	Case 2	Case 3	Case 4
Three-layer (0°/90°/0°)	96	100	90	91
Six-layer (0°/45°/0°)	96	100	95	98

optimal solution using a computer's CPU. CPU time is an important metric for evaluating the efficiency and performance of an optimization algorithm. In Table 12, the CPU time is shown for all the investigated damage scenarios. The table provides a comprehensive overview of the computational demands of each composite model, allowing for a better understanding of the time required for optimization. The table demonstrates that our proposed method achieves accurate and efficient detection of damage quantity in complex structures. The CPU time required for this task is notably low, indicating that our method can accurately assess the extent of damage in a time-effective manner. This combination of accuracy and efficiency makes our method highly suitable for practical applications where prompt decision-making is crucial for ensuring structural integrity and maintenance.

Recognizing the significance of addressing outliers in SHM systems, we conducted an in-depth analysis of the impact of noise on our proposed method. In the study, additional artificial noise was added to the composite dataset to observe how effectively our method copes with increasing noise complexities. Specifically, the FRFs of the composite three-layer scenario were contaminated with additional noise of SNR 5 and SNR 0. Subsequently, our proposed approach was applied to detect damage for scenario 1. The obtained MSE for SNR 5 was 0.1465, reflecting a notable increase compared to the SNR 10 results (0.00390), with an increase of 0.1426 in MSE. Further evaluation at SNR 0 revealed a significant increase, with MSE reaching 0.1798. This analysis provides valuable insights into our method's performance under different noise levels. In contrast to other approaches, which exhibit notable weaknesses in handling outliers, our proposed method demonstrates superior performance even in small SNRs, including SNR 0. However, it is crucial to note that the optimum and most reliable SNR for our approach, ensuring precise predictions with minimal error, is identified as SNR 10.

3.1.4. Importance of mutual information

In accordance with Section 2.6, we consider the mutual information between processed measured and simulated signals. Here, we compare the accuracy of the proposed objective function with an alternative that replaces the mutual information with the Euclidean norm. Table 14 provides insights into the CPU time required to execute the optimization algorithm on these objective functions. The results demonstrate that the proposed objective function yields higher accuracy and requires less processing time. The longer execution time of the algorithm can be attributed to the less smooth objective function that makes the algorithm trap in local minima. Further, we investigate this hypothesis in more detail.

The landscape of an objective function refers to the topography or structure of the function being optimized. It represents how the objective function's value changes as the decision variables are varied. Visualizing the landscape of an objective function can provide insights into the complexity, presence of multiple optima, and the search space's characteristics. Since we have more than one variable (damage indices), we have chosen different pairs of variables to plot on the two axes. This will allow us to visualize the relationship between different variables and how they affect the objective function. Fig. 13 shows the landscape of the two objective functions. The figure clearly shows that the proposed objective function with NMI is smoother than the one defined based on the Euclidean norm. This will expedite the convergence speed of the algorithm, allowing it to reach a solution more quickly.

The error indices obtained from 50 runs of the algorithm, each with different randomly generated noise, are presented in Table 13. These results further confirm the superior accuracy of the proposed method using the novel objective function. The significantly less accurate results obtained from the Euclidean norm-based objective function can be attributed to the rough landscape of the search space. This feature makes the algorithm trap in a local minimum and not converge to the exact solution.

3.1.5. Comparing the results of using different CI residuals

More than one cointegration vector can be obtained for the signals introduced to the Johansen cointegration process. The vector of coefficients in Eq. (14) corresponds to the cointegration vectors obtained from the eigenvalue problem of the Johansen cointegration procedure. It is known that the eigenvector corresponding to the first eigenvalue of the Johansen characteristic function results in the most stationary residual. As such, higher-order cointegration vectors can induce less stationary properties into the fused signals. To demonstrate the strength of the proposed algorithm, we also analyze the second cointegration resid-

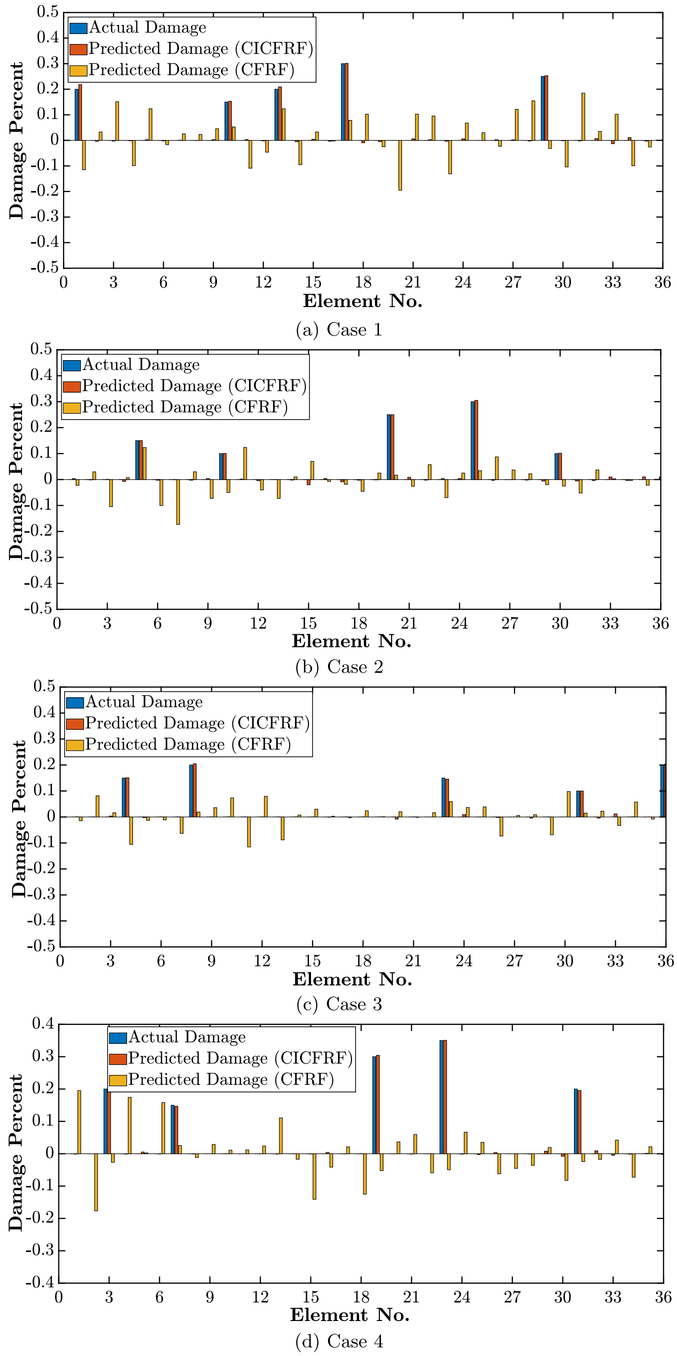

(a) Case 1

(b) Case 2

(c) Case 3

(d) Case 4

Fig. 9. The computed damage indices obtained of CICFRF; brown noise, SNR = 10; NoL = 3, LA = (0°/90°/0°).

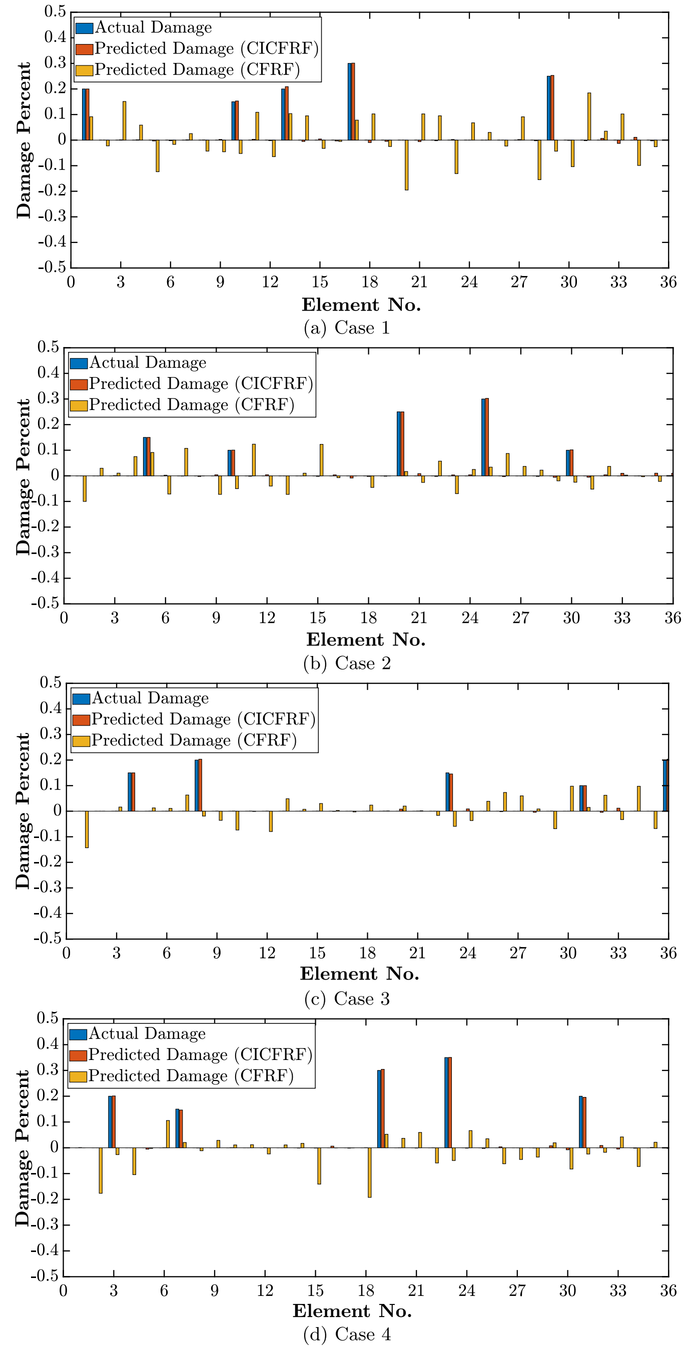

(a) Case 1

(b) Case 2

(c) Case 3

(d) Case 4

Fig. 10. The computed damage indices obtained of CICFRF; brown noise, SNR = 10; NoL = 6, LA = (0°/45°/0°).

ual of the CFRF matrix, termed CICFRF_2, to solve the damage detection problem. The CICFRF_1 and CICFRF_2 vectors calculated from Eq. (14) are shown in Fig. 14. The accuracy indices obtained from both CICFRF_1 and CICFRF_2 are presented in Table 15. It is evident that the proposed algorithm achieves superior results when using CICFRF_1 compared to CICFRF_2. Consequently, it can be concluded that the improved performance of CICFRF_1 is due to its enhanced stationary properties.

3.1.6. *Comparative analysis of composite plates with different E_1/E_2 ratios*

To evaluate the effectiveness of the proposed method, several parameters of the plate models have been examined in the sections above. These parameters include the number and orientation of the ply. However, it is necessary to also explore the proposed method's capability to detect damage in plates with different E_1/E_2 ratios. So far, all plate models had an E_1/E_2 ratio of 40. Thus, in this section, we extend our investigation to also include smaller values of E_1/E_2, namely 20 and 30. In Table 16, the natural frequencies for different E_1/E_2 values of the plate models are shown. As can be seen from the table, smaller E_1/E_2 ratios result in smaller natural frequencies. Table 18 shows the value of σ for all cases as determined by optimization with different values of the E_1/E_2 ratio. The accuracy indices for each case of three different damage scenarios are listed in Table 17. It is evident that for all examined E_1/E_2 ratios, accuracy indices are very similar. This confirms the robustness of the proposed method to different values of the E_1/E_2 ratio.

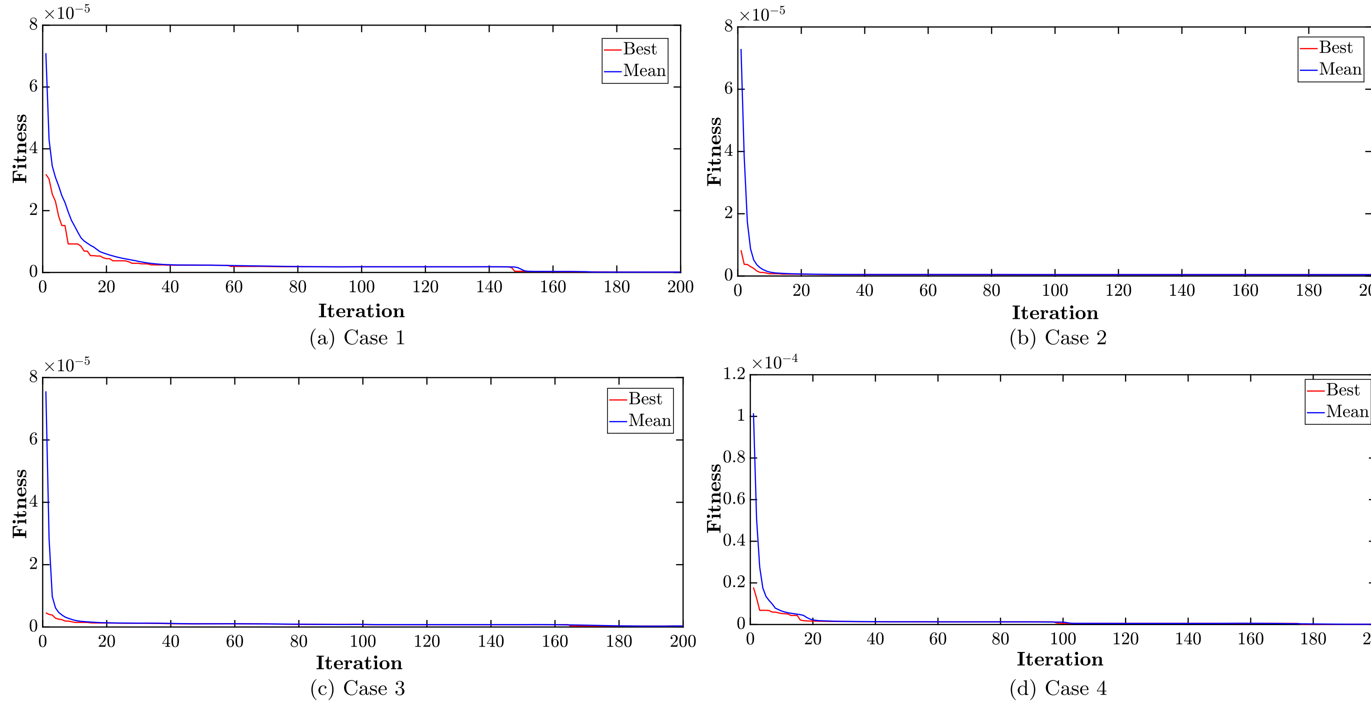

Fig. 11. Convergence of the proposed IRSA for damage scenarios 1-4 in three-layer (0°/90°/0°) composite laminate plate (brown noise with SNR = 10).

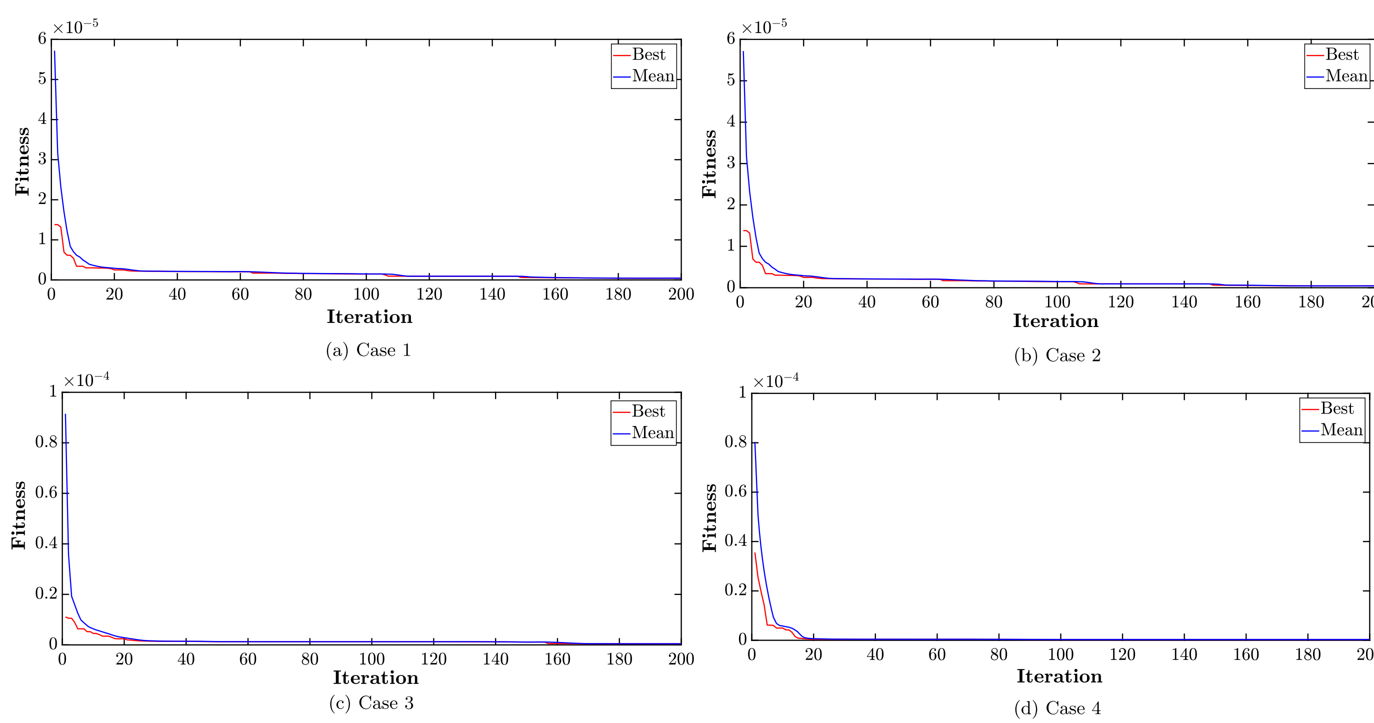

Fig. 12. Convergence of the proposed IRSA for damage scenarios 1-4 in six-layer (0°/45°/0°) composite laminate plate (brown noise with SNR = 10).

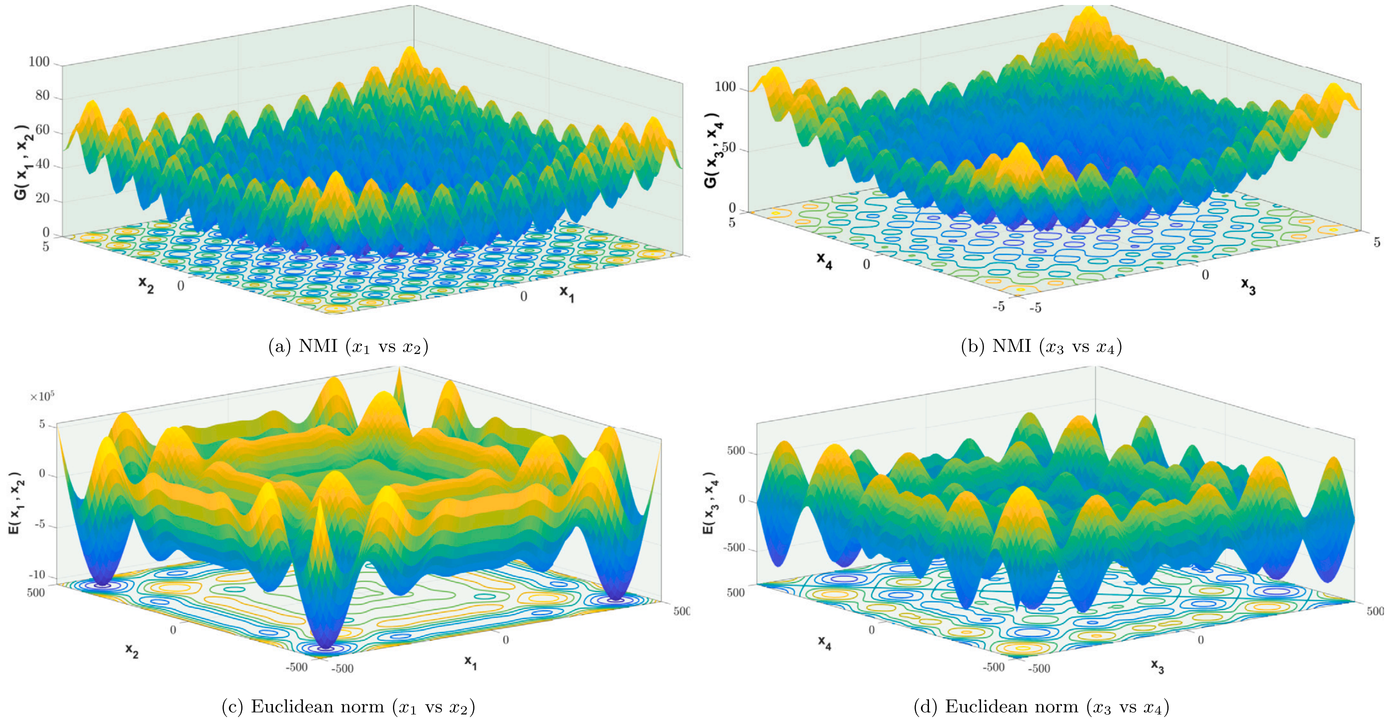

(a) NMI (x_1 vs x_2) (b) NMI (x_3 vs x_4)

(c) Euclidean norm (x_1 vs x_2) (d) Euclidean norm (x_3 vs x_4)

Fig. 13. Landscape of our proposed objective function compared with an objective function based on the Euclidean norm. All variables are kept constant, except (a) x_1 and x_2 and (b) x_3 and x_4, are kept constant.

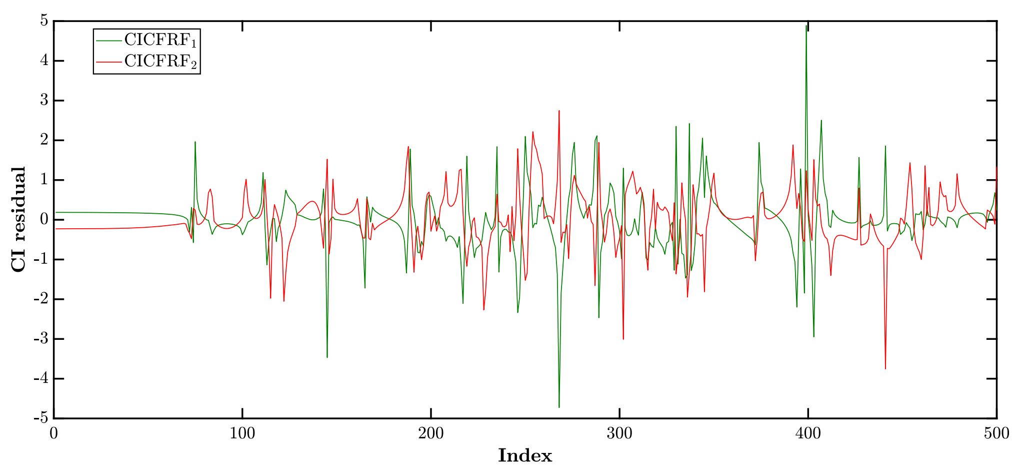

Fig. 14. Logarithmic plots of the PSD of CI_1 and CI_2, when the CFRF signals are contaminated with colored noise of SNR = 10 for a laminated plate with NoL = 3 and LA = (0°/90°/0°).

3.1.7. Comparative analysis of composite plates with different boundary conditions

The boundary conditions (BCs) can significantly impact the analysis and detection of damage in composite plates. Different types of BCs, such as simply supported, clamped, or free edges, can introduce variations in the structural response, including natural frequencies, mode shapes, and strain distribution. The identified changes serve as crucial indicators that must be taken into consideration when detecting the presence and determining the extent of damage in composite plates. These changes provide valuable insights and information that are instrumental in accurately assessing the damage in the plates. BCs affect how a structure responds to external forces and loads. They determine the constraints and limitations placed on the structure, which can alter its natural frequencies, mode shapes, and dynamic characteristics. Changes in boundary conditions can lead to variations in the structural response, affecting the accuracy of SHM measurements and analysis. Also, BCs can influence the localization of structural modes. Different boundary conditions can result in different mode shapes and mode frequencies. If the boundary conditions are altered, it can lead to a shift in the localization of modes, affecting the identification and interpretation of damage-induced changes in mode shapes or frequencies.

In order to test the capability of the proposed method in handling different BCs, here we investigate composite plates with varying BCs. The following four BCs are studied:

- Type I: West: Free, East: Free, South: Simply supported, North: Simply supported,
- Type II: West: Clamped, East: Clamped, South: Simply Supported, North: Simply supported,
- Type III: West: Free, East: Free, South: Clamped, North: Clamped, and

Table 13
Summary of the obtained error indices for the studied composite laminate plate for Euclidean norm and NMI (Three-layer (0°/90°/0°) and SNR = 10).

Euclidean norm			
Case	MSE	RE	CI
1	0.0876	-3.3098	-0.8003
2	0.0768	-4.4567	-0.6521
3	0.0823	-4.3498	-0.7763
4	0.0815	-6.3780	-0.9513
NMI			
Case	MSE	RE	CI
1	0.00390	-0.1204	0.9460
2	0.0040	-0.1188	0.9678
3	0.0040	-0.1308	0.9566
4	0.0046	-0.1154	0.9763

Table 14
Comparison of CPU time (Three-layer (0°/90°/0°) and SNR = 10).

Euclidean norm	
Case	Time (Sec.)
1	504
2	550
3	547
4	530
NMI	
Case	Time (Sec.)
1	96
2	100
3	90
4	91

- Type IV: West: Simply supported, East: Simply supported, South: Simply supported, North: Simply supported.

Fig. 15 illustrates the mode shapes corresponding to the first four frequencies of the plates with various BCs. It is evident that the frequencies and mode shapes of these plates are different due to their altered active degrees of freedom. Table 20 presents the damage detection results obtained for each BC scenario. The convergence of the objective function, achieved by optimizing the goal function with the proposed IRSA, is shown in Fig. 16. The presented figure demonstrates the convergence specifically for the first damage case. It is apparent from the figure that all types of BCs exhibit favorable convergence, indicating that our methods are not significantly influenced by the selection of BCs. Additionally, the remaining damage cases also exhibit satisfactory convergence, although corresponding plots were omitted from the paper to manage its length effectively. Through the systematic examination of these outcomes, the influence of BCs on the accuracy and reliability of our method was studied identifying the strengths and limitations of our technique under different boundary conditions. It was found that our method performed consistently well across various BCs, demonstrating its robustness and effectiveness in detecting damage in composite plates. It was further observed that the optimized value for σ (smoothing parameter) was insensitive to the type of BCs and was selected based on Table 19 in all cases. By recognizing the significance of BCs, we can ensure the applicability and generalizability of our technique to real-world scenarios where boundary conditions can vary significantly. These findings reinforce the validity of our method, further solidifying its practical utility in structural health monitoring and damage assessment.

3.1.8. Component exclusion analysis

The major components contributing to the enhancements of the proposed methodology are Johanson cointegration, Gaussian smoothing, and IRSA. To ascertain the distinct contributions of these components to the overall methodology, a systematic one-by-one exclusion study was conducted. This analysis was performed on the three-layer composite with damage scenario 1 and an SNR of 10. The MSE results from each exclusion analysis are outlined below (see Fig. 17):

- Johansen Cointegration Exclusion: First, the methodology's performance was assessed by deliberately excluding the Johansen cointegration component. The exclusion resulted in noteworthy changes in outputs, with an observed MSE of 0.0806. In comparison to the methodology incorporating Johansen cointegration (MSE of 0.00390), this represented a substantial increase (0.0767) in MSE, indicating a deviation from reliable results.
- Gaussian Smoothing Exclusion: Next, the impact of excluding Gaussian smoothing from the methodology was examined. The omission of Gaussian smoothing significantly disrupted the signal-to-noise ratio in the measured FRFs, leading to heightened noise levels and diminished data smoothing. The associated MSE of 0.0521, when compared to the methodology with Gaussian smoothing (MSE of 0.00390), demonstrated an increase (0.0482) in MSE, underscoring the adverse effect on result reliability.
- IRSA Exclusion: As last, the methodology's performance was scrutinized upon excluding the IRSA and subsequently optimizing with a standard RSA. The resulting MSE of 0.1104, in contrast to the methodology incorporating IRSA (MSE of 0.00390), showed a considerable increase (0.1065) in MSE. This elevation in MSE suggests a departure from reliable results when IRSA is excluded from the optimization process.

The results affirm the importance of each element within the proposed methodology, including Johansen cointegration, Gaussian smoothing, and IRSA. These components collectively contribute to enhancing the accuracy and reliability of the damage detection results.

3.1.9. Comparison with other techniques

A comparison of the proposed method with two other state-of-the-art techniques to assess laminated composite plates is presented in the following section. These methods were published by Vo-Duy et al. [45] and Fallah et al. [46]. Both methods have been published in recent years and are based on optimization algorithms in composite plates. In Vo-Duy et al. [45], first, a model strain energy-based method is used to identify the probable defective elements. By minimizing a mode shape error function, an improved differential evolution algorithm is used to quantify the extent of damage in the identified defective elements. In Fallah et al. [46], CMRVBI, a condensed modal residual vector-based indicator, is proposed for identifying defective elements. A salp swarm algorithm is then applied to minimize an objective function based on changes in structural modal flexibility to update damage indices corresponding to the identified defective elements.

All three methods were employed to analyze the data of the laminated composite plates with varying damage scenarios and the accuracy indices were obtained as shown in Table 21. The results clearly demonstrate the superiority of the proposed method over the other methods. In Figs. 18, the damage detection results are presented for composite laminate plates with NoL = 3 and LA = (0°/90°/0°). As illustrated in the figures, it is evident again that the proposed method outperforms the other methods. This superiority stems from various capabilities of the proposed method such as the effective objective function and optimization algorithm. The proposed methods of Vo-Duy et al. [45] and Fallah et al. [46] are unable to deal with outliers stemming from

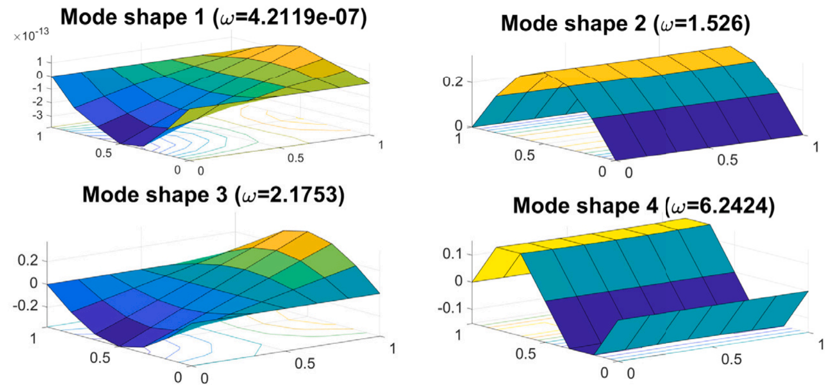

(a) Type I

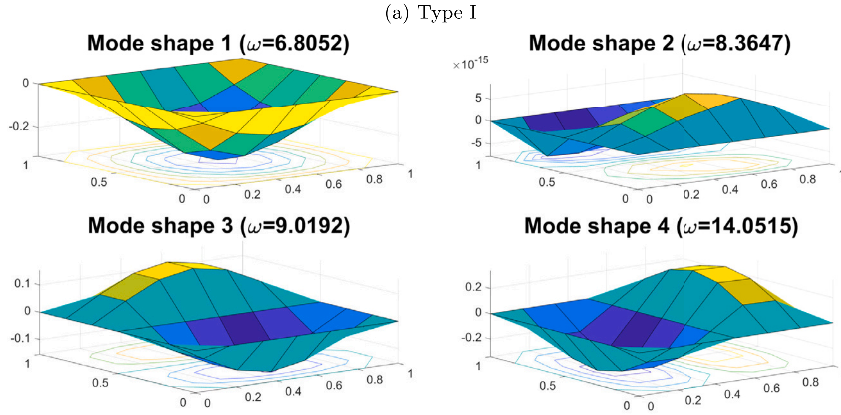

(b) Type II

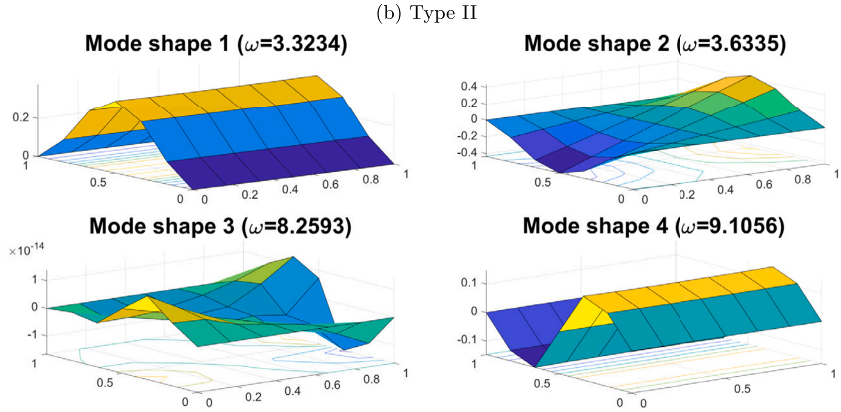

(c) Type III

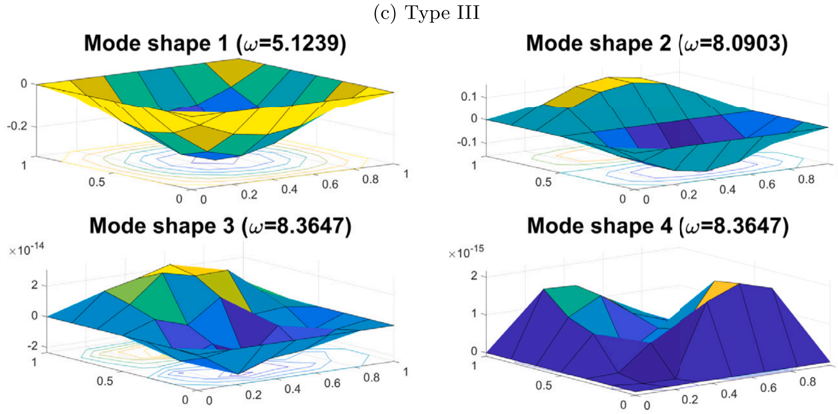

(d) Type IV

Fig. 15. Mode shapes of the first four frequencies of the four types of BC.

Table 15
Summary of the obtained error indices for all damage cases of the studied composite laminate plate using different CICFRFs.

Case	Applied	SNR	NoL = 3, LA = (0°/90°/0°)			NoL = 6, LA = (0°/45°/0°) × 2		
No.	method		MSE	RE	CI	MSE	RE	CI
1	$CICFRF_2$	10	0.0998	-5.2583	-0.7585	0.0802	-5.5757	-0.6031
1	$CICFRF_2$	20	0.0998	-4.0255	-0.6556	0.0978	-6.4502	-0.6025
1	$CICFRF_1$	10	0.00390	-0.1204	0.9460	0.0045	-0.1302	0.9661
1	$CICFRF_1$	20	0.0040	-0.1005	0.9477	0.0040	-0.1256	0.9302
2	$CICFRF_2$	10	0.0997	-4.0025	-0.6354	0.0908	-4.2580	-0.5680
2	$CICFRF_2$	20	0.0935	-3.1025	-0.4261	0.0925	-4.3259	-0.4411
2	$CICFRF_1$	10	0.0040	-0.1188	0.9678	0.0040	-0.0964	0.9758
2	$CICFRF_1$	20	0.0039	-0.1027	0.9756	0.0030	-0.0999	0.9769
3	$CICFRF_2$	10	0.0958	-3.9685	-0.7458	0.0945	-4.3647	-0.4125
3	$CICFRF_2$	20	0.0983	-4.1258	-0.6254	0.0968	-3.3247	-0.4369
3	$CICFRF_1$	10	0.0040	-0.1308	0.9566	0.0056	-0.1644	0.9663
3	$CICFRF_1$	20	0.0040	-0.1156	0.9893	0.0044	-0.1561	0.9597
4	$CICFRF_2$	10	0.0954	-2.3607	-0.6998	0.0969	-6.5057	-0.3653
4	$CICFRF_2$	20	0.0973	-3.4576	-0.7406	0.0993	-4.5269	-0.4205
4	$CICFRF_1$	10	0.0046	-0.1154	0.9763	0.0049	-0.1381	0.9773
4	$CICFRF_1$	20	0.0044	-0.1100	0.9720	0.0054	-0.1266	0.9778

Table 16
First ten natural frequencies of the simulated composite plates with different E_1/E_2 ratios.

Lamination scheme		Mode No.									
		1	2	3	4	5	6	7	8	9	10
Intact, $E_1/E_2 = 20$	NoL = 3, LA = (0°/90°/0°)	6.74	10.13	13.60	15.33	17.52	20.34	22.64	23.14	25.46	25.72
	NoL = 6, LA = (0°/45°/0°) × 2	6.89	10.59	13.87	15.85	18.06	20.95	21.14	22.96	23.98	25.76
Intact, $E_1/E_2 = 30$	NoL = 3, LA = (0°/90°/0°)	7.14	10.70	14.04	15.85	18.21	20.96	23.07	23.60	25.73	25.94
	NoL = 6, LA = (0°/45°/0°) × 2	7.34	11.14	14.40	16.41	18.64	21.56	23.48	24.04	24.55	25.77
Case 4, $E_1/E_2 = 20$	NoL = 3, LA = (0°/90°/0°)	6.55	9.98	13.24	15.07	17.27	19.96	22.01	22.81	24.99	25.13
	NoL = 6, LA = (0°/45°/0°) × 2	6.70	10.41	13.53	15.58	17.74	20.66	20.68	22.39	23.58	25.67
Case 4, $E_1/E_2 = 30$	NoL = 3, LA = (0°/90°/0°)	6.94	10.54	13.68	15.58	17.95	20.56	22.43	23.27	25.12	25.50
	NoL = 6, LA = (0°/45°/0°) × 2	7.14	10.96	14.07	16.15	18.30	21.26	22.89	23.52	24.09	25.22

Table 17
Accuracy indicators of the simulated composite plates with different E_1/E_2 ratios.

Case	E_1/E_2	NoL = 3, LA = 0°/90°/0°			NoL = 6, LA = (0°/45°/0°) × 2		
No.		MSE	RE	CI	MSE	RE	CI
1	40	0.0044	-0.0850	0.9861	0.0042	-0.0936	0.9699
1	30	0.0040	-0.0958	0.9749	0.0040	-0.1002	0.9655
1	20	0.0039	-0.0987	0.9701	0.0040	-0.1007	0.9761
2	40	0.0038	-0.1094	0.9805	0.0038	-0.0858	0.9812
2	30	0.0037	-0.1205	0.9739	0.0040	-0.1172	0.9833
2	20	0.0040	-0.1332	0.9701	0.0042	-0.1277	0.9814
3	40	0.0041	-0.1203	0.9832	0.0049	-0.1304	0.9863
3	30	0.0041	-0.1105	0.9749	0.0048	-0.1122	0.9761
3	20	0.0042	-0.1135	0.9701	0.0048	-0.1017	0.9651
4	40	0.0039	-0.1186	0.9817	0.0031	-0.0935	0.9753
4	30	0.0039	-0.1034	0.9549	0.0040	-0.1172	0.9735
4	20	0.0038	-0.1025	0.9721	0.0041	-0.1107	0.9815

Table 18
The value of σ for all cases as determined by optimization for composite plates with different E_1/E_2 ratios.

	σ			
E_1/E_2 ratios	Case 1	Case 2	Case 3	Case 4
20	1.44	1.34	1.02	1.38
30	1.32	1.12	1.25	1.37

Table 19
The value of σ for all cases as determined by optimization for composite plates with different BCs.

	σ			
BCs	Case 1	Case 2	Case 3	Case 4
Type I	1.04	1.12	1.32	1.30
Type II	1.30	1.25	1.30	1.11
Type III	1.45	1.23	1.13	1.54
Type IV	1.33	1.10	1.20	1.36

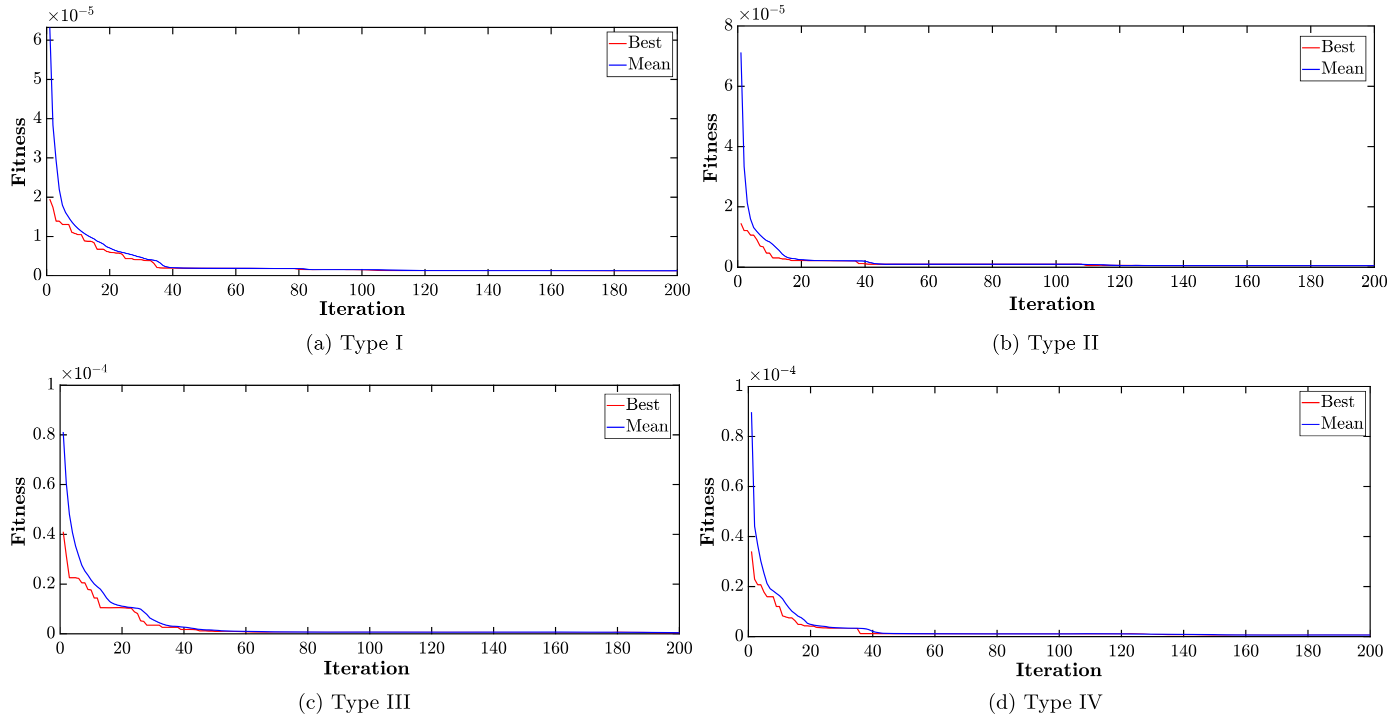

Fig. 16. Convergence of the proposed optimization algorithm for the first damage scenario of the composite plates with different BCs.

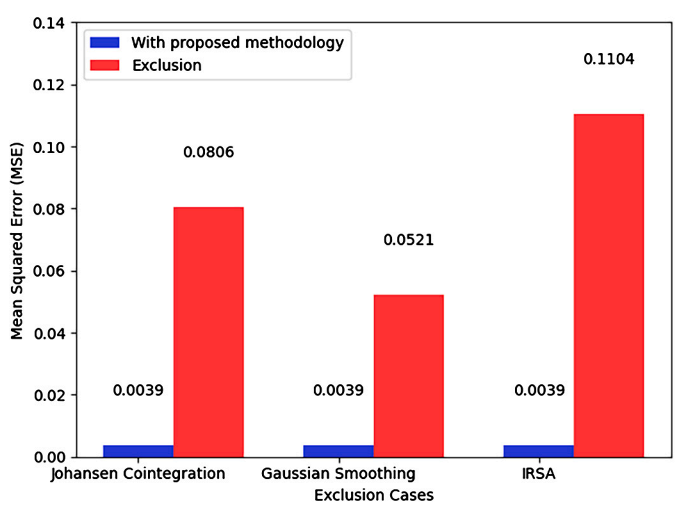

Fig. 17. Impact of exclusion on methodology performance.

non-stationary noise contamination, thus performing poorly in damage detection.

3.1.10. Comparing the authors' previous method ([52]) with the proposed approach

To further demonstrate our proposed method's superiority and accuracy, we compare it with an earlier method proposed by the authors [52]. In this preceding method, the Variational Mode Decomposition of FRFs was used based on the Sum of Unwrapped Instantaneous Hilbert Phases (SUIHP). This method, which is referred to as the SUIHP method, was designed specifically to detect damage in structures contaminated with severe noise and was validated particularly for white noise contamination. Generally, white noise contamination is easier to handle than colored noise. To showcase the capabilities of the proposed method, a direct comparison of these two methods is significant. In this paper, both methods were applied to address the damage detection problem in composite plates. Fig. 19 shows the results obtained from the proposed method and the preceding algorithm (SUIHP) using the composite laminate plates with the specifications NoL = 3 and LA = (0°/90°/0°) and damage case 3. Based on the figure, the superiority of the newly proposed method is clearly demonstrated. As mentioned earlier, the new method is able to successfully remove the non-stationary effects of colored noise while preserving stationary damage characteristics. In contrast, the prior SUIHP method proposed by Hassani et al. [52] yields inferior results.

3.2. Experimental verification

In this section, our proposed method was further validated by solving an experimental problem of a steel beam structure. Fig. 20 illustrates

Table 20
Accuracy indicators obtained for the simulated composite plates with different BC.

Case	BC	NoL = 3, LA = 0°/90°/0°			NoL = 6, LA = (0°/45°/0°) × 2		
No.		MSE	RE	CI	MSE	RE	CI
1	I	0.0040	-0.0845	0.9543	0.0039	-0.0936	0.9555
1	II	0.0040	-0.0958	0.9749	0.0039	-0.1002	0.9657
1	III	0.0039	-0.0957	0.9721	0.0038	-0.1023	0.9654
1	IV	0.0039	-0.0985	0.9561	0.0041	-0.1007	0.9456
2	I	0.0036	-0.1345	0.9843	0.0038	-0.0858	0.9612
2	II	0.0034	-0.1223	0.9711	0.0041	-0.1186	0.9633
2	III	0.0039	-0.1122	0.9601	0.0038	-0.1281	0.9614
2	IV	0.0038	-0.1222	0.9600	0.0039	-0.1290	0.9614
3	I	0.0040	-0.1203	0.9832	0.0044	-0.1314	0.9863
3	II	0.0040	-0.1105	0.9749	0.0045	-0.1134	0.9771
3	III	0.0041	-0.1135	0.9701	0.0046	-0.1022	0.9661
3	IV	0.0038	-0.1135	0.9701	0.0043	-0.1021	0.9666
4	I	0.0037	-0.1186	0.9797	0.0038	-0.0925	0.9653
4	II	0.0037	-0.1034	0.969	0.0040	-0.1162	0.9455
4	III	0.0040	-0.1025	0.9666	0.0040	-0.1117	0.9725
4	IV	0.0041	-0.1025	0.9621	0.0040	-0.1117	0.9525

the flowchart of the proposed method adjusted to the steel beam study. The figure demonstrates the step-by-step procedure of constructing the proposed objective function, which involves smoothing the identified FRFs and fusing them with the Johanson cointegration approach. The resulting objective function was then minimized using the proposed IRSA algorithm to obtain the best possible values for the smoothing factor (σ) and the damage parameters (α).

The experimental study involves a simply supported steel beam inflicted with damage at different locations and of various intensities [53–55] (see Fig. 21). Four identical beams were experimentally tested to study individual damage cases at four different locations. The dimensions of the beams were $12 \times 32 \times 2{,}400$ mm^3. The material properties were as follows: modulus of elasticity 200 GPa, Poisson's ratio 0.3, and density 7850 kg/m3. The beams were attached to concrete supports by using a specially engineered support system, to provide well-defined boundary conditions as close as possible to a pin-pin connection.

A comprehensive analysis was undertaken, investigating 16 single damage cases in the form of notches. These notches were strategically placed at four different locations ('4', '5', '6', and '7') and subjected to four distinct severity levels ('XL', 'L', 'M', 'S'). Each notch had a standardized width of 1 mm, while their lengths varied at 1 mm, 4 mm, 8 mm, and 12 mm. The severity of damage was quantified by measuring the cross-sectional losses of the second moment of area (I), expressed as percentages—9.09%, 33.01%, 57.81%, and 75.59%. To induce damage, a saw cut was applied progressively from the soffit of the beams. For a visual representation of the four severity levels, refer to Fig. 22. This systematic approach allowed for a comprehensive exploration of the impact of different notch locations and severity levels on the structural integrity of the beams.

Modal testing and experimental modal analysis were performed on the steel beams to determine their dynamic properties. Fig. 24 presents the utilized testing equipment and a diagram of the modal testing and experimental modal analysis setup is shown in Fig. 23. A modally tuned impact hammer was used in the testing to stimulate the beams at a particular reference point and nine accelerometers were used to measure the beam's responses.

The main data acquisition equipment consisted of a Hewlett Packard dynamic analyzer (model E1432A) Vxi system that was equipped with an HP Vxi 16 channel 51.2 kHz digitizer with anti-aliasing filters. The experiment modal analysis software package, LMS CADA-X, was used to record the data from the data acquisition system and post-process it on a personal computer.

For each test, the sampling rate was set to 10,000 Hz with 16,384 time domain data points being recorded. In the frequency domain, this

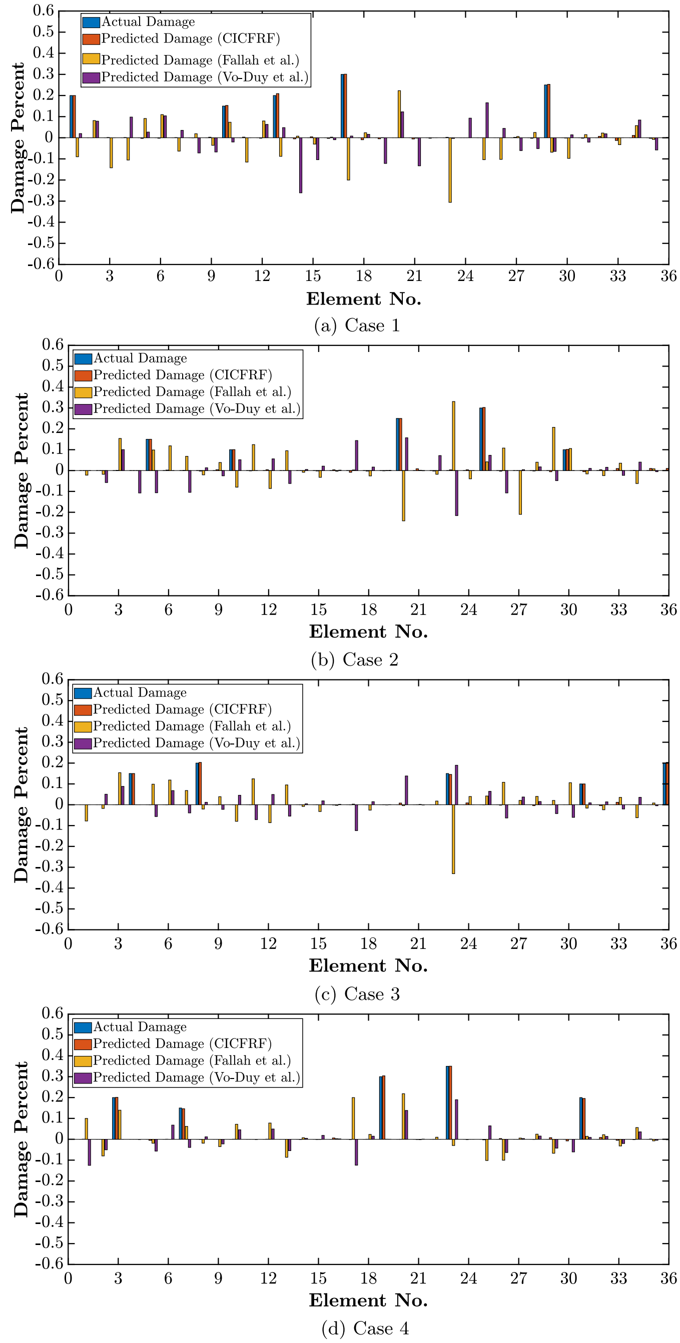

Fig. 18. Damage indices obtained from one time running of CIFRF, [46], and [45]; brown noise, SNR = 10; NoL = 3, LA = (0°/90°/0°).

corresponds to a frequency range of 5,000 Hz with 8,192 FRF data points, thus giving a frequency resolution of 0.61 Hz per data point. The acquired impact and response time history signals (amplitude versus time) were then converted into frequency spectra (amplitude versus frequency) using the Fourier transform. By dividing the Fourier transform signals of the accelerometers (output) by the Fourier transform signal of the hammer impact (input), the FRFs were obtained. For each state of the beam (undamaged state and each damaged state), five averaged FRFs (from 15 different hammer hits) were recorded. Thereby 25 test measurements were obtained from each steel beam and 100 measurements from the entire test series.

A list of the natural frequencies of the first seven modes of Beams 1 to 4 can be found in Table 22. Fig. 25 presents FRFs of the experimental steel beams in the intact state and various damaged states for

Table 21
Accuracy indicators obtained comparing the proposed method with two comparative methods (Fallah et al. [46], and Vo-Duy et al. [45]).

Case	Applied	SNR	NoL = 3, LA = (0°/90°/0°)			NoL = 6, LA = (0°/45°/0°) × 2		
No.	method		MSE	RE	CI	MSE	RE	CI
1	Fallah et al. [46]	10	0.0976	-4.7865	-0.9000	0.0987	-4.4390	-0.9098
1	Fallah et al. [46]	20	0.0967	-4.0576	-0.8565	0.0943	-3.4123	-0.8975
1	Vo-Duy et al. [45]	10	0.0758	-6.8842	-0.8829	0.0825	-4.0326	-0.8863
1	Vo-Duy et al. [45]	20	0.0788	-6.9280	-0.8775	0.0976	-6.0548	-0.9432
1	Proposed method	10	0.00390	-0.1204	0.9460	0.0045	-0.1302	0.9661
1	Proposed method	20	0.0040	-0.1005	0.9477	0.0040	-0.1256	0.9302
2	Fallah et al. [46]	10	0.0954	-5.0076	-0.8458	0.0890	-5.4345	-0.8883
2	Fallah et al. [46]	20	0.0990	-5.8076	-0.7543	0.0865	-5.5556	-0.7775
2	Vo-Duy et al. [45]	10	0.0762	-5.8088	-0.7999	0.0799	-6.3088	-0.8979
2	Vo-Duy et al. [45]	20	0.0750	-3.9986	-0.5446	0.0983	-4.7672	-0.7546
2	Proposed method	10	0.0040	-0.1188	0.9678	0.0040	-0.0964	0.9758
2	Proposed method	20	0.0039	-0.1027	0.9756	0.0030	-0.0999	0.9769
3	Fallah et al. [46]	10	0.0792	-4.0980	-0.8887	0.0888	-6.8459	-0.9771
3	Fallah et al. [46]	20	0.0876	-5.3654	-0.7879	0.0909	-5.7456	-0.8882
3	Vo-Duy et al. [45]	10	0.0976	-4.9088	-0.8464	0.0958	-6.2589	-0.9635
3	Vo-Duy et al. [45]	20	0.0678	-7.1000	-0.8345	0.0803	-5.7896	-0.5672
3	Proposed method	10	0.0040	-0.1308	0.9566	0.0056	-0.1644	0.9663
3	Proposed method	20	0.0040	-0.1156	0.9893	0.0044	-0.1561	0.9597
4	Fallah et al. [46]	10	0.0772	-5.0030	-0.7896	0.0888	-5.8669	-0.8871
4	Fallah et al. [46]	20	0.0888	-5.3885	-0.5670	0.0876	-6.5555	-0.7882
4	Vo-Duy et al. [45]	10	0.0678	-4.8600	-0.8672	0.0654	-7.2589	-0.4561
4	Vo-Duy et al. [45]	20	0.0765	-6.6000	-0.6750	0.0703	-6.6786	-0.7832
4	Proposed method	10	0.0046	-0.1154	0.9763	0.0049	-0.1381	0.9773
4	Proposed method	20	0.0044	-0.1100	0.9720	0.0054	-0.1266	0.9778

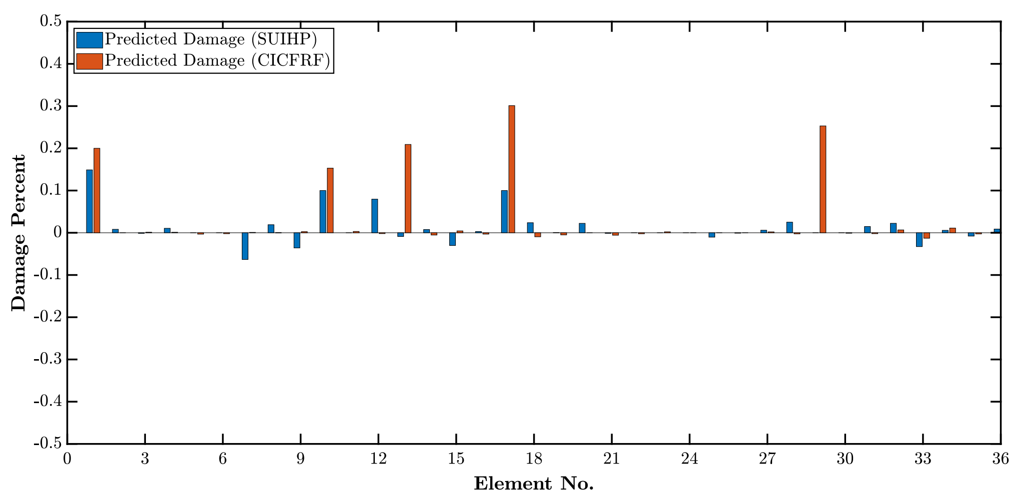

Fig. 19. Damage indices obtained comparing CIFRF and SUIHP, brown noise, SNR = 10; NoL = 3, LA = (0°/90°/0°) and damage case 3.

Beam 4. The FRF summation functions from different beams in the undamaged state at reference points H1, H2, H3, H4, and H5 are shown in Fig. 26. Fig. 25 shows the effect of different damage severity and Fig. 26 illustrates the impact of various damage locations on the FRF summation function. As mentioned before, in our proposed method, the smoothed FRFs corresponding to various excitations and scenarios can be combined using Johansen Cointegration. Fused smoothed FRFs are then used as inputs for the proposed objective function.

A matching numerical model of the tested steel beams was created in MATLAB. The numerical model simulated the beams with 24 elements. The damage was inflicted at the nodes, and the damage extent was simulated as a reduction in the EI of the beam cross-section at the corresponding node. The model was set to be optimized through the proposed procedure to identify the damage location and severity. To this end, first, the proposed objective function was constructed and then, the proposed IRSA algorithm was employed to optimize the objective function to obtain optimal values for the σ and α.

As shown in Fig. 27, different values of σ have different effects on smoothing. For large σ, the signal is over-smoothed, whereas a small σ introduces little smoothing to the FRF signals. Based on the results of optimizing the objective function, the results of the last column of Table 23 were identified as the optimal value for smoothing FRFs which also led to the optimal damage indices. Upon examining the non-smoothed FRFs depicted in Figs. 25 and 26, it is evident that there are significant error measurements and a considerable amount of noise present. However, we can effectively address these issues by applying a Gaussian smoothing technique.

The results presented in Table 24 showcase the effectiveness of the proposed methods in accurately predicting the severity of damages and identifying their respective locations with the comparison of the actual damage. The results show that our proposed method is capable of de-

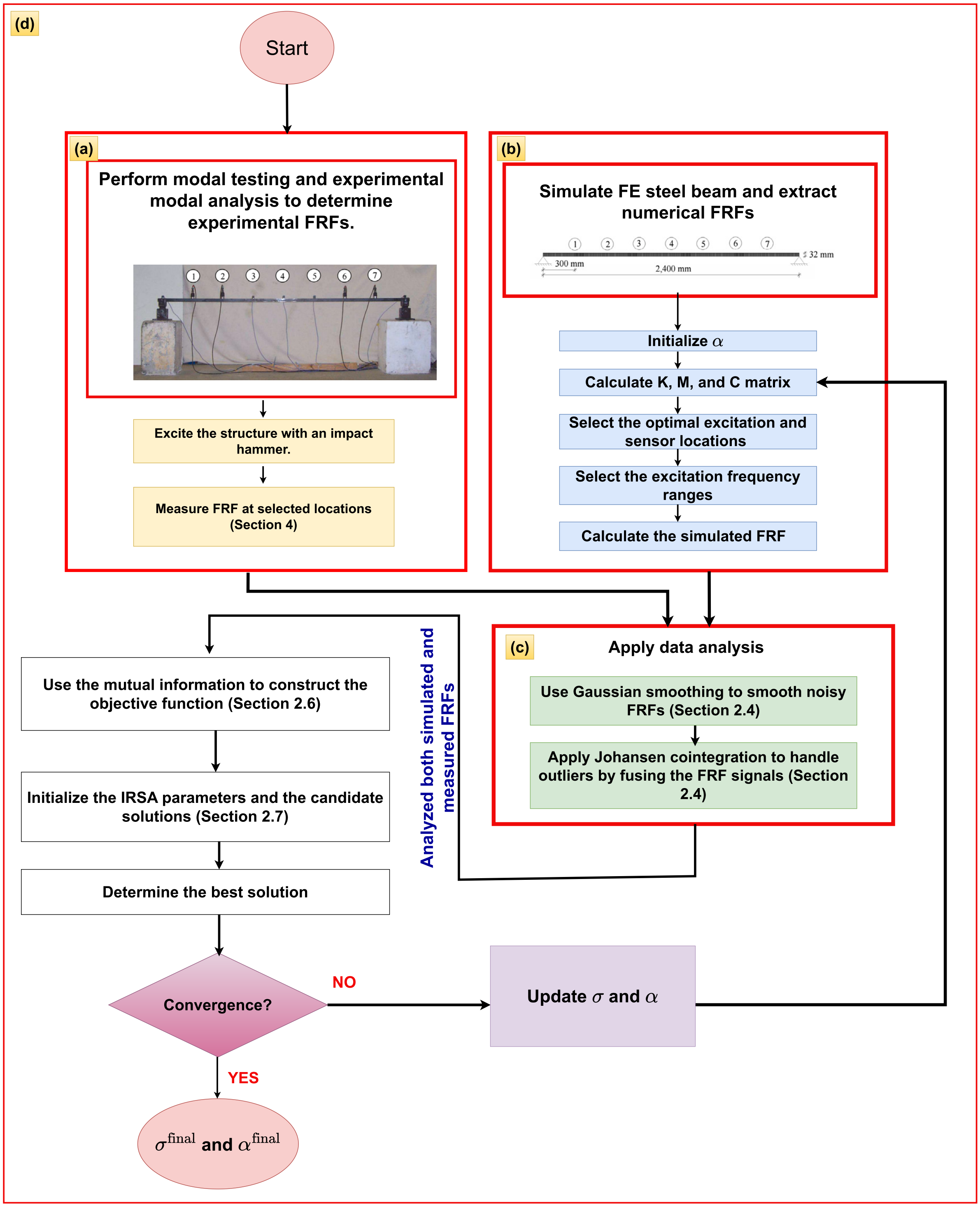

Fig. 20. Methodology of the proposed method applied to the experimental and numerical steel beam study ((a) conduct modal testing; (b) simulate a steel beam using Finite Element (FE) analysis; (c) apply data analytic methods to the obtained results; (d) implement the proposed approach or methodology).

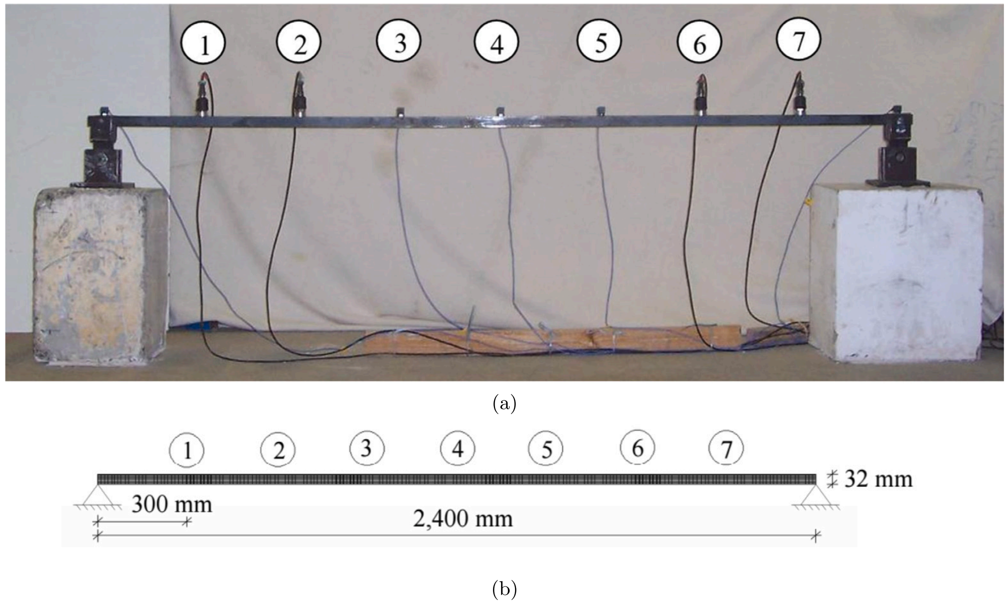

Fig. 21. (a) Experimental test set up, and (b) numerical steel beam model [55,56].

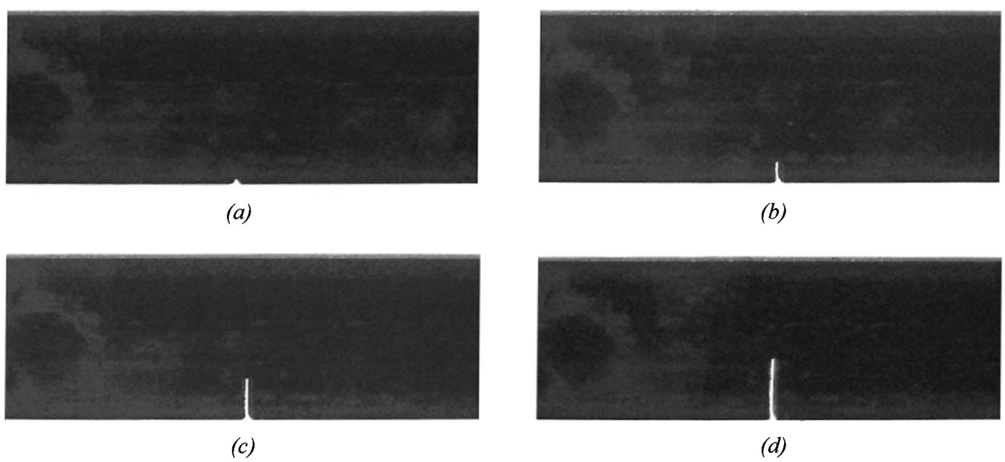

Fig. 22. Experimental damage severity (a) 1 mm, (b) 4 mm, (c) 8 mm, and (d) 12 mm cut [55,56].

tecting damage in the exact location, and the severity predicted is close to the actual severity. The achieved accuracy and robustness highlight the reliability of the approach even after 200 iterations of the proposed IRSA. This demonstrates the capability of the proposed method to precisely determine damage locations and estimate their severity, which is crucial in various practical applications.

Figs. 28, 29, 30, and 31 visually represent the predicted damage locations and severity for different cases. These figures provide concrete evidence of the proposed method's ability to update and adapt to experimental problems. In these figures, the accuracy of the predicted damage locations and severity further validates the applicability of the proposed approach in practical scenarios.

To further scrutinize the outcomes of the damage identification process, Table 23 is provided, which displays the accuracy indices CI, MSE, and RE for different laminated composite models. As mentioned before, a predicted outcome is considered more accurate when the values of |CI|, |MSE|, and |RE| are closer to 1, 0, and 0, respectively. The values of |CI|, |MSE|, and |RE| for this method indicate a higher level of accuracy, approaching the desired ideal values. This suggests that the damage identification results obtained using a combination of proposed optimization and processed FRFs are more precise and reliable, showcasing the effectiveness of the proposed approach.

The convergence of the proposed optimization algorithm is visually represented in Figs. 32, 33, 34, and 35 for all beams with different types of damage over 200 iterations. These figures provide clear evidence of the optimization process, reinforcing the reliability and precision of the proposed algorithm. Upon closer examination of the figures, it is evident that the objective function is optimized perfectly. The optimization process reaches a state where the objective function is minimized or maximized, depending on the nature of the problem. This achievement is crucial in demonstrating the effectiveness of the proposed optimization algorithm. The convergence observed in the figures signifies the successful optimization of the objective function, implying that the proposed algorithm has effectively found the optimal solution within the given constraints. This convergence further reinforces the accuracy and robustness of the proposed optimization algorithms, as well as the effectiveness of the proposed objective functions. As a result, the optimization process is well-optimized, showcasing the accuracy and robustness of the proposed optimization algorithm and objective functions. These

Table 22
First seven natural frequencies of the experimental steel beam.

Type		Mode No.						
		1	2	3	4	5	6	7
Intact	Beam 1	21.60	40.07	129.37	221.49	310.39	448.69	614.30
4XL	Beam 1	21.62	40.09	129.27	221.64	310.78	448.97	615.41
4L	Beam 1	21.49	40.12	129.43	222.06	310.15	449.24	613.78
4M	Beam 1	21.44	40.07	128.03	221.33	307.18	448.65	610.25
4S	Beam 1	21.37	40.05	126.50	220.68	305.34	448.62	601.10
Intact	Beam 2	20.27	40.71	125.02	215.96	302.79	477.86	616.27
5XL	Beam 2	20.23	40.64	125.24	216.01	302.89	478.99	617.39
5L	Beam 2	20.18	40.69	125.40	215.78	300.58	480.03	616.65
5M	Beam 2	20.30	40.36	125.70	213.47	299.06	477.59	612.14
5S	Beam 2	20.29	40.31	126.05	212.24	289.52	476.78	604.19
Intact	Beam 3	21.09	40.21	127.86	218.05	307.09	483.94	616.62
6XL	Beam 3	20.97	40.04	128.31	218.39	305.22	470.56	616.08
6L	Beam 3	21.04	40.15	128.04	218.91	305.12	478.01	615.37
6M	Beam 3	21.04	39.98	127.64	218.24	304.85	480.37	613.17
6S	Beam 3	20.93	39.54	126.64	218.34	304.54	479.66	607.02
Intact	Beam 4	21.01	39.56	124.41	209.65	300.44	476.46	606.48
7XL	Beam 4	20.94	39.41	123.94	205.22	299.19	469.37	609.10
7L	Beam 4	20.77	39.58	123.91	208.80	298.54	476.57	607.12
7M	Beam 4	20.77	39.50	123.59	207.33	297.83	472.93	605.13
7S	Beam 4	20.77	39.16	123.20	206.50	292.96	471.89	604.05

results validate the effectiveness of the proposed approach in achieving the desired optimization goals.

In addition, the computational efficiency of the proposed method is evaluated and summarized in the last column of Table 24, which presents the central processing unit (CPU) times for all the studied cases. CPU time, also known as process time, refers to the duration during which a CPU time is actively engaged in executing instructions for a computer program or operating system. It is distinct from elapsed time, which encompasses various activities such as waiting for input/output (I/O) operations or entering low-power mode. These results play a vital role in assessing the feasibility of implementing the proposed approach in practical applications. The obtained CPU times indicate that the proposed method delivers results within reasonable computational limits. The computational times remain low, implying that the method can be effectively utilized for damage detection in real systems. This is a crucial advantage as it allows for high-accuracy damage identification without excessively consuming computational resources. The convergence of the objective function with a high level of accuracy, as observed in the optimization results, further affirms the effectiveness of the proposed method. The optimization process successfully achieved the desired optimization goals, showcasing the reliability and precision of the approach. By saving computation time, the proposed approach becomes more practical and applicable in real-world scenarios where time constraints are crucial.

Table 23
Accuracy indices of the obtained results.

Beam	Damage	MSE	RE	CI	σ
Beam 1	4XL	0.0048	-0.1104	0.9260	2.01
Beam 1	4L	0.0044	-0.1050	0.9333	2.06
Beam 1	4M	0.0044	-0.1042	0.9433	2.07
Beam 1	4S	0.0043	-0.1022	0.9533	2.15
Beam 2	5XL	0.0048	-0.1234	0.9091	2.21
Beam 2	5L	0.0048	-0.1222	0.9131	2.22
Beam 2	5M	0.0046	-0.1141	0.9344	2.16
Beam 2	5S	0.0044	-0.1122	0.9433	2.11
Beam 3	6XL	0.0050	-0.1345	0.9062	2.10
Beam 3	6L	0.0048	-0.1322	0.9231	2.29
Beam 3	6M	0.0047	-0.1241	0.9353	2.28
Beam 3	6S	0.0046	-0.1041	0.9400	2.01
Beam 4	7XL	0.0049	-0.1435	0.9143	2.15
Beam 4	7L	0.0047	-0.1333	0.9225	2.13
Beam 4	7M	0.0047	-0.1200	0.9352	2.17
Beam 4	7S	0.0046	-0.1030	0.9407	2.23

4. Conclusions

Based on the findings and results presented in this study, the proposed method can significantly contribute to the field of SHM by overcoming the challenge introduced by the presence of outliers in the detected dataset. The novel usage of Johansen cointegration as a data fusion technique has proven to be effective in handling outliers in FRF signals, enhancing the robustness of the proposed approach. It is noteworthy to mention that Johansen cointegration is more capable of handling low-frequency outliers in a set of datasets. Therefore, to overcome the challenge introduced by high-frequency noise contamination, it has been further integrated with Gaussian smoothing. Such a novel hybrid approach was shown to be efficient in managing both high-frequency and low-frequency outliers while enabling the preservation of crucial information in the dataset for use in SHM.

Moreover, the introduction of a new objective function incorporating concepts of mutual information has shown promise in creating a smoother search space for optimizing damage indices. The proposed DSF has also demonstrated its efficacy in managing outliers stemming from non-stationary noise or measurement errors in FRF signals. Furthermore, to enhance the detectability of damage, some improvements to the RSA optimization algorithm have been introduced. Through rigorous evaluation and numerical analysis of the proposed optimization algorithm, the Improved RSA (IRSA) demonstrated its superior performance by comparison with various established benchmarks, showcasing its accuracy and robustness.

The effectiveness of the proposed method was numerically validated on composite plates, providing valuable insights into the impacts of different parameters in damage detection. Furthermore, successful validation through an experimental damage detection scenario on steel beams has underscored the real-world applicability and reliability of our proposed method. Comparative analyses with other state-of-the-art methods have consistently highlighted the superiority of the proposed method, indicating its potential for widespread practical application. Collectively, these findings emphasize the significance and potential impact of the proposed method in advancing the field of SHM.

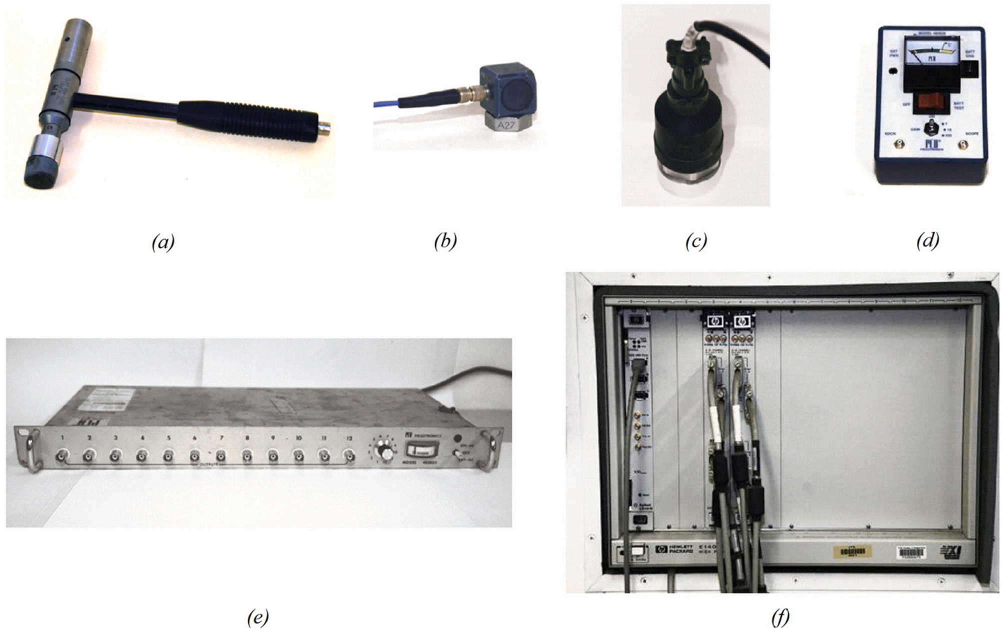

Fig. 23. Test equipment: (a) modal hammer model HP 086C05, (b) accelerometer model PCB 356A08, (c) accelerometer model PCB 337A26, (d) battery-powered signal conditioner, (e) multi-channel signal conditioner, and (f) data acquisition system [56].

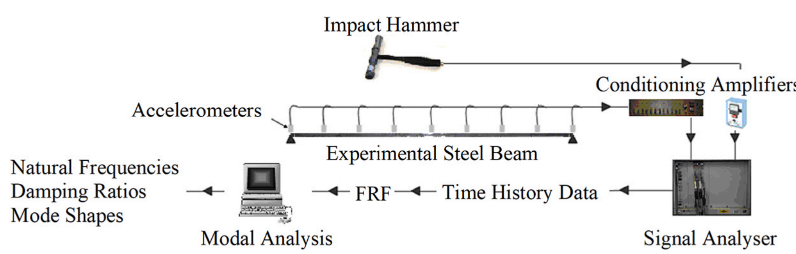

Fig. 24. Schematic diagram of MT& EMA [55,56].

Table 24
Damage severity predictions using the proposed IRSA after 200 iterations.

Beam	Damage type	Actual damage location (m)	Actual damage severity	Predicted damage location (m)	Predicted damage severity	CPU Time (sec)
Beam 1	4XL	1.2	0.0909	1.2	0.09487	160
Beam 1	4L	1.2	0.3301	1.2	0.3243	158
Beam 1	4M	1.2	0.5781	1.2	0.5770	163
Beam 1	4S	1.2	0.7559	1.2	0.7459	159
Beam 2	5XL	1.5	0.0909	1.5	0.0873	156
Beam 2	5L	1.5	0.3301	1.5	0.3211	164
Beam 2	5M	1.5	0.5781	1.5	0.5962	166
Beam 2	5S	1.5	0.7559	1.5	0.7301	169
Beam 3	6XL	1.8	0.0909	1.8	0.0953	173
Beam 3	6L	1.8	0.3301	1.8	0.3112	165
Beam 3	6M	1.8	0.5781	1.8	0.5700	160
Beam 3	6S	1.8	0.7559	1.8	0.7411	162
Beam 4	7XL	2.1	0.0909	2.1	0.0801	150
Beam 4	7L	2.1	0.3301	2.1	0.3421	172
Beam 4	7M	2.1	0.5781	2.1	0.5651	168
Beam 4	7S	2.1	0.7559	2.1	0.7532	163

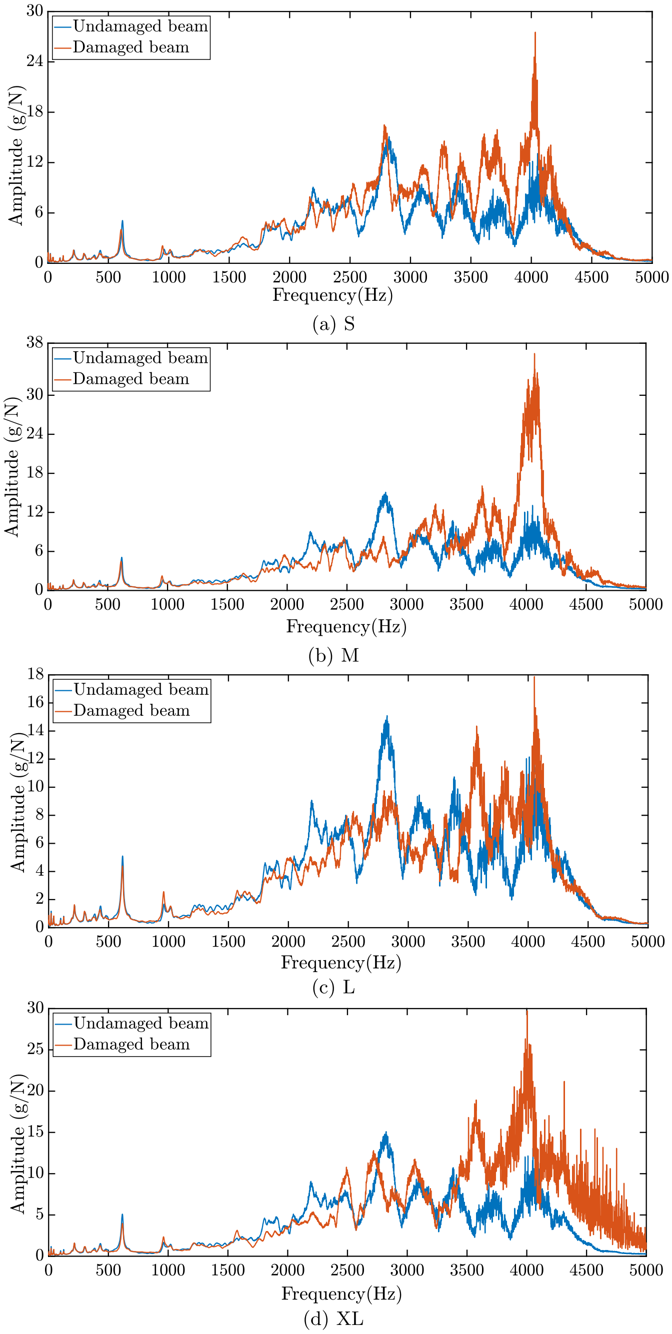

Fig. 25. Effects of different damage severity on FRF data. Displayed are FRF summation functions from Beam 4 in the undamaged state and damaged states with defects at location ‘3’ of severity extra-light (XL), light (L), medium (M), and severe (S).

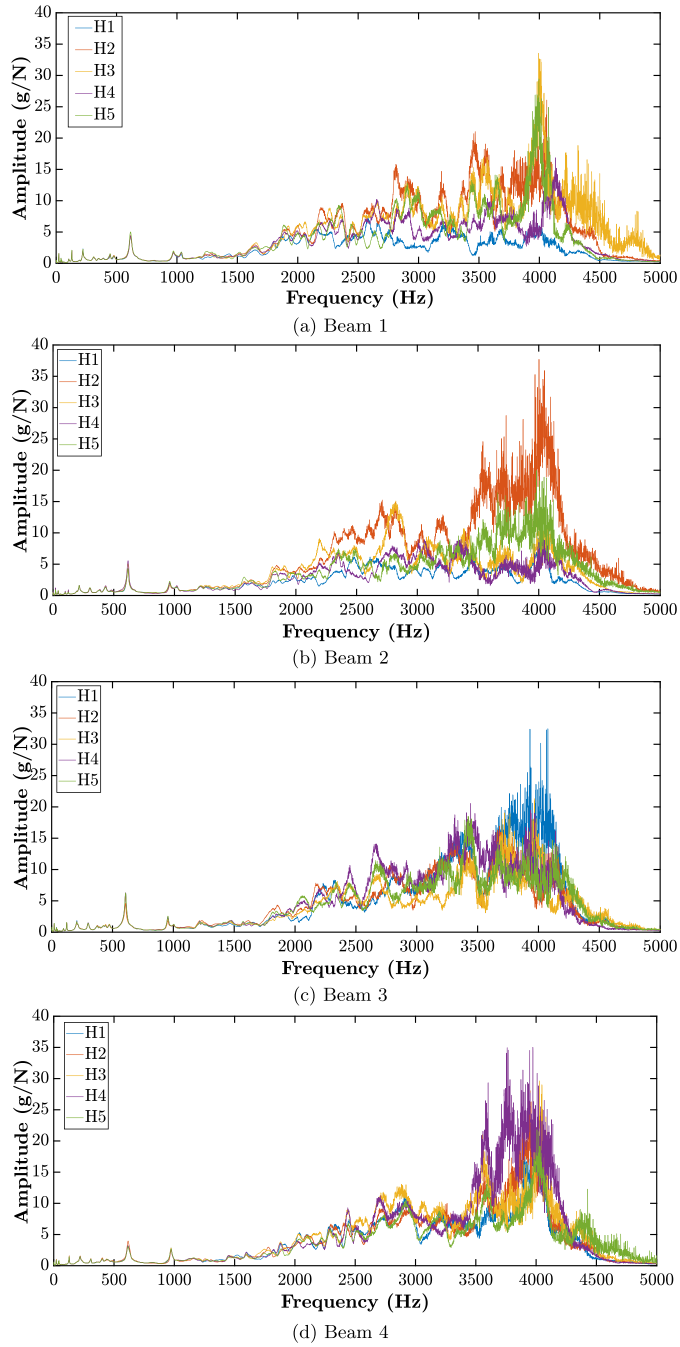

Fig. 26. FRF summation functions of impact points H1, H2, H3, H4, and H5.

The authors acknowledge the importance of assessing the generalizability of the proposed method amidst severe environmental conditions. Therefore, future work should be devoted to investigating the efficacy of the proposed method in detecting structural damage under varying severe environmental conditions.

Replication of results

No results are presented.

CRediT authorship contribution statement

Sahar Hassani: Conceptualization, Data curation (Simulation), Formal analysis, Investigation, Methodology, Resources (Simulation), Software, Validation, Visualization, Writing – original draft, Writing – review & editing. **Ulrike Dackermann:** Data curation (Experimental), Visualization, Funding acquisition, Project administration, Resources (Experimental), Supervision, Writing – review & editing. **Mohsen Mousavi:** Visualization, Supervision, Writing – review & editing. **Jianchun Li:** Supervision, Visualization, Project administration, Writing – review & editing.

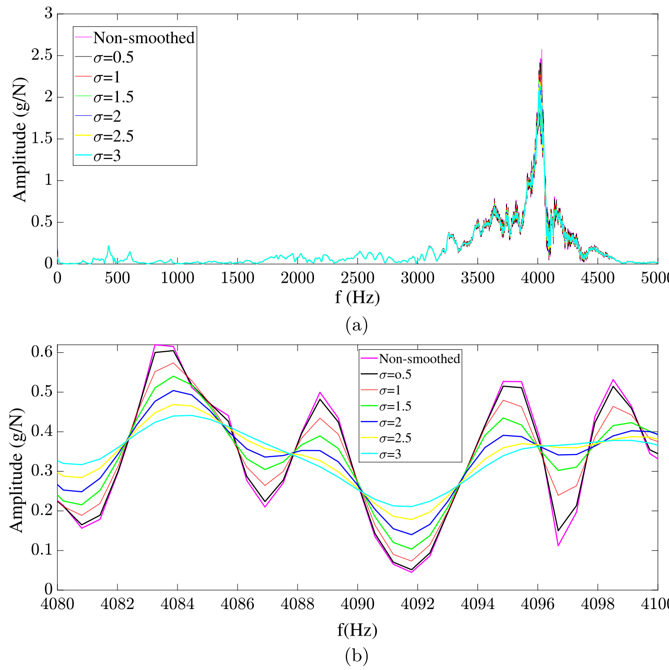

Fig. 27. FRF smoothing of beam 2 with severe damage (S) using different values of σ; (a) whole spectrum and (b) zoomed spectrum.

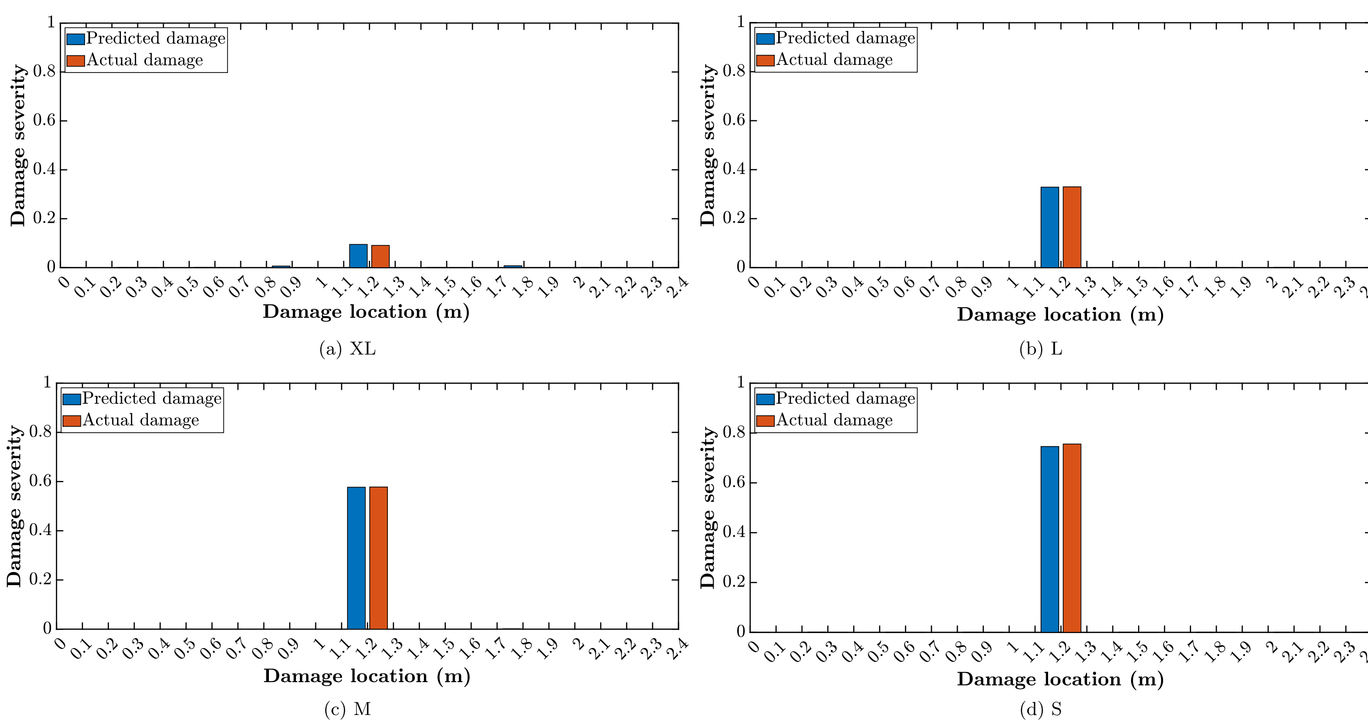

Fig. 28. Identified damage severity using processed FRF data from Beam 1.

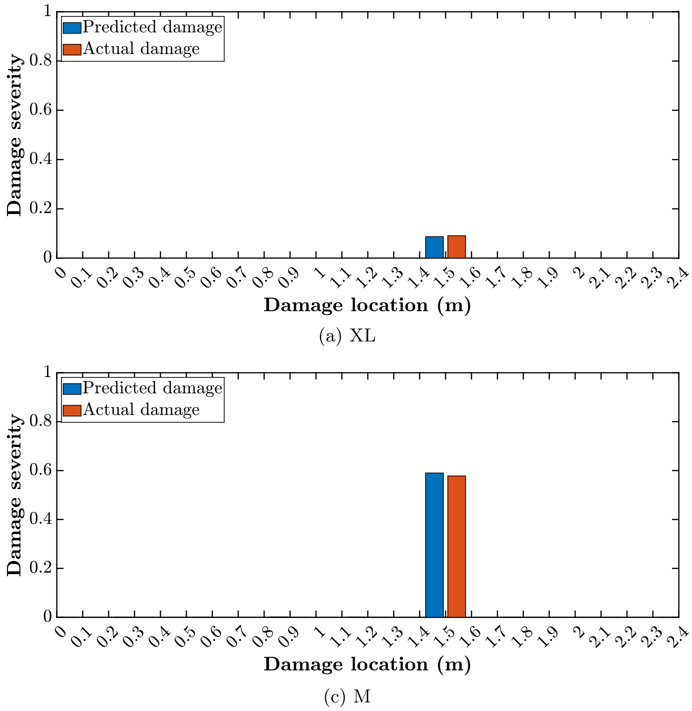

Fig. 29. Identified damage severity using processed FRF data from Beam 2.

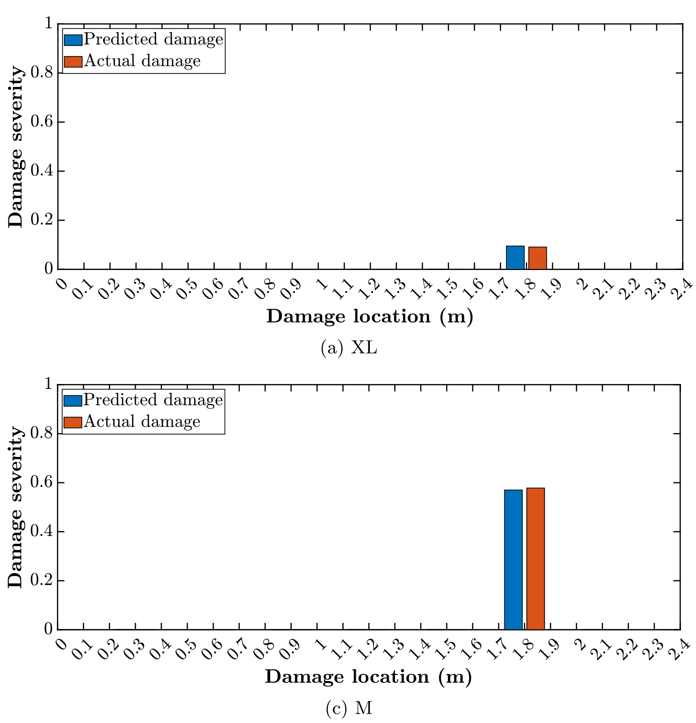

Fig. 30. Identified damage severity using processed FRF data from Beam 3.

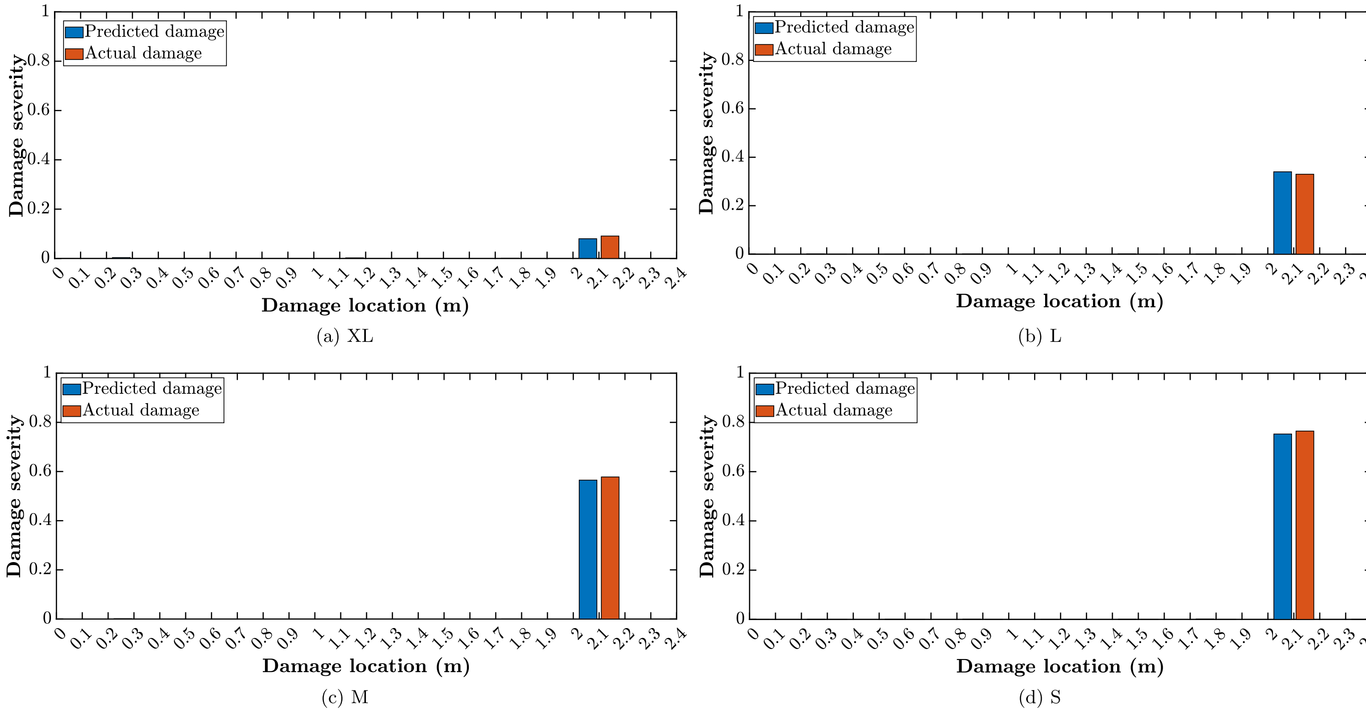

Fig. 31. Identified damage severity using processed FRF data from Beam 4.

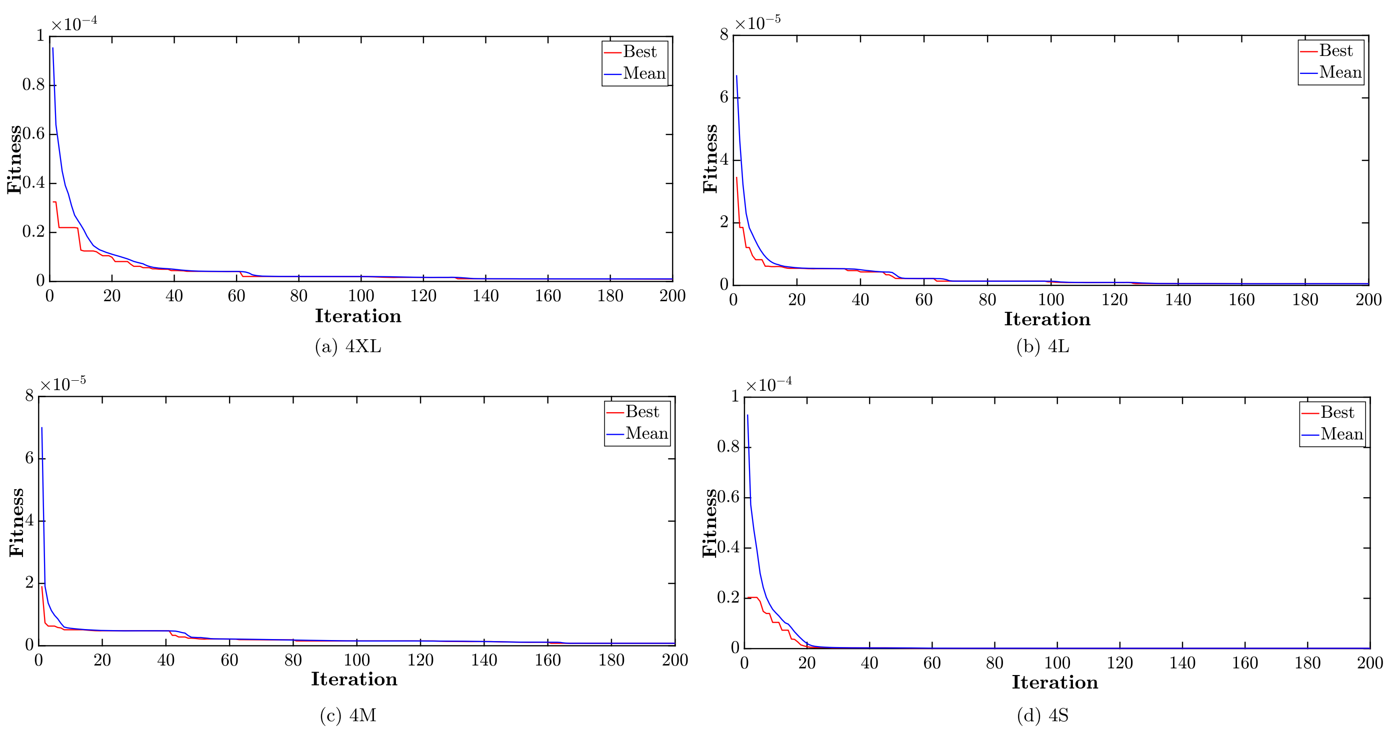

Fig. 32. Convergence of the proposed optimization algorithm for damage scenarios 1-4 in steel beam 1.

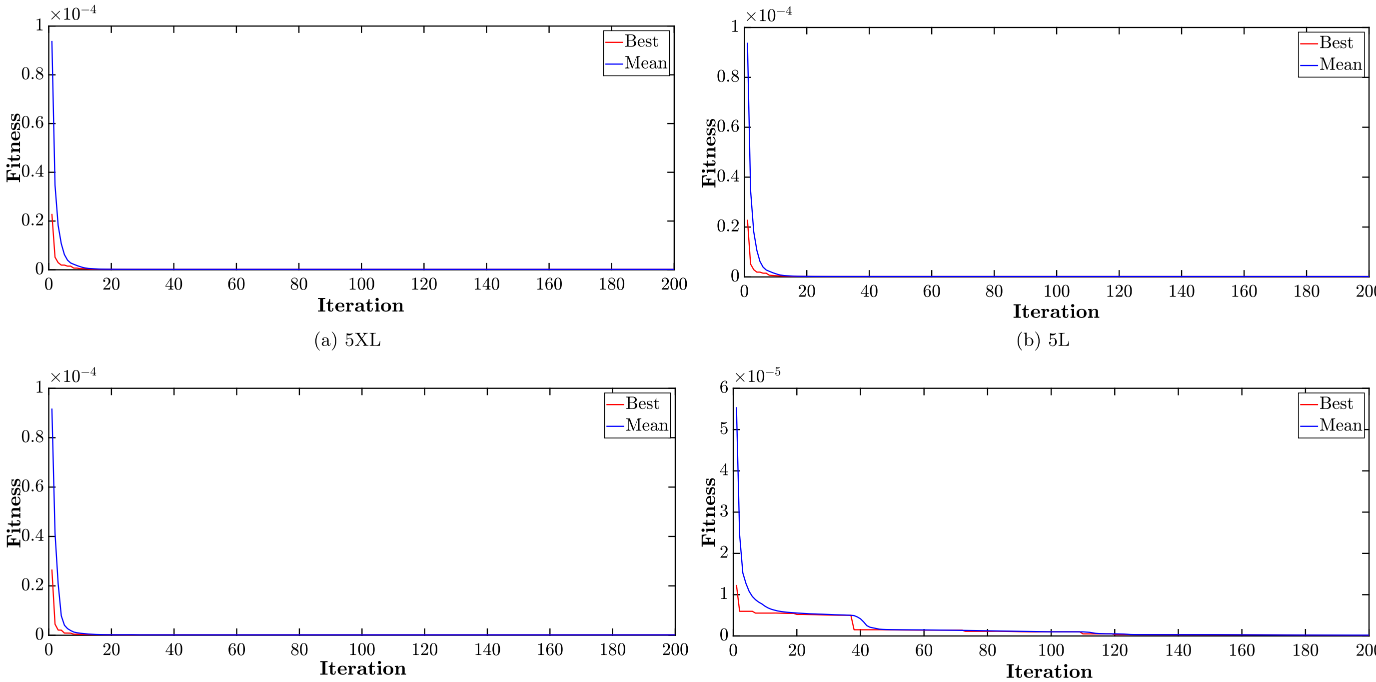

(a) 5XL (b) 5L

(c) 5M (d) 5S

Fig. 33. Convergence of the proposed optimization algorithm for damage scenarios 1-4 in steel beam 2.

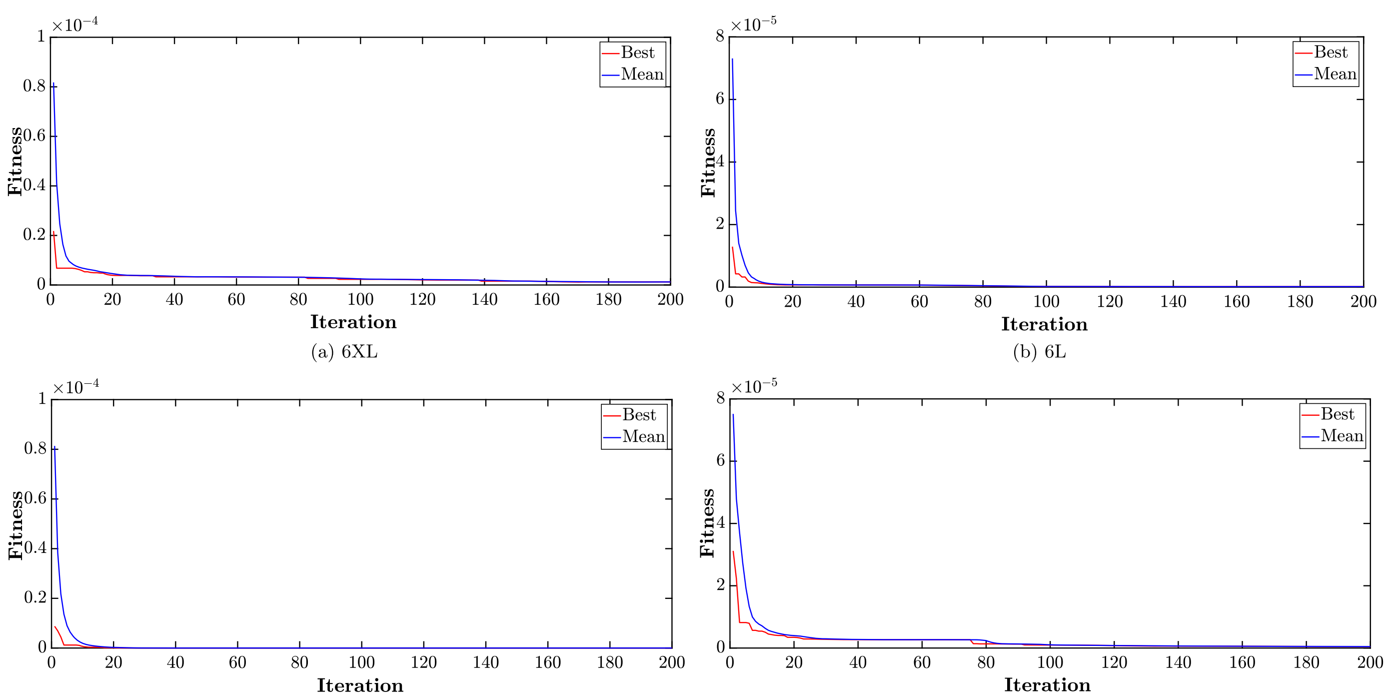

(a) 6XL (b) 6L

(c) 6M (d) 6S

Fig. 34. Convergence of the proposed optimization algorithm for damage scenarios 1-4 in steel beam 3.

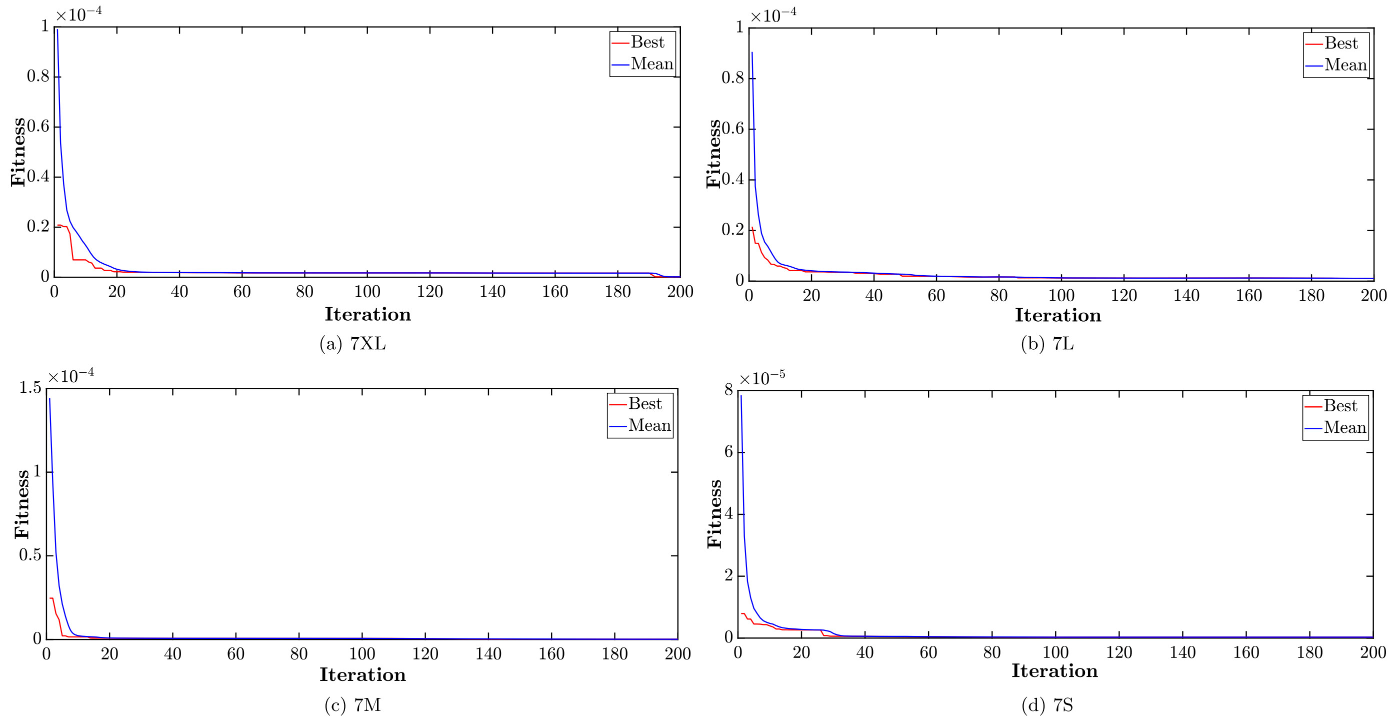

Fig. 35. Convergence of the proposed optimization algorithm for damage scenarios 1-4 in steel beam 4.

Declaration of competing interest

The authors declare that they have no known competing financial interests or personal relationships that could have appeared to influence the work reported in this paper.

Data availability

Data will be made available on request.

References

[1] de Castro BA, Baptista FG, Ciampa F. Comparative analysis of signal processing techniques for impedance-based shm applications in noisy environments. Mech Syst Signal Process 2019;126:326–40.
[2] Wang X, Chakraborty J, Niederleithinger E. Noise reduction for improvement of ultrasonic monitoring using coda wave interferometry on a real bridge. J Nondestruct Eval 2021;40:1–14.
[3] Zhang C, Mousavi AA, Masri SF, Gholipour G, Yan K, Li X. Vibration feature extraction using signal processing techniques for structural health monitoring: a review. Mech Syst Signal Process 2022;177:109175.
[4] Figueiredo E, Brownjohn J. Three decades of statistical pattern recognition paradigm for shm of bridges. Struct Health Monit 2022;21(6):3018–54.
[5] Chen SY, Wang YW, Ni YQ. Gross outlier removal and fault data recovery for shm data of dynamic responses by an annihilating filter-based Hankel-structured robust pca method. Struct Control Health Monit 2022;29(12):e3144.
[6] Fan W, Qiao P. Vibration-based damage identification methods: a review and comparative study. Struct Health Monit 2011;10(1):83–111.
[7] Bandara RP, Chan TH, Thambiratnam DP. Structural damage detection method using frequency response functions. Struct Health Monit 2014;13(4):418–29.
[8] Jonscher C, Liesecke L, Penner N, Hofmeister B, Grießmann T, Rolfes R. Influence of system changes on closely spaced modes of a large-scale concrete tower for the application to structural health monitoring. J Civ Struct Health Monit 2023:1–18.
[9] Brincker R, Lopez-Aenlle M. Mode shape sensitivity of two closely spaced eigenvalues. J Sound Vib 2015;334:377–87.
[10] Zhu T, Zang C, Zhang G. Noise reduction for modal parameter identification of the measured frfs using the modal peak-based Hankel-svd method. In: Shock and vibration 2020; 2020.
[11] Beale C, Niezrecki C, Inalpolat M. An adaptive wavelet packet denoising algorithm for enhanced active acoustic damage detection from wind turbine blades. Mech Syst Signal Process 2020;142:106754.
[12] de Castro BA, Baptista FG, Ciampa F. New signal processing approach for structural health monitoring in noisy environments based on impedance measurements. Measurement 2019;137:155–67.
[13] Das S, Saha P. Performance of hybrid decomposition algorithm under heavy noise condition for health monitoring of structure. J Civ Struct Health Monit 2020;10:679–92.
[14] Fan G, Li J, Hao H. Vibration signal denoising for structural health monitoring by residual convolutional neural networks. Measurement 2020;157:107651.
[15] Sarrafi A, Mao Z, Shiao M. Uncertainty quantification framework for wavelet transformation of noise-contaminated signals. Measurement 2019;137:102–15.
[16] Hanson D, Randall R, Antoni J, Thompson D, Waters T, Ford R. Cyclostationarity and the cepstrum for operational modal analysis of mimo systems—part i: Modal parameter identification. Mech Syst Signal Process 2007;21(6):2441–58.
[17] Adhikari K, Kay S. Optimal sparse sampling for detection of a known signal in nonwhite gaussian noise. IEEE Signal Process Lett 2021;28:1908–12.
[18] Luo J, Hong Y, Li C, Sun Y, Liu X, Yan Z. Frequency identification based on power spectral density transmissibility under unknown colored noise excitation. Comput Struct 2022;263:106741.
[19] Alamdari MM, Li J, Samali B. FRF-based damage localization method with noise suppression approach. J Sound Vib 2014;333(14):3305–20.
[20] Johansen S. Statistical analysis of cointegration vectors. J Econ Dyn Control 1988;12(2–3):231–54.
[21] Cross EJ, Worden K. Cointegration and why it works for shm. J Phys Conf Ser 2012;382:012046. IOP Publishing.
[22] Cross EJ, Worden K, Chen Q. Cointegration: a novel approach for the removal of environmental trends in structural health monitoring data. Proc R Soc A, Math Phys Eng Sci 2011;467(2133):2712–32.
[23] Li X, Qu W, Xiao L, Lu Y. Removal of temperature effect in impedance-based damage detection using the cointegration method. J Intell Mater Syst Struct 2019;30(15):2189–97.
[24] Dao PB, Klepka A, Pieczonka Ł, Aymerich F, Staszewski WJ. Impact damage detection in smart composites using nonlinear acoustics—cointegration analysis for removal of undesired load effect. Smart Mater Struct 2017;26(3):035012.
[25] Dao PB, Staszewski WJ. Cointegration and how it works for structural health monitoring. Measurement 2023;209:112503.
[26] Tome ES, Pimentel M, Figueiras J. Damage detection under environmental and operational effects using cointegration analysis–application to experimental data from a cable-stayed bridge. Mech Syst Signal Process 2020;135:106386.
[27] Hassani S, Dackermann U, Mousavi M, Li J. A systematic review of data fusion techniques for optimized structural health monitoring. Inf Fusion 2023:102136.
[28] Ramesh S, Nirmalraj S, Murugan S, Manikandan R, Al-Turjman F. Optimization of energy and security in mobile sensor network using classification based signal processing in heterogeneous network. J Signal Process Syst 2023;95(2–3):153–60.
[29] Keshmiry A, Hassani S, Mousavi M, Dackermann U. Effects of environmental and operational conditions on structural health monitoring and non-destructive testing: a systematic review. Buildings 2023;13(4):918.
[30] Figueiredo E, Park G, Farrar CR, Worden K, Figueiras J. Machine learning algorithms for damage detection under operational and environmental variability. Struct Health Monit 2011;10(6):559–72.

[31] Entezami A, Shariatmadar H, Mariani S. Early damage assessment in large-scale structures by innovative statistical pattern recognition methods based on time series modeling and novelty detection. Adv Eng Softw 2020;150:102923.

[32] Entezami A, Sarmadi H, Behkamal B. A novel double-hybrid learning method for modal frequency-based damage assessment of bridge structures under different environmental variation patterns. Mech Syst Signal Process 2023;201:110676.

[33] Abualigah L, Abd Elaziz M, Sumari P, Geem ZW, Gandomi AH. Reptile search algorithm (rsa): a nature-inspired meta-heuristic optimizer. Expert Syst Appl 2022;191:116158.

[34] Pedram M, Esfandiari A, Khedmati MR. Finite element model updating using strain-based power spectral density for damage detection. Struct Control Health Monit 2016;23(11):1314–33. https://doi.org/10.1002/stc.1833.

[35] Pereira J, Heylen W, Lammens S, Sas P. Influence of the number of frequency points and resonance frequencies on modal updating techniques for health condition monitoring and damage detection of flexible structure. In: Proceedings-SPIE the international society for optical engineering. Citeseer; 1995. p. 1273.

[36] Fathi A, Esfandiari A, Fadavie M, Mojtahedi A. Damage detection in an offshore platform using incomplete noisy FRF data by a novel bayesian model updating method. Ocean Eng 2020;217:108023. https://doi.org/10.1016/j.oceaneng.2020.108023.

[37] Kasdin NJ. Discrete simulation of colored noise and stochastic processes and 1/f/sup/spl alpha//power law noise generation. Proc IEEE 1995;83(5):802–27.

[38] Hassani S, Mousavi M, Dackermann U. Johansen cointegration of frequency response functions contaminated with nonstationary colored noise for structural damage detection. J Sound Vib 2023;552:117641.

[39] Härdle W. Smoothing techniques: with implementation in S. Springer Science & Business Media; 2012.

[40] Khorshidi MS, Nikoo MR, Sadegh M. Optimal and objective placement of sensors in water distribution systems using information theory. Water Res 2018;143:218–28.

[41] Khorshidi MS, Nikoo MR, Taravatrooy N, Sadegh M, Al-Wardy M, Al-Rawas GA. Pressure sensor placement in water distribution networks for leak detection using a hybrid information-entropy approach. Inf Sci 2020;516:56–71.

[42] He K, Zhang X, Ren S, Sun J. Delving deep into rectifiers: surpassing human-level performance on imagenet classification. In: Proceedings of the IEEE international conference on computer vision; 2015. p. 1026–34.

[43] Dos Santos JA, Soares CM, Soares CM, Maia N. Structural damage identification in laminated structures using FRF data. Compos Struct 2005;67(2):239–49. https://doi.org/10.1016/j.compstruct.2004.09.011.

[44] Reddy JN. Mechanics of laminated composite plates and shells: theory and analysis. CRC Press; 2003.

[45] Vo-Duy T, Ho-Huu V, Dang-Trung H, Nguyen-Thoi T. A two-step approach for damage detection in laminated composite structures using modal strain energy method and an improved differential evolution algorithm. Compos Struct 2016;147:42–53.

[46] Fallah N, Vaez SRH, Fasihi H. Damage identification in laminated composite plates using a new multi-step approach. Steel Compos Struct 2018;29(1):139–49.

[47] Ferreira A, Castro LM, Bertoluzza S. A high order collocation method for the static and vibration analysis of composite plates using a first-order theory. Compos Struct 2009;89(3):424–32. https://doi.org/10.1016/j.compstruct.2008.09.006.

[48] Ferreira A, Fasshauer G. Computation of natural frequencies of shear deformable beams and plates by an rbf-pseudospectral method. Comput Methods Appl Mech Eng 2006;196(1–3):134–46. https://doi.org/10.1016/j.cma.2006.02.009.

[49] Ferreira A, Fasshauer G. Analysis of natural frequencies of composite plates by an rbf-pseudospectral method. Compos Struct 2007;79(2):202–10. https://doi.org/10.1016/j.compstruct.2005.12.004.

[50] Ferreira A, Roque C, Martins P. Analysis of composite plates using higher-order shear deformation theory and a finite point formulation based on the multiquadric radial basis function method. Composites, Part B, Eng 2003;34(7):627–36. https://doi.org/10.1016/S1359-8368(03)00083-0.

[51] Hassani S, Mousavi M, Gandomi AH. A hilbert transform sensitivity-based model-updating method for damage detection of structures with closely-spaced eigenvalues. Eng Struct 2022;268:114761.

[52] Hassani S, Mousavi M, Gandomi AH. Damage detection of composite laminate structures using vmd of frf contaminated by high percentage of noise. Compos Struct 2022;286:115243.

[53] Dackermann U, Li J, Samali B. Damage identification based on modal strain energy utilising neural network ensembles'. In: Proceedings of the Australasian structural engineering conference; 2008.

[54] Li J, Dackermann U, Xu YL, Samali B. Damage identification in civil engineering structures utilizing pca-compressed residual frequency response functions and neural network ensembles. Struct Control Health Monit 2011;18(2):207–26.

[55] Dackermann U, Li J, Samali B. Dynamic-based damage identification using neural network ensembles and damage index method. Adv Struct Eng 2010;13(6):1001–16.

[56] Dackermann U. Vibration-based damage identification methods for civil engineering structures using artificial neural networks. Ph.D. thesis. 2009.